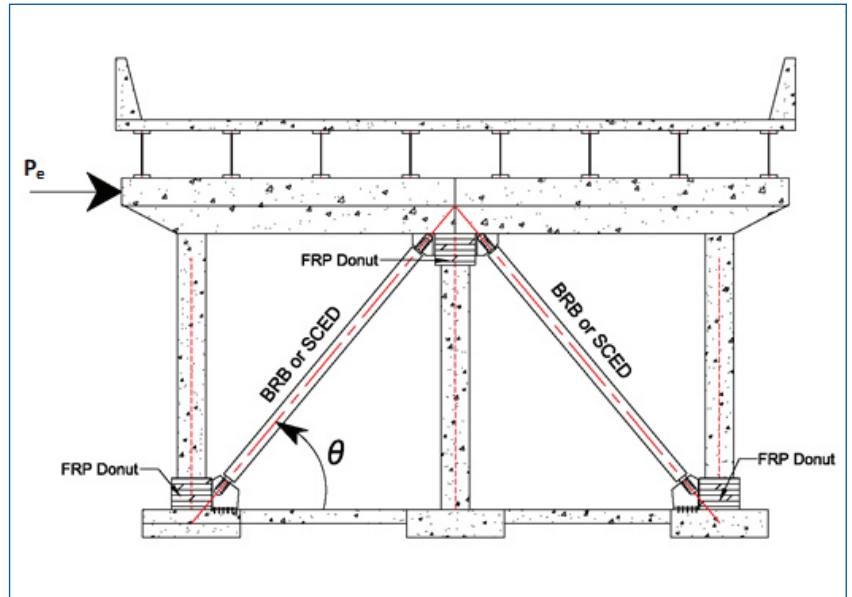


MOUNTAIN-PLAINS CONSORTIUM

MPC 18-348 | C. Pantelides, A. Upadhyay, and R. Wu

A Self-Centering Buckling Restrained Braces for Curved Bridges



A University Transportation Center sponsored by the U.S. Department of Transportation serving the Mountain-Plains Region. Consortium members:

Colorado State University
North Dakota State University
South Dakota State University

University of Colorado Denver
University of Denver
University of Utah

Utah State University
University of Wyoming

**SELF-CENTERING BUCKLING RESTRAINED BRACES
FOR CURVED BRIDGES**

Chris P. Pantelides
Professor

Anurag Upadhyay
Graduate Student

Ruoyang Wu
Graduate Student

Department of Civil and Environmental Engineering
The University of Utah

May 2018

Acknowledgements

The authors acknowledge the financial support provided by the Mountain-Plains Consortium (MPC) under project MPC-491.

Disclaimer

The contents of this report reflect the views of the authors, who are responsible for the facts and the accuracy of the information presented. This document is disseminated under the sponsorship of the Department of Transportation, University Transportation Centers Program, in the interest of information exchange. The U.S. Government assumes no liability for the contents or use thereof.

NDSU does not discriminate in its programs and activities on the basis of age, color, gender expression/identity, genetic information, marital status, national origin, participation in lawful off-campus activity, physical or mental disability, pregnancy, public assistance status, race, religion, sex, sexual orientation, spousal relationship to current employee, or veteran status, as applicable. Direct inquiries to Vice Provost, Title IX/ADA Coordinator, Old Main 201, 701-231-7708, ndsueoaa@ndsu.edu.

ABSTRACT

This project studies effective configurations of self-centering devices in the seismic retrofit of curved bridges for control of longitudinal and lateral forces. Reparability of bridge columns is investigated experimentally. A seismic retrofit and repair technique using a Carbon Fiber Reinforced Polymer (CFRP) donut and headed steel bars is implemented; a severely damaged cast-in-place column-to-cap beam joint and a column-to-footing joint are repaired using a CFRP donut, and their performance is compared to the original specimens. A fiber element model for the CFRP donut repair is developed. A numerical model of a seismically retrofitted curved bridge with Buckling Restrained Braces (BRBs) is developed. The steel core area and core length of BRBs is optimized to obtain maximum ductility of the retrofitted bridge under the design level earthquake. The optimized BRBs are placed in the bents of the bridge model and the seismic performance is evaluated through nonlinear dynamic analysis. The BRB retrofit is compared with a seismic retrofit using Self-Centering Energy Dissipation devices (SCEDs). Longitudinal BRBs/SCEDs are also implemented, which reduce the pounding forces between the deck and abutments. Guidelines are developed for the seismic retrofit of bridges using BRBs, SCEDs and CFRP donuts to enhance the seismic performance.

TABLE OF CONTENTS

1.	INTRODUCTION.....	1
1.1	Objectives and Scope of Work	1
1.2	Outline	1
2.	LITERATURE REVIEW	3
2.1	General.....	3
2.2	Seismic Performance of Multispan Bridges	3
2.3	Repair of Concrete Columns	3
2.4	Seismic Retrofit of Bridges with Buckling Restrained Braces.....	4
2.5	Self-centering Energy Dissipation Devices	4
3.	SEISMIC RETROFIT AND REPAIR OF DAMAGED CONCRETE COLUMNS USING CFRP DONUTS.....	6
3.1	Introduction.....	6
3.2	Experimental Investigation of Original Specimens	6
3.2.1	Description of Original Specimens	6
3.2.2	Experimental Results for Original Specimens	6
3.3	Design of the Repair	8
3.3.1	Design of CFRP Donut and Headed Steel Bars	8
3.3.2	Mix Design of Repair Concrete.....	9
3.3.3	Finite Element Model for Design of CFRP Cylindrical Shell.....	9
3.3.4	Design of CFRP Cylindrical Shell	10
3.3.5	Repair Procedure	10
3.4	Experimental Results for Repaired Specimens.....	11
3.4.1	Test Setup and Loading Protocol	11
3.4.2	Results for Repaired Cap Beam Specimen CB-CIP-R.....	11
3.4.3	Results for Repaired Footing Specimen F-CIP-R	12
3.5	Performance of Repaired Specimens	14
3.5.1	Headed Steel Bar Performance.....	15
3.5.2	CFRP Cylindrical Shell Performance.....	16
3.5.3	Moment-Plastic Rotation.....	18
3.6	Development of Numerical Model	18
3.6.1	Model Fiber	18
3.6.2	Distributed Plasticity over Plastic Hinge Length	19
3.6.3	Bond-slip Model for Modified Steel	19
3.6.4	Low-Cycle Fatigue	22
3.7	Numerical Results and Comparisons to Experiments.....	22
3.7.1	Hysteretic Response	22
3.7.2	Cumulative Hysteretic Energy	22
3.7.3	Moment-Rotation Response	22
3.7.4	Accumulated Low-Cycle Fatigue Damage	24
4.	SEISMIC RETROFIT OF A MULTI SPAN SIMPLY SUPPORTED CURVED BRIDGE WITH THREE-COLUMN BENTS.....	25
4.1	Description of Bridge	25
4.1.1	Superstructure and Substructure.....	25
4.1.2	Foundations and Soil Description	27

4.2	Numerical Model.....	27
4.3	Model Validation.....	29
4.3.1	BRB and SCED Model Validation.....	30
4.3.2	Performance Criteria	31
4.4	Mode Shapes.....	31
4.5	Seismic Retrofit Scheme.....	32
4.6	Non-linear Time-history Analysis	33
4.6.1	Deck Bearing Modification	33
4.7	Effect of Ground Motion Incidence Angle on Bridge Performance.....	35
4.8	Three-Dimensional Nonlinear Dynamic Analysis of Retrofitted Bridge with BRBs and SCEDs.....	39
4.9	Performance of Bridge Retrofitted with BRBs/SCEDs and CFRP Donut	48
5.	RECOMMENDED SEISMIC RETROFIT PROCEDURE USING BUCKLING RESTRAINED BRACES, SELF-CENTERING ENERGY DISSIPATION DEVICES AND CFRP DONUTS.....	50
5.1	Design of BRBs for Bridge Bents.....	50
5.2	Design of SCED for Bridge	51
5.3	Design of CFRP Donut for Column Shear	52
5.3.1	Strut-and-Tie Model for Retrofit Design.....	53
5.3.2	Design of Headed Steel Bars.....	53
5.3.3	Determination of CFRP Donut Geometry	53
5.3.4	Design of CFRP Cylindrical Shell	54
5.3.5	Design of Steel Collar	54
5.3.6	Design of CFRP Jackets Above the CFRP Donut.....	55
5.3.7	Foundation Seismic Rehabilitation.....	55
6.	CONCLUSIONS	58
6.1	CFRP Donut for Bridge Column Repair.....	58
6.2	Retrofit of Curved Bridge Using BRBs/SCEDs	59
	REFERENCES.....	60

LIST OF FIGURES

Figure 2.1	Buckling Restrained Brace: (a) Schematic (Starseismic LLC®); (b) hysteresis (NIST 2015).....	5
Figure 2.2	Schematic of a SCED and hysteresis (Christopoulos et al., 2008).....	5
Figure 3.1	Dimensions and reinforcement details of original specimens.....	7
Figure 3.2	Damage to original cast-in-place specimens: (a) CB-CIP-O; (b) F-CIP-O.....	8
Figure 3.3	Results from finite element model 7H2V of specimen CB-CIP-R: (a) CFRP shell stresses; (b) pushover curve of FEM CB-CIP-R compared to experimental backbone curve of CB-CIP-O.	10
Figure 3.4	Repair design details.	11
Figure 3.5	Repair procedure: (a) post-installed headed bars; (b) temporary form for CFRP wrapping; (c) CFRP shell; (d) CFRP donut.	11
Figure 3.6	Test set-up and loading protocol for repaired specimens.....	12
Figure 3.7	Plastic hinge relocation of repaired specimens: (a) CB-CIP-R; (b) F-CIP-R.	13
Figure 3.8	Hysteretic response of original and repaired specimens: (a) cap beam-to-column; (b) footing-to-column.	13
Figure 3.9	Damage of repaired specimen CB-CIP-R: (a) gap between column and CFRP donut at 2% drift ratio; (b) slip of the column inside the CFRP donut at 5% drift ratio; (c) column concrete crushing above donut at 6% drift ratio; (d) final damage.	13
Figure 3.10	Damage of repaired specimen F-CIP-R:(a) gap between column and CFRP donut at 3% drift ratio; (b) column concrete crushing at 5% drift ratio; (c) severe column concrete crushing at 7% drift ratio; (d) final damage.....	14
Figure 3.11	Cumulative hysteretic energy: (a) cap beam-to-column specimens; (b) footing-to-column specimens.	15
Figure 3.12	Stiffness degradation: (a) cap beam-to-column specimens; (b) footing-to-column specimens.	15
Figure 3.13	Backbone and idealized force-displacement relationships for: (a) cap beam; (b) footing specimens.	16
Figure 3.14	Headed steel bar longitudinal strain of cap beam specimen CB-CIP-R.....	17
Figure 3.15	CFRP hoop strain 38 mm below CFRP donut top for specimens: (a) CB-CIP-R; (b) F-CIP-R.	17
Figure 3.16	Measured hoop strain distribution of CFRP shell for specimens: (a) CB-CIP-R; (b) F-CIP-R.	17
Figure 3.17	Measured vertical strain distribution of CFRP shell for specimens: (a) CB-CIP-R; (b) F-CIP-R.....	18
Figure 3.18	Moment versus plastic rotation for specimens: (a) column-to-cap beam; (b) column-to-footing.	19
Figure 3.19	Schematic of Model Fiber.....	20
Figure 3.20	Schematic of bond-slip springs model.....	21

Figure 3.21	Bond stress-slip curves used in bond-slip springs model for CB-CIP-R.	21
Figure 3.22	Hysteretic response of repaired CIP specimens: (a) Model Fiber and test for CB-CIP-R; (b) Model Fiber and test for F-CIP-R.	23
Figure 3.23	Cumulative hysteretic energy comparisons: (a) CB-CIP-R; (b) F-CIP-R.....	23
Figure 3.24	Moment-rotation response comparisons: (a) CB-CIP-R; (b) F-CIP-R.	24
Figure 3.25	Low-cycle fatigue of two extreme column longitudinal steel bars from Model Fiber: (a) CB-CIP-R; (b) F-CIP-R.	24
Figure 4.1	Plan and elevation of the bridge.....	25
Figure 4.2	Bearings of the original bridge.....	26
Figure 4.3	Elevation of Bent 2.....	26
Figure 4.4	Sectional details: (a) Column (Sec. A-A); (b) Cap beam (Sec. B-B).....	27
Figure 4.5	Numerical model of one of the bents.	28
Figure 4.6	Numerical model of curved bridge rendered in MATLAB.....	28
Figure 4.7	Model validation: (a) comparison of numerical pushover analysis curve with experimental data; (b) test setup for bent 5S with half deck load.	29
Figure 4.8	Comparison of pile cap displacement of numerical pushover analysis with experimental data.	29
Figure 4.9	Comparison of lateral load capacity of numerical model of the bridge bent with half deck load (Pantelides et al. 1999) and full deck load.....	30
Figure 4.10	Validation of numerical model for: (a) BRB; (b) SCED.	30
Figure 4.11	First six mode shapes of as-built curved bridge.....	32
Figure 4.12	Seismic retrofit scheme for bridge with BRBs or SCEDs: (a) for individual bent; (b) at expansion joints; (c) at abutments.....	33
Figure 4.13	Comparison of lateral displacement of cap beam of Bent 2; span 2 and span 3 supported on Bent 2 of as-built bridge.....	34
Figure 4.14	Bearing at bent 2: (a) deformation time history; (b) hysteresis.....	34
Figure 4.15	Bearing replacement plan for the bridge.....	35
Figure 4.16	Comparison of lateral displacement of cap beam of bent 2; span 2 and span 3 supported on bent 2 for bridge after bearing replacement.....	35
Figure 4.17	Rotation of ground motion components.....	36
Figure 4.18	Drift ratio in global-X direction for bent 1.....	37
Figure 4.19	Drift ratio in global-X direction for bent 2.....	37
Figure 4.20	Drift ratio in global-Y direction for bent 2.....	38
Figure 4.21	Total base shear of three bents in global-X direction.....	38
Figure 4.22	Total base shear of three bents in global-Y direction.....	39
Figure 4.23	Pounding force on middle girder at abutment A.....	39

Figure 4.24	Performance of as-built bent 2 under ChiChi, Taiwan (1999) ground motion scaled to MCE.	40
Figure 4.25	Drift ratio time history of as-built bent 2 under ChiChi, Taiwan (1999) ground motion scaled to MCE.	40
Figure 4.26	Performance of as-built bridge bent 2 under Imperial Valley (1979) Delta station far-field ground motion scaled to MCE.	40
Figure 4.27	Performance of bridge bent 2 retrofitted with BRBs under Imperial Valley (1979) Delta station far-field ground motion scaled to MCE.	41
Figure 4.28	Performance of bridge bent 2 retrofitted with SCEDs under Imperial Valley (1979) Delta station far-field ground motion scaled to MCE.	42
Figure 4.29	Comparison of performance of as-built and retrofitted bridge bent 2 under Imperial Valley (1979) Delta station far-field ground motion scaled to MCE.	42
Figure 4.30	Drift ratio time history of as-built and retrofitted bridge bent 2 under Imperial Valley (1979) Delta station far-field ground motion scaled to MCE.	42
Figure 4.31	Hysteresis of one of the BRBs under the Imperial Valley (1979) Delta station far-field ground motion scaled to MCE.	43
Figure 4.32	Hysteresis of one of the SCEDs under the Imperial Valley (1979) Delta station far-field ground motion scaled to MCE.	43
Figure 4.33	Shear force demand in the column at the column-brace connection for Imperial Valley (1979) Delta station far-field ground motion scaled to MCE.	44
Figure 4.34	Column shear capacity enhancement with FRP donut.	44
Figure 4.35	Drift performance evaluation of as-built and retrofitted bridge under 22 far-field ground motions scaled to MCE level.	45
Figure 4.36	Concrete compressive strain performance evaluation of as-built and retrofitted bridge bent under 22 far-field ground motions scaled to MCE level.	45
Figure 4.37	Rebar tensile strain performance evaluation of as-built and retrofitted bridge bent under 22 far-field ground motions scaled to MCE level.	46
Figure 4.38	Pounding force between deck and abutment A for the as-built and retrofitted bridge under 22 far-field ground motions scaled to MCE level.	46
Figure 4.39	Pounding force time-history at abutment A for the as-built and retrofitted bridge under Kobe (1995) ground motion scaled to MCE level.	47
Figure 4.40	Total base shear resisted by columns of three bents in global-X direction under 22 far-field ground motions scaled to MCE level.	47
Figure 4.41	Residual drift CDF of as-built and retrofitted bridge bent 2 under 22 far-field ground motions scaled to MCE level.	48
Figure 4.42	Comparison of drift for bent 2 of bridge retrofitted with BRBs and BRBs+Donut for Landers, Yermo fire station ground motion scaled to MCE level.	49
Figure 4.43	Stress-strain performance of: (a) column core concrete; (b) rebar of bent 2 of the bridge retrofitted with BRBs and BRBs+Donut for Landers, Yermo fire station ground motion scaled to MCE level.	49

Figure 4.44 Performance comparison of BRB at bent 2 of the bridge retrofitted with BRBs and BRBs+Donut for Landers, Yermo fire station ground motion scaled to MCE level: (a) hysteretic curves; (b) cumulative energy dissipated by the BRB.....	49
Figure 5.1 Retrofit scheme for old bridges.	52
Figure 5.2 Design of self-centering material.	52
Figure 5.3 Design of CFRP donut: (a) Simplified Strut-and-Tie model; (b) design of hoop layers.....	56
Figure 5.4 Retrofit details of CFRP donut for column.....	56
Figure 5.5 Retrofitted bridge bent with CFRP composite jackets and CFRP donut.....	57

LIST OF TABLES

Table 3.1 Material properties. 7

Table 3.2 Original and repaired specimen results. 7

Table 3.3 Mix design of non-shrink concrete..... 9

Table 4.1 Performance states of Vision 2000..... 31

Table 4.2 Drift limits for performance criteria. 31

EXECUTIVE SUMMARY

Existing bridges, erected before the 1970s, have several deficiencies and need a seismic retrofit. Based on current seismic bridge design philosophy, damage to bridge substructures during strong earthquakes is restricted to the ends of bridge columns. A retrofit scheme using Buckling Restrained Braces (BRBs) or Self-Centering Energy Dissipation (SCED) devices and Carbon Fiber Reinforced Polymer (CFRP) concrete donuts is investigated for a curved bridge with substandard seismic details. A numerical model of the multi-span simply supported curved bridge is analyzed to assess seismic demand. In addition, probabilistic seismic analysis is performed using the original and retrofitted bridge models. Nonlinear time-history analysis shows that after seismic retrofit, the BRBs in bridge bents can mitigate the influence of incidence angle. To predict the maximum bridge response, it is sufficient to apply the minor component of the ground motion along the bridge longitudinal axis and the major component of the ground motion in the transverse direction. Additional findings of this research include:

- BRBs reduce peak drift demand experienced by the bridge bent by up to 60%, thus reducing structural response in the “operational” performance level.
- Longitudinal BRBs/SCEDs significantly reduce the pounding forces between the deck and abutment. For 20 of the 22 ground motions studied, BRB/SCED devices completely eliminated pounding.
- BRBs/SCEDs reduce displacement demand at the expansion joints and seismic pounding damage to the bridge deck.
- SCEDs successfully bring the bridge bent close to the initial position after an earthquake and reduce the residual drift. This keeps the bridge’s structural response in the “operational” performance level. Bridges retrofitted with BRBs have a larger residual drift due to yielding of the BRB core. As-built bridges also have a larger residual drift because of damage to concrete, yielding and potential buckling of steel bars.
- The column shear demand increases due to implementation of BRBs/SCEDs since these devices transfer the seismically induced forces to the column-foundation and column-beam joints. The increased shear demand can lead to shear failure of substandard columns at the connection. CFRP donuts enhance the shear capacity at the critical section and provide additional base shear capacity to the bridge bent.

NOTATION

AISC – American Institute of Steel Construction

ALI – Axial Load Index

BRB – Buckling Restrained Brace

CFRP – Carbon Fiber Reinforced Polymer

DBE – Design Basis Earthquake

FEA – Finite Element Analysis

FEM – Finite Element Model

GM – Ground Motion

IDA – Incremental Dynamic Analysis

MCE – Maximum Credible Earthquake

MSC – Multi Span Continuous

MSSS – Multi Span Simply Supported

OpenSEES – Open System for Earthquake Engineering Simulations

PEER – Pacific Earthquake Engineering Research

PGA – Peak Ground Acceleration

Sa – Spectral acceleration

SCED – Self-Centering Energy Dissipation Device

1. INTRODUCTION

1.1 Objectives and Scope of Work

In recent large earthquakes, existing bridges designed and constructed according to older design provisions have suffered severe damage or collapse. Poorly detailed or deficient bridge structures cannot resist strong earthquakes (Priestley et al. 1996). Such bridges are vulnerable to collapse, which could lead to significant economic losses due to bridge closure in the immediate aftermath of a strong earthquake. Structural pounding at expansion joints or at the abutments has caused damage to the deck and unseating due to irreparable rebound action. Columns of multi-column bridge bents experienced shear failure due to lack of transverse reinforcement or flexural failure due to an inadequate plastic hinge mechanism. Modern seismic design methods have improved the seismic performance of bridges by introducing elements capable of achieving high ductility. Although these elements are designed for life-safety requirements, i.e. to prevent collapse, the inelastic damage to the primary structural elements may be significant and not repairable; this requires temporary closure for weeks or months to restore the bridge to an operational service condition.

The first part of this research investigates the repair of damaged bridge columns using CFRP donuts. Two severely damaged cast-in-place half-scale specimens representing a beam-to-column connection and a footing-to-column connection are repaired using a CFRP donut, which consists of a multilayered CFRP shell filled with concrete for confinement and headed steel bars drilled into the beam/footing for additional flexural and shear capacity. The second part of this research investigates the behavior of curved bridges with multicolumn bents by implementing BRBs/SCEDs as energy dissipation devices. Damage to the structure can be minimized by using these devices. BRBs/SCEDs should be designed in such a way that they yield before any element of the bridge substructure suffers significant damage. After the earthquake, the BRBs/SCEDs could be replaced, thus keeping the structure serviceable. Five different cases of seismic retrofit are studied in this research: (i) CFRP donuts to improve column flexural and shear performance, (ii) BRBs/SCEDs placed between girders and abutments to mitigate structural pounding, (iii) BRBs/SCEDs placed between girders of adjacent spans at expansion joints of bridge decks to prevent structural pounding, (iv) BRBs/SCEDs placed diagonally between columns of a multi-column bridge bent to enhance lateral shear capacity and hysteretic energy dissipation, and (v) BRBs and CFRP donuts combining cases (i) and (iv) for superior seismic performance.

1.2 Outline

Section 2 provides a summary of topics including structural pounding observed in bridges and seismic retrofit methods for pounding mitigation, seismic rehabilitation of multicolumn bridge bents, and implementation of BRBs and SCEDs in bridges.

Section 3 discusses a bridge column seismic retrofit and repair technique using CFRP donuts and headed steel bars. Two damaged cast-in-place half-scale bridge column-to-cap beam and column-to-footing specimens are repaired using a CFRP donut filled with concrete and headed steel bars in the footing/cap beam to transfer tension and increase flexural capacity. The performance of the repaired columns is compared to that of the original specimens. A fiber element model for the CFRP donut repair using OpenSEEs (PEER 2016) is developed for analytical studies.

A numerical model of a seismically retrofitted multispan simply supported (MSSS) curved bridge with BRBs is developed in Section 4. The nonlinear seismic response analysis of the bridge was performed using OpenSEEs (PEER 2016). The steel core area and core length of the BRBs is optimized to obtain maximum ductility of the retrofitted bridge under the design level earthquake (DBE). The optimized

BRBs are placed in the bents of the full-scale bridge model and the seismic performance is evaluated through nonlinear time-history analysis. The BRB retrofit is subsequently compared with a seismic retrofit of the same bridge using SCEDs to assess the feasibility and importance of self-centering.

Section 5 presents guidelines for the seismic retrofit of a multicolumn bridge bent using BRBs, SCEDs and CFRP donuts to enhance the overall performance, including the shear capacity of the columns.

Section 6 offers conclusions regarding the use of a CFRP donut for bridge column repair, the retrofit of curved bridges using BRBs/SCEDs, and the combination of the two seismic retrofit techniques for superior seismic performance.

2. LITERATURE REVIEW

2.1 General

Research has been conducted on the seismic performance of curved bridges and on retrofit measures for improving their performance during strong earthquakes. Researchers have investigated the use of Buckling Restrained Braces (BRBs) for seismic retrofit of bridges. Innovative earthquake-resistant systems that reduce residual displacements, called “self-centering” systems, have been studied analytically and experimentally for various structural systems. This section provides background information on previous research regarding repair of concrete columns, self-centering systems, and techniques for reducing residual displacements.

2.2 Seismic Performance of Multispan Bridges

Many studies have evaluated the seismic response of typical Multi Span Simply Supported (MSSS) and Multi Span Continuous (MSC) steel girder bridges to examine their seismic behavior and the impact of modeling fidelity on their performance. Dicleli and Bruneau (1995) found that bearing stiffness significantly affects the response of MSSS steel girder bridges and indicated that if pounding were considered in the longitudinal direction, there could be a large potential for failure of bearings in shear, and span unseating. For MSC bridges, damage to steel bearings is probable, but could serve as an effective way of isolating the superstructure and preventing further column damage. Padgett and DesRoches (2008) evaluated the three-dimensional nonlinear seismic performance of retrofit measures for typical steel girder bridges; use of elastomeric bearings in MSC bridges increased passive deformations due to pounding. Pan et al. (2007, 2010) performed parametric studies to evaluate seismic fragility of MSSS highway bridges and showed that pounding of girders at abutments could lead to a change in curvature ductility of the concrete piers.

Historical development of the design of curved bridges in the United States can be found in the literature (Tongaonkar and Jangid 2003; DeSantiago et al. 2005; Linzell et al. 2004; Banerjee et al. 2016). Seo and Linzell (2011, 2012) found that the radius of curvature and number of spans in curved bridges have the most influence on bridge performance. Ates and Constantinou (2011a, 2011b) investigated the performance of a curved bridge with an isolated deck considering soil-structure interaction, and found that maximum bearing displacements occur when the bridge is under radial direction earthquakes. Amjadian and Agrawal (2016) used a model to study rigid body motion of curved bridges subjected to earthquake induced pounding; curved bridges with subtended angles between 450 and 900 had high radial displacements whereas bridges with angles between 900 and 1350 had high azimuthal displacements due to pounding. Monzon et al. (2016) performed shake table tests of a 0.4-scale symmetric single column curved bridge to examine the efficiency of base isolation of bridge decks using rubber isolators; base isolation kept the column elastic, but induced unsymmetry in the response of the deck at the abutments leading to higher displacements.

2.3 Repair of Concrete Columns

During strong earthquakes, damage to bridge substructures is meant to be limited to the ends of bridge columns (AASHTO 2011). Repair of damaged columns is preferable to replacement; benefits include rapid construction, decreased interruption, and reduced cost. Research efforts have focused on seismic repair and retrofit of reinforced concrete (RC) columns (Chai et al. 1991; Kitada 1998; He et al. 2015). Several column repair alternatives have been studied, such as steel jackets (Chai et al. 1991), RC jackets (Rodriguez and Park 1994; Lehman et al. 2001), fiber reinforced polymer (FRP) jackets (Saadatmanesh et al. 1997; Pantelides and Gergely 2002; Saiidi and Cheng 2004; He et al. 2013; Kumar and Mosalam

2015; Parks et al. 2016; Wu and Pantelides 2017a; b); FRP bars combined with FRP jackets (Jiang et al. 2016), bar couplers (Yang et al. 2015), prestressed steel jackets (Fakharifar et al. 2016), shape memory alloy spirals (Shin and Andrawes 2011), and engineered cementitious composite jackets (Billah and Alam 2014). FRP composites are used because of their high strength, light weight, and non-corrosive properties. The ductile performance of FRP strengthened structures has been documented (Gergely et al. 1998). Prefabricated FRP composite jackets have been used to enhance shear strength (Xiao et al. 1999). During large earthquakes, column steel reinforcement buckles or fractures and concrete crushes and spalls. Typically, repair of such damage involves removal of core concrete and replacement of the buckled and fractured steel reinforcement, which requires significant time and effort to implement (Rodriguez and Park 1994; Yang et al. 2015).

2.4 Seismic Retrofit of Bridges with Buckling Restrained Braces

Buckling restrained braces (BRBs) are mechanical damping devices consisting of a central steel core surrounded by a steel tube that restrains the core from axially buckling in compression; the space between the core and the tube is filled with mortar. Unbonding material covers the steel core to isolate it from the concrete and allows it to deform freely in the axial direction. The unbonding material is thin enough to avoid local buckling of the core, and yet thick enough to accommodate lateral expansion of the core due to Poisson's ratio effects. The steel core usually has a rectangular or cruciform cross-sectional shape. Figure 2.1(a) shows the components of a BRB and additional details. Figure 2.1(b) shows the hysteretic performance model of a BRB, as compared to a conventional steel brace, which is prone to failure due to compression buckling.

Research toward possible use of Buckling Restrained Braces (BRB) in bridge structures to dissipate seismic energy has been conducted. El-Bahey and Bruneau (2011) studied the use of BRBs as structural fuses for seismic retrofit of bridges. Upadhyay et al. (2015) used a model of a curved bridge with single column bents to show that BRBs are effective in reducing girder displacements thus preventing damage due to pounding at the abutments. Wang et al. (2016) found that BRBs can redistribute and dissipate energy thus reducing seismic drift and the potential failure of concrete columns and abutment shear keys. The BRBs show unbalance between axial compression and tension strength, ranging from 5% to 30%, due to restraining effects and the presence of unbonded materials. This unbalance could lead to permanent deformation of bridge bents, which is not desirable after a strong earthquake. A BRB retrofit design using the fuse concept was tested by Bazaez and Dusicka (2016, 2017) on a scaled bridge bent and was compared to a retrofitted bent using a typical industrial BRB. Results showed that the bent retrofitted with BRBs designed with the structural fuse concept performed better than the one with a standard BRB design in terms of improving displacement ductility; the drift ratio capacity was higher with the standard BRB design compared to a structural fuse BRB design. Wei and Bruneau (2017) performed nonlinear time-history analyses using numerical models of different bridge types to study the effectiveness of seismic retrofit of bridge bents using the structural fuse concept and showed that the displacement demands were reduced on average by 50% using a BRB retrofit.

2.5 Self-centering Energy Dissipation Devices

Self-centering energy dissipation devices are used to reduce residual displacements in structures. Researchers have tested different self-centering devices, including a posttensioned Self Centering Energy Dissipation (SCED) device in moment frames (Christopoulos et al., 2008; Miller et al., 2012; Kammula et al., 2013; Chou et al., 2014; Zhou et al., 2015), shape memory alloys (SMA) in bridge columns (Varela and Saiidi, 2014; Gao et al., 2016), and rocking columns with external energy dissipation devices (Marriot et al., 2011; Guerrini et al., 2015). Upadhyay and Pantelides (2017) compared the performance of a BRB and SCED retrofit of a multicolumn bridge bent and showed that the SCED retrofit reduces the residual drift significantly, making it possible to repair the bridge bent after an earthquake.

Self-centering energy dissipation devices are a combination of post-tensioned high strength tendons and an energy dissipation mechanism using friction or yielding, which enable the brace to recenter. Figure 2.2 shows a schematic of a self-centering energy dissipation device. The brace consists of an outer and an inner steel tube connected to the brace ends. This arrangement enables the tendons to be in tension irrespective of a tension or compression force in the brace. The initial stiffness of the brace is provided by the PT bars, and the inner and outer tube. Once the outer and inner tubes lose contact with each other, the secondary stiffness is provided only by the PT bars. The force at which the brace enters the secondary stiffness during loading, termed “forward activation force,” is equal to the pre-tension in the tendons and peak friction force of the energy dissipater. The point at which the brace changes its stiffness during unloading is termed the “reverse activation force.” Energy dissipation efficiency depends on the friction coefficient of the damper.

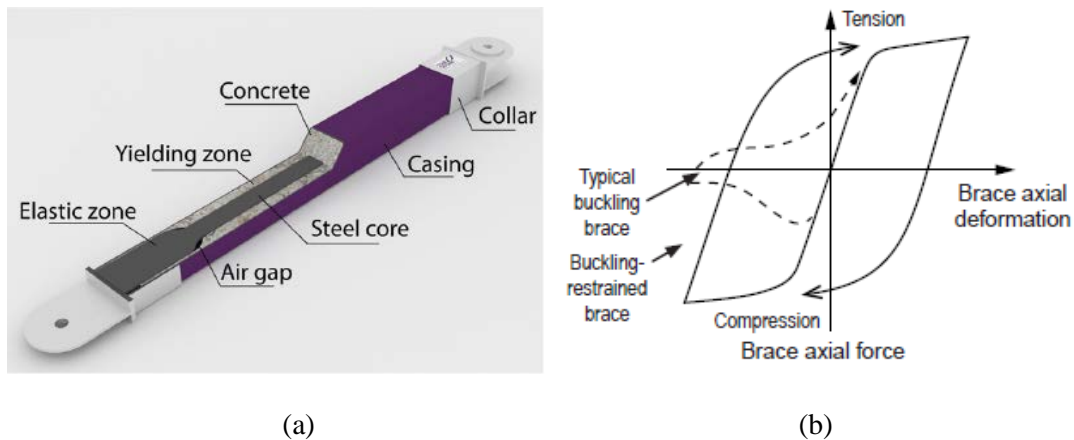


Figure 2.1 Buckling Restrained Brace: (a) Schematic (Starseismic LLC®); (b) hysteresis (NIST 2015).

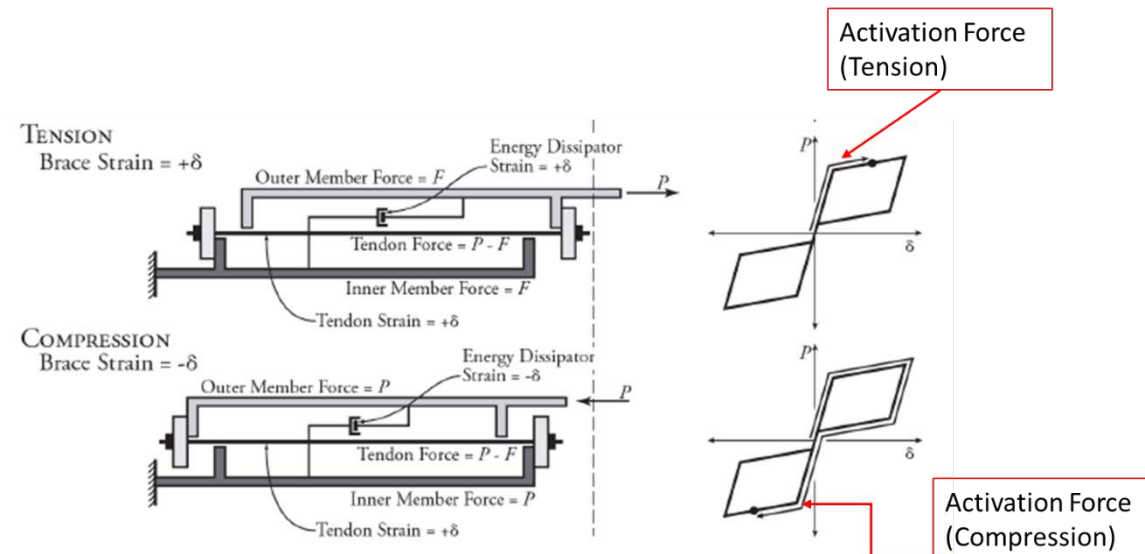


Figure 2.2 Schematic of a SCED and hysteresis (Christopoulos et al., 2008).

3. SEISMIC RETROFIT AND REPAIR OF DAMAGED CONCRETE COLUMNS USING CFRP DONUTS

3.1 Introduction

A repair method using a Carbon Fiber Reinforced Polymer (CFRP) cylindrical shell and epoxy-anchored headed steel bars for relocating the column plastic hinge is investigated with minimal intervention in the column (Parks et al. 2016; Wu and Pantelides 2017c; d). The CFRP shell encloses a number of headed steel bars and is filled with non-shrink concrete to a certain height to form a CFRP “donut.” In addition to providing confinement, the CFRP shell serves as a stay-in-place form. The method described in this report incorporates fibers in the hoop and vertical direction of the CFRP shell and is implemented for two severely damaged cast-in-place specimens, a cap beam-to-column connection and a footing-to-column connection. Typically, bridges with such severe damage would be demolished.

3.2 Experimental Investigation of Original Specimens

3.2.1 Description of Original Specimens

Two original cast-in-place (CIP) monolithic specimens, referred to as CB-CIP-O and F-CIP-O, were tested under quasi-static cyclic loads; the specimens were designed based on current seismic design standards for bridges (AASHTO 2011; Ameli et al. 2015, 2016). Notation CB stands for Cap Beam-to-Column connection and F represents a Footing-to-Column connection; letter O stands for original and R for repaired. The corresponding repaired specimens are referred to as CB-CIP-R and F-CIP-R.

The geometry and reinforcement of the original specimens, which included a column connected to a footing and a column connected to a cap beam, are shown in Figure 3.1. The column has a 533 mm octagonal cross-section and an effective column height of 2438 mm measured from the top of the cap beam/footing to the centerline of the column load stub. All steel reinforcement had a design yield strength of 414 MPa. The longitudinal reinforcement consists of six 25 mm steel bars arranged in a circular pattern. A 13 mm spiral at a 64 mm pitch is provided as transverse reinforcement. The footing is 1.82 m long, 610 mm deep, and 914 mm wide. The cap beam is 2.74 m long, 610 mm deep, and 610 mm wide. The concrete compressive strength measured on test day was 46 MPa per ASTM C39. The measured yield strength of longitudinal and transverse reinforcement was 469 MPa and 434 MPa, respectively per ASTM A370; the ultimate strength of longitudinal and transverse reinforcement was 641 MPa and 710 MPa, respectively. Detailed material properties for the original and repaired specimens are given in Table 3.1.

3.2.2 Experimental Results for Original Specimens

Table 3.2 summarizes the maximum lateral load, ultimate drift ratio, and failure mode of the original specimens. The original specimens were tested up to a drift ratio of 9.3%. The failure mode of both CB-CIP-O and F-CIP-O was fracture of the two extreme longitudinal bars. At failure of the original specimens, the lateral load capacity dropped to a level of 43% to 56% of the ultimate load. Figure 3.2 shows damage of the original columns at the footing/cap beam interface, where extensive spalling occurred in the plastic hinge region; flexural cracking reached 406 mm above the interface. Longitudinal steel bar fracture and buckling across multiple steel spiral hoops is evident. Concrete damage was severe in the bottom 305 mm of the column and extended into the column core.

A five-level damage states (DS) approach has been proposed to evaluate damage of RC columns (Vosooghi and Saiidi 2013); level DS-1 indicates flexural crack formation, whereas level DS-5 means

damage to the core concrete and imminent column failure. According to this damage level designation, the two original specimens had reached a damage state of DS-5, leading to significant reduction of the lateral load-carrying capacity. There is a perception that it is difficult to repair structural components with a damage level of DS-5; the objective of this research was to repair the severely damaged specimens rapidly with minimal intervention.

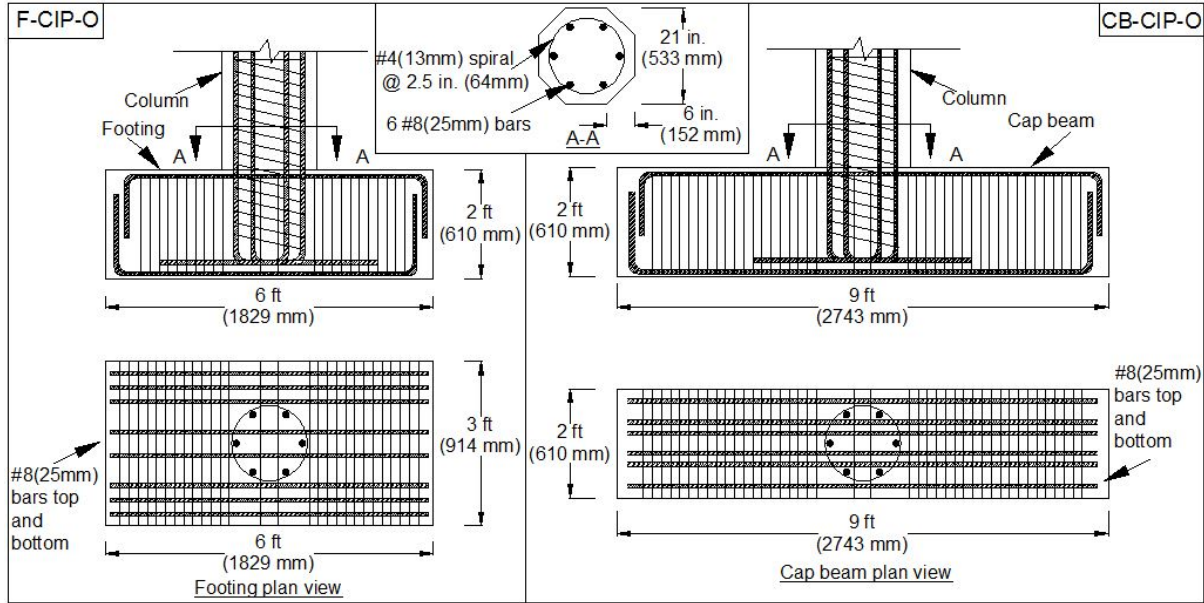


Figure 3.1 Dimensions and reinforcement details of original specimens.

Table 3.1 Material properties.

Material properties		CB-CIP-O	CB-CIP-R	F-CIP-O	F-CIP-R
Column concrete compressive strength	f'_c , MPa	46	51	46	52
CFRP donut concrete compressive strength	f'_{cd} , MPa	NA	76	NA	76
Headed steel bars	f_y , MPa	NA	427	NA	427
	f_u , MPa		593		593

Note: NA= Not applicable

Table 3.2 Original and repaired specimen results.

Test criteria	CB-CIP-O	F-CIP-O	CB-CIP-R	F-CIP-R
Maximum load, kN	168	160	203	195
Ultimate drift ratio, %	9.3	8.8	8.1	8.4
Failure mode	East and west bar fracture	East and west bar fracture	Severe concrete crushing	Severe concrete crushing
Yield strength, kN	143	149	190	181
Effective yield displacement, mm	23	24	29	34
Ultimate displacement, mm	227	215	198	204
Elastic stiffness, kN/mm	6.29	6.23	6.49	5.31
Displacement ductility	9.9	8.9	6.8	6.0

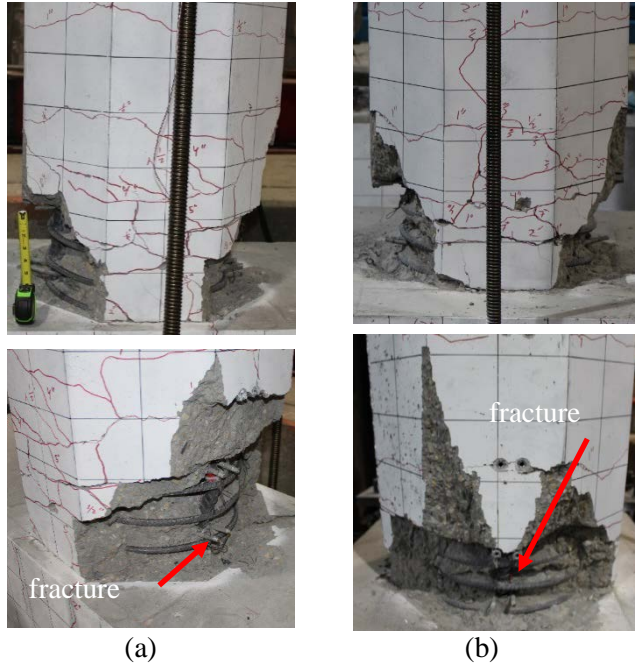


Figure 3.2 Damage to original cast-in-place specimens: (a) CB-CIP-O; (b) F-CIP-O.

3.3 Design of the Repair

3.3.1 Design of CFRP Donut and Headed Steel Bars

The seismic repair was intended to strengthen the original specimens and restore their lateral strength and displacement capacity. A CFRP cylindrical shell, consisting of hoop and vertical CFRP layers, epoxy anchored headed steel bars, and repair concrete were used to create a CFRP donut and relocate the column plastic hinge above it. Considering the 57 mm diameter of the head of the headed steel bars and the clearance for avoiding contact with the column, a 762 mm diameter circular cross-section was used for the repair. To determine the height of the CFRP donut, the plastic hinge length was determined as follows (Panagiotakos and Fardis 2001):

$$L_{pl} = 0.12L_s + 0.014a_s d_b f_y \quad (3.1)$$

where L_s is the shear span, a_s equals 1.0 by considering steel bar bond-slip in the plastic hinge, d_b is the diameter of the longitudinal column steel bars, and f_y is the yield strength, in SI units. The plastic hinge region from Eq. (3.1) was calculated as 460 mm. According to the damage condition of the original specimens a repair height of 483 mm was selected.

Based on the flexural demand at the repaired section of the CFRP donut, six 25 mm diameter headed steel bars were provided with a 445 mm height above the cap beam/footing. The headed steel bars were embedded 483 mm into the cap beam/footing and anchored using epoxy. The flexural capacity of the repaired section with the headed steel bars was determined using sectional analysis. The length of the headed steel bars above and below the interface satisfies the development length criteria of ACI 318 (ACI 2014). The properties of the headed steel bars are shown in Table 3.1.

The measured ultimate tensile capacity of the CFRP composite was 780 MPa, the modulus of elasticity was 65 GPa, and the ultimate tensile strain was 1.20%, as determined from tensile coupon tests carried out according to ASTM D3039 requirements.

3.3.2 Mix Design of Repair Concrete

High-strength repair concrete with a compressive strength of 75.8 MPa was provided inside the CFRP donut. The mix design of the repair concrete is shown in Table 3.3. A quantity of Portland cement 15% by volume was replaced with expansive cement to avoid shrinkage of the repair concrete and reduction of confinement effectiveness.

3.3.3 Finite Element Model for Design of CFRP Cylindrical Shell

Nonlinear finite element analysis (FEA) was conducted for finding the number and orientation of CFRP layers for the shell. Materials considered in the analysis were: column concrete and concrete inside the CFRP donut, reinforcing steel bars, headed steel bars, and CFRP shell. Three-dimensional eight-node solid elements were used to model the concrete, and four-node shell elements were used to model the CFRP shell. Three-dimensional two-node truss elements were used to model the steel bars. The concrete damaged plasticity model was used to simulate inelastic response of the concrete and a yield surface was adopted (Dassault Systèmes Simulia 2014). Considering the extensive damage of the original specimens, modified steel properties were used for the repaired columns.

Static pushover analyses were conducted using a displacement-based method up to a drift ratio of 8.0%. A Finite Element Model (FEM) was developed with CFRP layers in the hoop and vertical direction. Transverse cracks in the CFRP cylindrical shell, were observed in previous tests using a CFRP donut (Parks et al. 2016); therefore, vertical CFRP layers were inserted in the CFRP shell model in an effort to prevent such cracks from occurring. An efficiency factor equal to 0.58 was used to account for three-dimensional stresses (American Concrete Institute Committee 440, 2008). Several FEM models were created with different combinations of hoop and vertical CFRP layers. The maximum hoop stress for the model with four hoop layers was 438 MPa or 97% of the allowable CFRP ultimate stress of 452 MPa. For the case of seven hoop layers and two vertical layers, designated as model 7H2V, the maximum hoop stress was 251 MPa or 55% of the allowable CFRP ultimate stress.

Figure 3.3(a) shows the maximum stress (MPa) in one CFRP hoop layer of model 7H2V; stress concentration at a 152 mm wide strip was noted at the top of the CFRP shell corresponding to the top of

Table 3.1 Mix design of non-shrink concrete.

Components		Weight, kg
Cement	Type II cement	263.6
	Komponent	46.5
Water		104.1
9.5 mm rock		739.6
Sand		538.8
Type F fly ash		78.1
Additives	Gelenium 30-30	3.3
	Delvo stabilizer	3.0
	Air-Entraining admixture	0.14

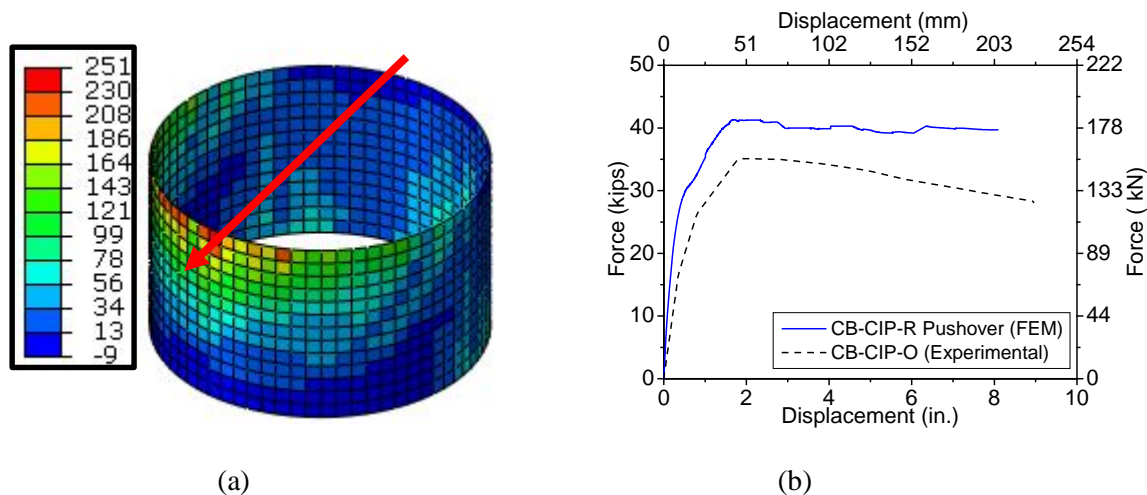


Figure 3.3 Results from finite element model 7H2V of specimen CB-CIP-R: (a) CFRP shell stresses; (b) pushover curve of FEM CB-CIP-R compared to experimental backbone curve of CB-CIP-O.

the headed steel bars. The pushover curve of model 7H2V for specimen CB-CIP-R is shown in Figure 3.3(b) and is compared with the backbone curve from the experiment of the original cap beam CB-CIP-O. The calculated shear capacity of the column above the CFRP donut was 1068 kN, which was significantly higher than the required shear of 188 kN obtained from the FEM model.

3.3.4 Design of CFRP Cylindrical Shell

The final repair design is shown in Figure 3.4. Based on the FEM pushover analysis, seven CFRP hoop layers were applied; in addition, two CFRP vertical layers were applied for the full height of the shell. Since the damage state of the two original CIP specimens was similar, the 483 mm high CFRP cylindrical shell was used for both repaired specimens. Details of the headed steel bars are also shown in Figure 3.4.

3.3.5 Repair Procedure

The repair procedure is shown in Figure 3.5. First, the holes for six 25 mm headed steel bars were core drilled into the footing/cap beam and the headed bars were epoxy anchored; the epoxy had a bond strength of 12.4 MPa. A 762 mm diameter and 483 mm high form was cut into two half-cylinders; duct tape was used to reconnect the two halves after placement around the column. A thin plastic sheet was used as a bond breaker before wrapping the CFRP sheets. A splice length equal to 343 mm was used for each CFRP hoop layer. A 13 mm gap was left at the bottom of the CFRP shell to avoid contact with the footing/cap beam, as shown in Figure 3.4. The CFRP shell was sealed to act as a stay-in-place form; high-strength concrete with expansive cement was cast in the space between the CFRP cylindrical shell and the column.

The cap beam specimen was tested upside down. The beam width was smaller than the CFRP shell diameter; wood forms were placed along the cap beam to provide support for the repair concrete as shown in Figure 3.5(c). In practice, the cap beam would be above the column and the gap would provide an inlet for casting the repair concrete. It takes six hours to install the six headed steel bars and two hours to install the CFRP shell; curing of the CFRP shell can be achieved in approximately 48 hours, after which the repair concrete could be cast.

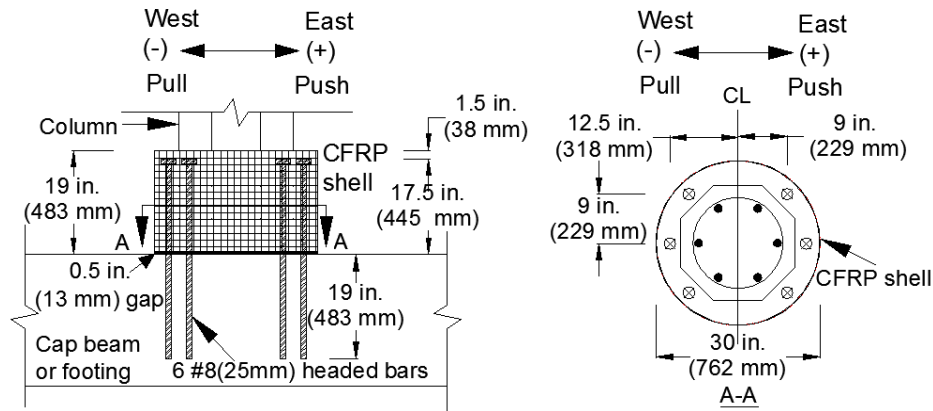


Figure 3.4 Repair design details.

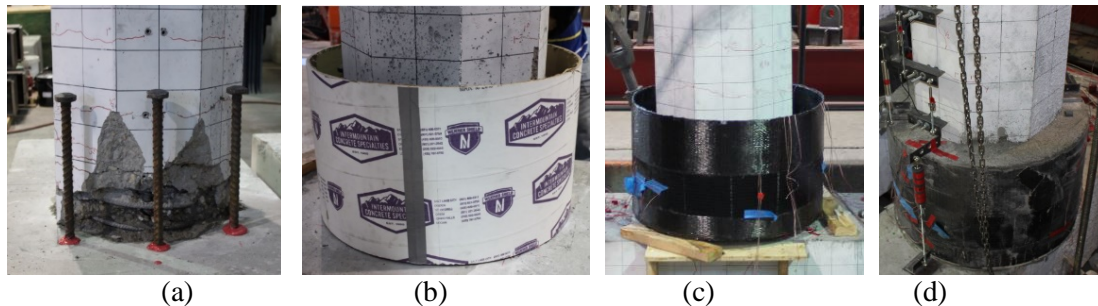


Figure 3.5 Repair procedure: (a) post-installed headed bars; (b) temporary form for CFRP wrapping; (c) CFRP shell; (d) CFRP donut.

3.4 Experimental Results for Repaired Specimens

3.4.1 Test Setup and Loading Protocol

The test setup and loading protocol were the same for the original and repaired specimens. A lateral displacement-controlled, cyclic quasi-static load was applied using a hydraulic actuator with the loading protocol shown in Figure 3.6. The axial load was applied using a hydraulic cylinder; the axial load index (ALI) was set to 6% of the column axial compression capacity. The lateral drift history consisted of increasing amplitudes with two cycles at each drift ratio until failure (American Concrete Institute Committee 374, 2013). The footing and cap beam had a span between supports of 1.22 m and 2.44 m, respectively. String potentiometers were used to measure column displacement at the level of the load stub. Strain gauges were attached to the headed steel bars and CFRP shell.

3.4.2 Results for Repaired Cap Beam Specimen CB-CIP-R

Damage to specimen CB-CIP-R is shown in Figure 3.7(a); the hysteresis curve is compared to that of the original specimen CB-CIP-O in Figure 3.8(a). Table 3.2 shows that specimen CB-CIP-R achieved a 21% increase in lateral load capacity compared to the original specimen; the displacement capacity was similar to the original specimen. Cracks widened at the same locations created during testing of the original specimen. At a drift ratio of 2%, radial cracks 0.13 mm wide formed at the top surface of the concrete of

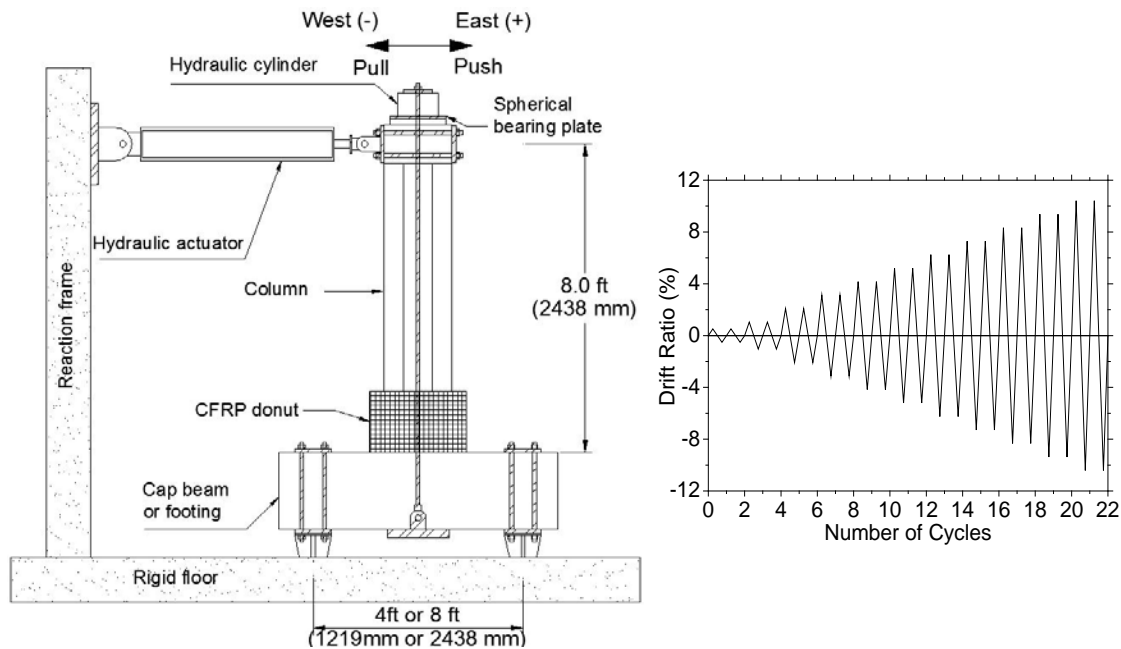


Figure 3.6 Test set-up and loading protocol for repaired specimens.

the CFRP donut. In the test of original specimen CB-CIP-O, fracture of the two extreme longitudinal bars and concrete spalling in the plastic hinge region extended into the column core (Figure 3.2(a)); thus, a weak bond between column and repair concrete was observed and a gap developed between original column and repair concrete at the CFRP donut surface as shown in Figure 3.9(a).

At a drift ratio of 3%, radial cracks in the repair concrete widened to 0.33 mm, the column concrete above the CFRP donut started to spall and the gap between concrete inside the CFRP donut and column widened. At a drift ratio of 4%, the column corners in the CFRP donut concrete started crushing. At a drift ratio of 5%, column cracks were 1.0 mm wide and separation of column and repair concrete was evident. The severe spalling of the original column concrete and the weak bond between column and CFRP donut concrete caused the column to slip inside the CFRP donut, as shown in Figure 3.9(b). At a drift ratio of 6%, the maximum lateral load capacity was reached with column concrete crushing above the CFRP donut in the plastic hinge region, as shown in Figure 3.9(c). The test was terminated at a drift ratio of 8.4% after a 38% drop in lateral load.

Concrete crushing occurred in the relocated plastic hinge region 470 mm above the CFRP donut on the west side and 356 mm on the east side. The column core concrete and steel spirals were exposed and damage developed in the column 70 mm inside the CFRP donut, as shown in Figure 3.9(d). The CFRP shell and repair concrete were not damaged.

3.4.3 Results for Repaired Footing Specimen F-CIP-R

Damage to specimen F-CIP-R is shown in Figure 3.7(b). The hysteretic response superimposed with that of the original column F-CIP-O is shown in Figure 3.8(b). The maximum lateral load for F-CIP-R was 22% higher than that for F-CIP-O. A gap between column and repair concrete started at a drift ratio of 2%, and became prominent at a drift ratio of 3%, as shown in Figure 3.10(a). Radial cracks on the top surface of the repair concrete and column cracks widened to 0.25 mm at a 4% drift ratio. The maximum lateral load capacity was reached at a drift ratio of 5% and concrete crushing and spalling was observed as

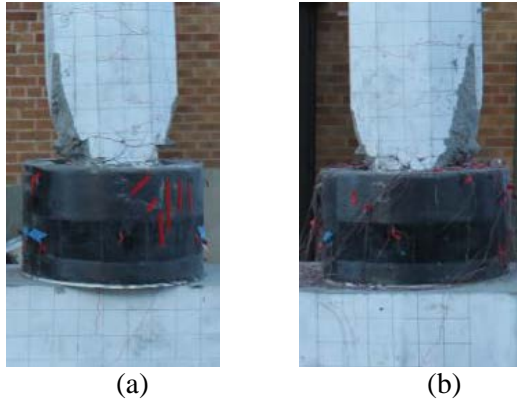


Figure 3.7 Plastic hinge relocation of repaired specimens: (a) CB-CIP-R; (b) F-CIP-R.

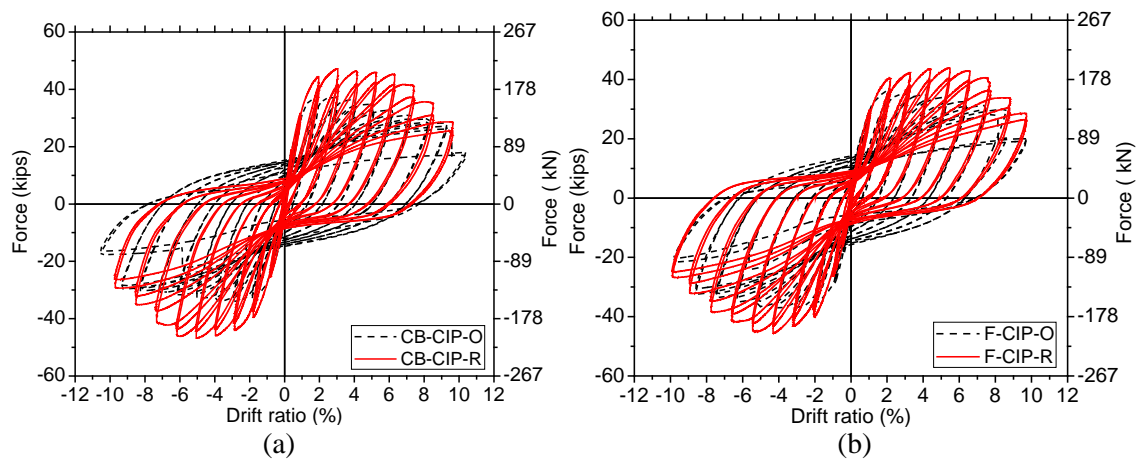


Figure 3.8 Hysteretic response of original and repaired specimens: (a) cap beam-to-column; (b) footing-to-column.

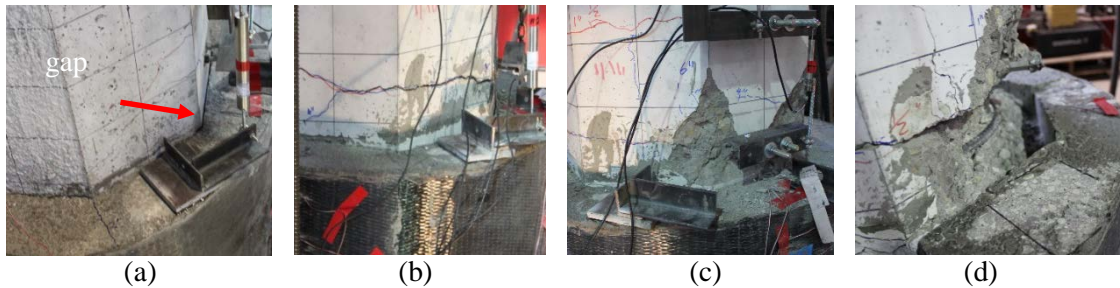


Figure 3.9 Damage of repaired specimen CB-CIP-R: (a) gap between column and CFRP donut at 2% drift ratio; (b) slip of the column inside the CFRP donut at 5% drift ratio; (c) column concrete crushing above donut at 6% drift ratio; (d) final damage.

shown in Figure 3.10(b), which became severe at a drift ratio of 7% as shown in Figure 3.10(c). At a drift ratio of 8.4%, the specimen failed due to concrete crushing, 546 mm above the CFRP donut on the east side and 298 mm on the west side. Steel reinforcement was exposed and column concrete cover spalled. Two fractured and buckled steel bars and severe concrete damage of the original column, which extended into the column core (Figure 3.2(b)), created a weak bond between the column and repair concrete and allowed a gap to form between the original column and repair concrete inside the CFRP donut. Column

concrete damage reached a depth of 76 mm inside the CFRP donut, as shown in Figure 3.10(d). No damage was observed in the CFRP shell or repair concrete.

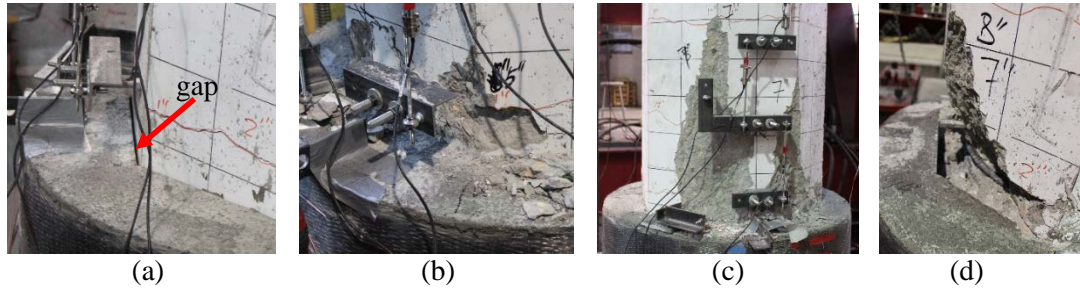


Figure 3.10 Damage of repaired specimen F-CIP-R:(a) gap between column and CFRP donut at 3% drift ratio; (b) column concrete crushing at 5% drift ratio; (c) severe column concrete crushing at 7% drift ratio; (d) final damage.

3.5 Performance of Repaired Specimens

Cumulative hysteretic energy dissipation versus drift ratio is shown in Figure 3.11. At an 8.3% drift ratio, cumulative hysteretic energy of repaired specimens CB-CIP-R and F-CIP-R was 90% and 88% of the original specimens CB-CIP-O and F-CIP-O, respectively. Severe damage of the original specimens contributed to reduced hysteretic energy dissipation. Stiffness degradation of the specimens is shown in Figure 3.12; the stiffness of CB-CIP-R was larger than that of CB-CIP-O, as shown in Figure 3.12(a). The stiffness of F-CIP-R became larger than that of F-CIP-O after a 2% drift ratio, as shown in Figure 3.12(b). Cumulative hysteretic energy and stiffness degradation show that the repair method restored the performance of the repaired specimens to a similar level as the original.

Table 3.2 shows results for the two repaired specimens; the ultimate drift ratio of CB-CIP-R and F-CIP-R was 87% and 95% that of CB-CIP-O and F-CIP-O, respectively. Pinching of the hysteresis curves was observed for the repaired specimens when compared to the original specimens, as shown in Figure 3.8; this was caused by concrete crushing, which reduced the available development length of buckled and fractured bars suffered by the original specimens and the resulting slip between cracked surfaces. The gap created between column and repair concrete started at a 2% to 3% drift ratio when the east and west column faces were damaged inside the donut, as shown in Figs. 3.9(a) and 3.10(a); this was facilitated by the fact that the extreme longitudinal column steel bars near the east and west column faces had already fractured and buckled in the original specimens, as shown in Figs. 3.2(a) and 3.2(b). With increasing cyclic displacements, the column concrete impacted on the repair concrete at CFRP donut top and begun crushing, thus creating a gap. This gap between column and repair concrete widened with increasing drift ratio.

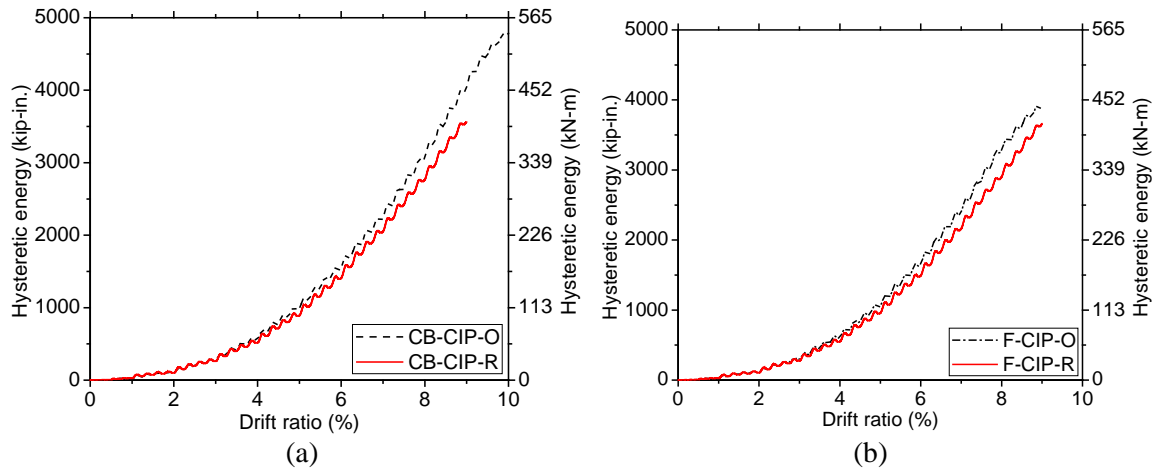


Figure 3.11 Cumulative hysteretic energy: (a) cap beam-to-column specimens; (b) footing-to-column specimens.

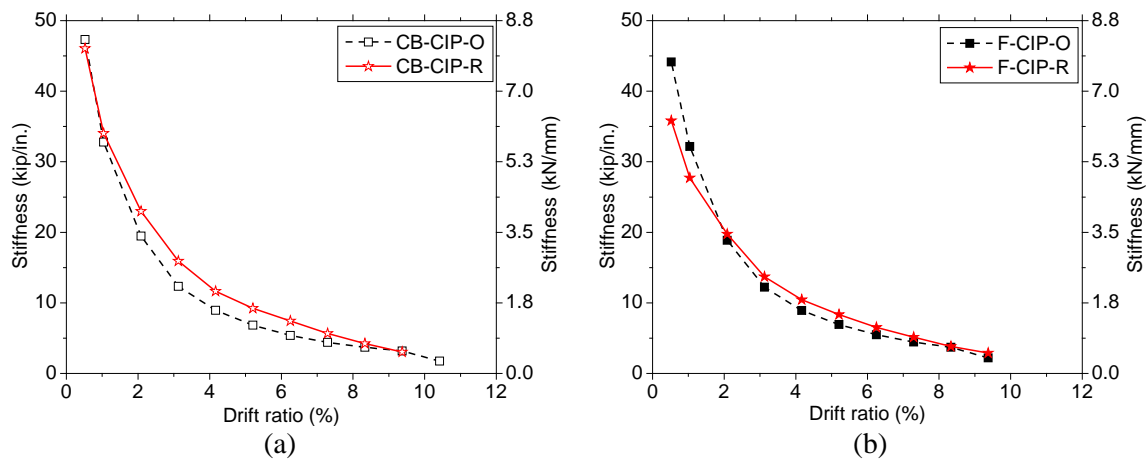


Figure 3.12 Stiffness degradation: (a) cap beam-to-column specimens; (b) footing-to-column specimens.

Performance of the repaired specimens was evaluated in terms of strength and ductility. The backbone curves from experimental data and idealized elastoplastic curves for cap beam and footing specimens are shown in Figs. 3.13(a) and (b), respectively. The yield strength, effective yield displacement, and elastic stiffness of the idealized capacity curves are summarized in Table 3.2. For the repaired specimens, the initial stiffness was determined using the slope of a straight line from the origin to a point at 50% of the peak force from the actual backbone curve (Vosooghi and Saiidi 2010). The elastic stiffness of CB-CIP-R and F-CIP-R was 103% and 85% that of the corresponding original specimens, respectively. The displacement ductility for both repaired specimens exceeded the minimum component displacement ductility equal to 3.0 of Caltrans SDC.

3.5.1 Headed Steel Bar Performance

Strain gauges were placed on the extreme east- and west-headed steel bars 25 mm from the cap beam/footing interface. Figure 3.14 shows the results for CB-CIP-R; the extreme headed bar on the east side reached its peak of 3.4 times the yield strain at a 2% drift ratio. The extreme headed bar on the west

side reached its peak of 2.9 times the yield strain at a drift ratio of 4%. The measured strains confirm that the headed steel bars transfer tensile and compressive forces between the column and cap beam/footing through the CFRP donut.

3.5.2 CFRP Cylindrical Shell Performance

In addition to serving as a form, the CFRP shell provides confinement, circumferential tension, and shear strength. Hoop strain was measured at four levels located at 38, 102, 241 and 356 mm down from the top of the CFRP donut; strain gauges at 38 mm, located at the same level as the head of the headed steel bars, had the maximum strain; this shows that the CFRP shell is under circumferential tension. The hoop strain at 38 mm below the top of the CFRP donut for the two repaired specimens is shown in Figs. 3.15(a) and (b). At a 2% drift ratio, the hoop strain reached 0.20% for both specimens. For CB-CIP-R, the hoop strain at a 6% drift ratio reached a maximum value of 0.45%, as shown in Figure 3.15(a). The corresponding hoop stress was 292 MPa, which exceeds the predicted value of 251 MPa from the FEM model of Figure 3.3, but is less than the allowable CFRP ultimate stress of 452 MPa. The hoop strain of the east side of specimen F-CIP-R at a 7% drift ratio reached a maximum value of 0.49%, as shown in Figure 3.15(b).

The hoop strain profiles for specimen CB-CIP-R and F-CIP-R are shown in Figs. 3.16(a) and (b), respectively. The hoop strain increased from bottom to top of the CFRP shell. The hoop strain at the top 152 mm of the CFRP shell ranged from 0.2 to 0.5%; this shows that the CFRP shell formed an effective tension ring. Strain in the vertical CFRP layers was measured at the same elevation as the hoop strain. Figures 3.17(a) and (b) show the vertical strain profile for specimens CB-CIP-R and F-CIP-R, respectively. The maximum strain of the vertical CFRP layers for specimen CB-CIP-R was 0.16% in compression and 0.04% in tension, as shown in Figure 3.17(a). The maximum strain of the vertical CFRP layers for specimen F-CIP-R was 0.23% in compression and 0.08% in tension, as shown in Figure 3.17(b). The maximum vertical strains occurred 102 mm below the CFRP donut top.

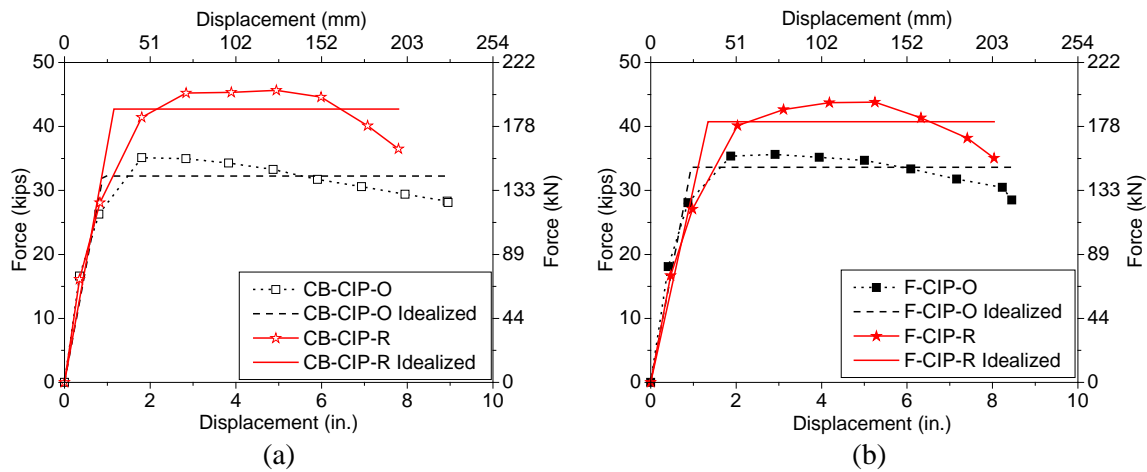


Figure 3.13 Backbone and idealized force-displacement relationships for: (a) cap beam; (b) footing specimens.

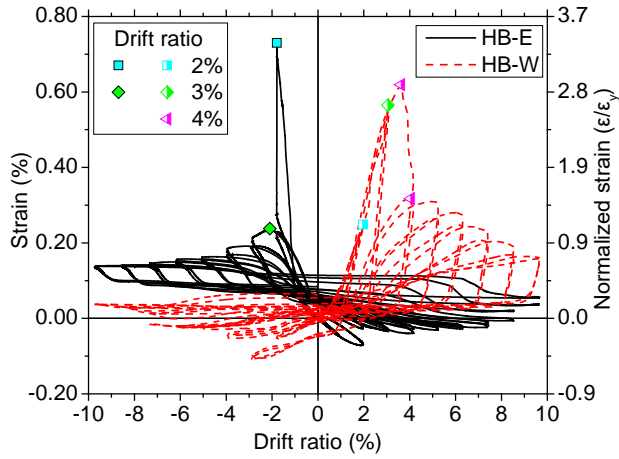


Figure 3.14 Headed steel bar longitudinal strain of cap beam specimen CB-CIP-R.

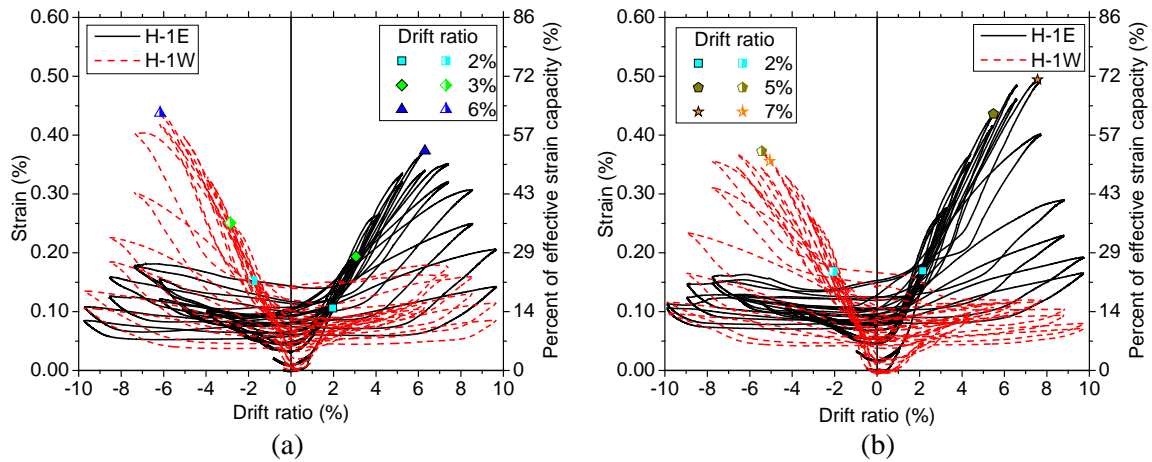


Figure 3.15 CFRP hoop strain 38 mm below CFRP donut top for specimens: (a) CB-CIP-R; (b) F-CIP-R.

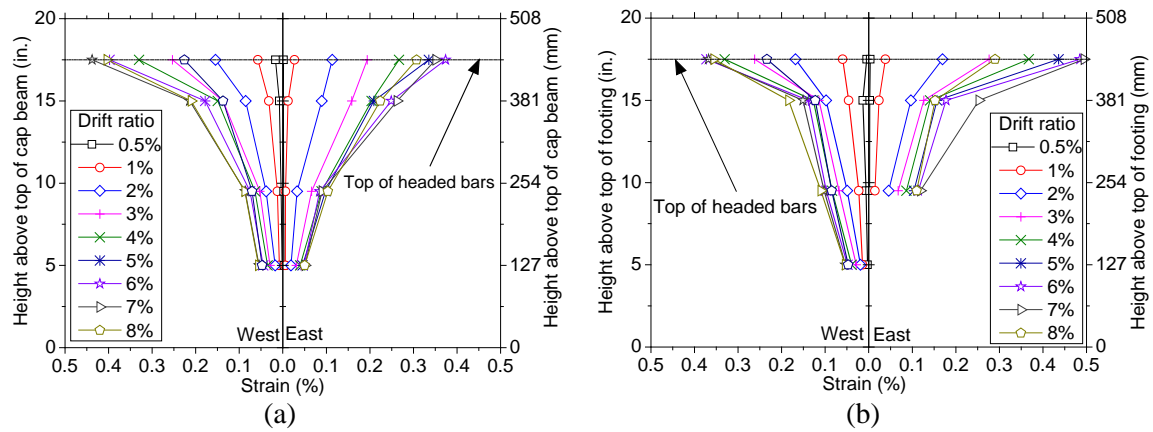


Figure 3.16 Measured hoop strain distribution of CFRP shell for specimens: (a) CB-CIP-R; (b) F-CIP-R.

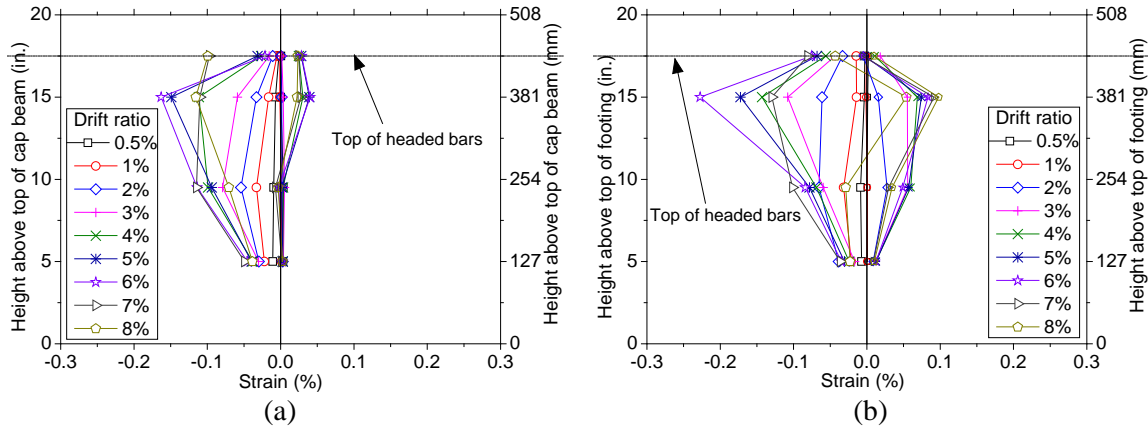


Figure 3.17 Measured vertical strain distribution of CFRP shell for specimens: (a) CB-CIP-R; (b) F-CIP-R.

3.5.3 Moment-Plastic Rotation

Plastic rotation was calculated by dividing the plastic displacement by the column height. Plastic displacement was taken as the difference between total and yield displacement using the idealized backbone curve of Figure 3.13. A comparison of bending moment versus plastic rotation between repaired and original specimens is shown in Figure 3.18. The bending moment capacity of the repaired specimens is larger than the moment capacity of the original specimens. The ultimate plastic rotation of the two repaired specimens was 0.085 rad, which is 89% and 96% of the original specimens CB-CIP-O and F-CIP-O, respectively. Both repaired specimens show good rotation capacity, which meets the acceptance criteria of 0.060 rad for the Collapse Performance (CP) level specified in ASCE/SEI 41 (American Society of Civil Engineers 2013).

3.6 Development of Numerical Model

3.6.1 Model Fiber

Bond-slip effects must be considered to accurately determine the structural response, since bond slip failure occurs in most RC concrete structures, especially poorly confined concrete joints (Harajli 2009). When repairing a severely damaged structure, the bond-slip between damaged longitudinal steel bars and surrounding concrete is critical for accurately determining the structural response. Damaged steel properties could be implemented with a reduction in the elastic modulus according to the maximum steel bar strain experienced by the original members (Vosooghi and Saiidi 2013). Several models with modified steel properties have been developed to consider bond-slip behavior in the analysis (D'Amato et al. 2012; Zhao and Sritharan 2007; Ameli and Pantelides 2016). One method is to modify the steel properties based on assumed bond-slip relationships and use a modified steel constitutive curve in the numerical model (Wu and Pantelides 2018).

Little research exists regarding numerical models considering bond-slip, longitudinal bar fracture/buckling, and damaged concrete for repaired RC column-to-cap beam/footing connections. In addition, low-cycle fatigue of damaged longitudinal steel bars should be considered in the analysis, since the longitudinal steel bars of the original members experienced yielding and post-yielding strain. A model is proposed to address the aforementioned factors for the repaired RC connections. The bond-slip effect was considered in the distributed plasticity element.

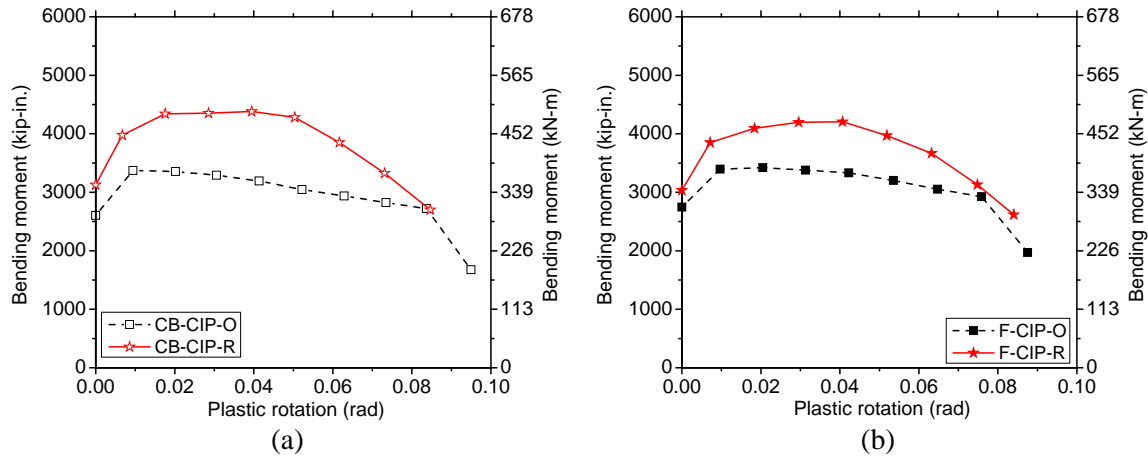


Figure 3.18 Moment versus plastic rotation for specimens: (a) column-to-cap beam; (b) column-to-footing.

A schematic of the fiber model for the repaired column is shown in Figure 3.19. The octagonal column was approximated by a circular section of equal cross-sectional area to simplify discretization. There were 40 circumferential subdivisions for the core concrete, cover concrete and CFRP confined concrete; and 20, 5, and 10 radial subdivisions for the core concrete, cover concrete, and CFRP confined concrete, respectively. The *Concrete04* material model was used to model steel-confined concrete and cover concrete based on Mander’s steel-confined concrete model (Mander et al. 1988). CFRP confined concrete was implemented in the *Concrete01* material model, which was calculated based on the recommendations of ACI Committee 440 (ACI440 2015).

3.6.2 Distributed Plasticity over Plastic Hinge Length

In Model Fiber, distributed plasticity considering bond-slip is assumed to be concentrated in the plastic hinge length of the non-linear beam-column element instead of the total length of the element. This was implemented using the *BeamWithHinges* element (Scott and Fenves 2006). In this element, incorporation of a plastic hinge length in the element integration method ensures an objective element and sectional response, which is important for strain-softening behavior in RC structures. The two-point Gauss–Radau integration rule was applied over a length equal to four times the plastic hinge length at the element ends. One benefit of this element is its ability to control the plastic hinge length, L_{pl} , which can be determined based on the damaged regions observed from tests or empirical relationships from the literature (Panagiotakos and Fardis 2001).

3.6.3 Bond-slip Model for Modified Steel

To consider the bond-slip effects in Model Fiber, a one-dimensional bond-slip model, as shown in Figure 3.20, was developed based on recent research (Ameli and Pantelides 2016). In this bond-slip model, longitudinal steel bars with *damaged steel* properties were discretized and connected to bond-slip springs, modeled using the *ZeroLength Element*. The bond stress-slip relationships in the bond-slip springs were obtained from the CEB-FIB Code in the case of splitting mode failure (CEB-FIP 1993, 2012). For the length of steel bars embedded in the previously damaged region, the bond stress-slip relationship for unconfined concrete was used for bond-slip spring elements; for the remaining length of steel bars outside the previously damaged region, the bond stress-slip relationship for confined concrete was used for bond-

slip spring elements. Bond stress-slip relationships for confined and unconfined concrete used for specimen CB-CIP-R are shown in Figure 3.21.

In the one-dimensional bond-slip model, one end of the steel bar was pulled to get the total deformation, including steel bar elongation and slip. Total deformation of the steel bar, Δs , is the sum of the corresponding total deformation from both the column part and the cap beam or footing part, as shown in Eq. (3.2) (D'Amato et al. 2012):

$$\Delta s = \Delta s_A + \Delta s_B \quad (3.2)$$

where Δs = total deformation of steel bar; Δs_A = deformation of steel bar in the column; and Δs_B = deformation of steel bar in the cap beam or footing, as indicated in Figure 3.20. The total deformation of the steel bar, Δs , including elongation and slip was obtained. The steel strain, ε , was calculated based on Eq. (3.3):

$$\varepsilon = \Delta s / L_{pl} \quad (3.3)$$

where ε = steel strain; and L_{pl} = plastic hinge length. In Model Fiber, 356 mm, or 67% of the column width, was used for the defined plastic hinge length of cast-in-place specimens CB-CIP-R and F-CIP-R.

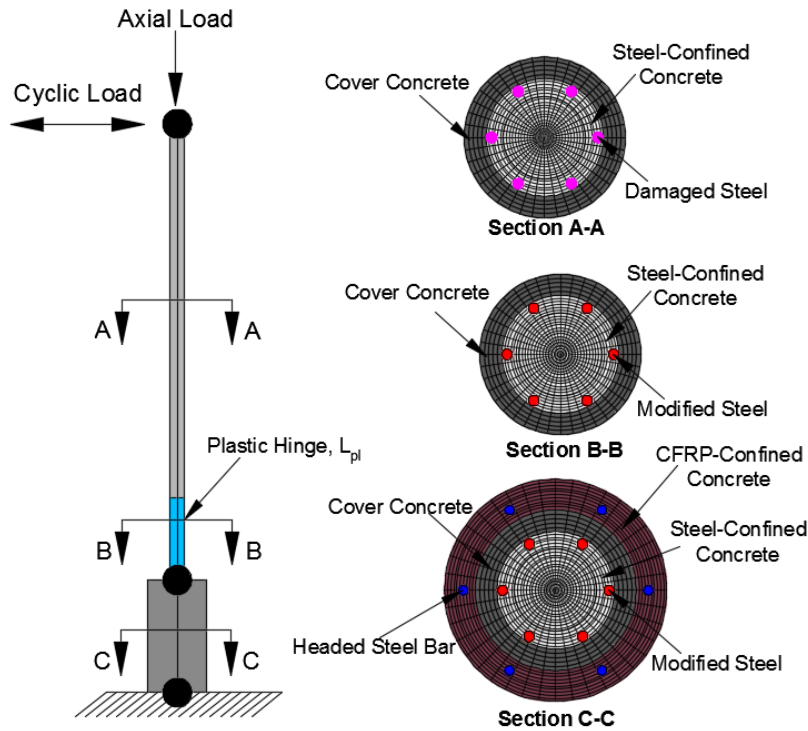


Figure 3.19 Schematic of Model Fiber.

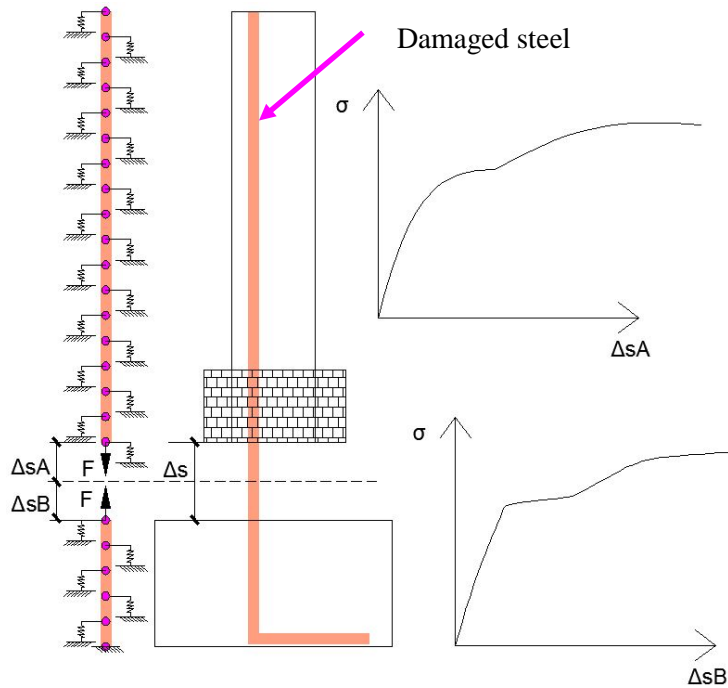


Figure 3.20 Schematic of bond-slip springs model.

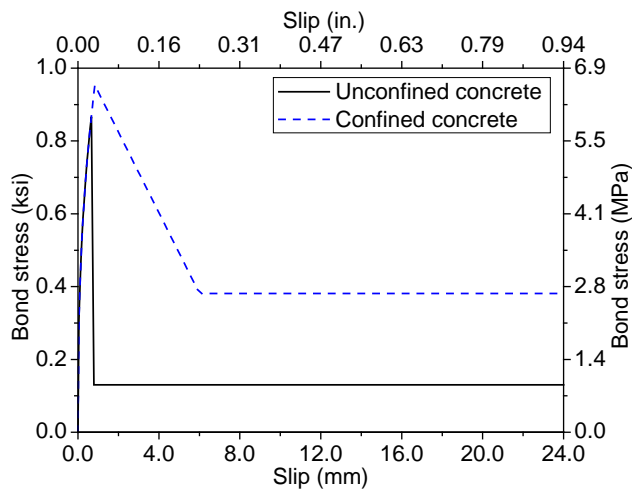


Figure 3.21 Bond stress-slip curves used in bond-slip springs model for CB-CIP-R.

The *modified steel* stress-strain curve with consideration of initial damage and bond-slip is obtained, which was used for steel bars in the defined plastic hinge region and CFRP donut cross-section of Model Fiber. The elastic modulus of *modified steel* was 0.33 times the original steel elastic modulus for specimens CB-CIP-R and F-CIP-R.

The *Hysteretic Material* available in *OpenSEEs* was used to model longitudinal steel bars in Model Fiber. In the defined *modified steel* stress-strain curve, although the columns are well-confined, buckling of the

steel bars in compression was also considered using the method proposed by Dhakal and Maekawa (2002).

3.6.4 Low-Cycle Fatigue

In Model Fiber, the *fatigue* material in *OpenSEEs* was used to consider the accumulation of low-cycle fatigue damage in the longitudinal steel bars (Uriz and Mahin 2008). Since the column longitudinal steel bars had experienced high strains in the original specimen tests, it was necessary to consider the cumulative strain in the analysis of the repaired specimens to obtain the accumulated damage of the longitudinal steel bars. A cumulative linear damage rule from the Coffin-Manson expression was incorporated in the *fatigue* material, as shown in Eqs. (3.4) and (3.5), respectively (Kunnath et al. 2009):

$$\varepsilon_i = \varepsilon_0 (2N_f)^{-m} \quad (3.4)$$

$$D_f = 1 / \sum_{i=1}^n (2N_f)_i \quad (3.5)$$

where ε_i = total strain range ($\varepsilon_{\max} - \varepsilon_{\min}$) at cycle i ; ε_0 = value of strain at which one cycle will cause failure; $2N_f$ = number of half-cycles to failure; m = material constant related to the slope of the Coffin-Manson curve in log-log space; and D_f = accumulated fatigue damage. In this study, a value ε_0 of 0.25 was used for specimens CB-CIP-R and F-CIP-R. In addition, a value of m equal to 0.36 was used for the repaired specimens, based on previous recommendations (Kunnath and Brown 2004; Uriz and Mahin 2008). A large value of ε_0 implies less accumulated fatigue damage.

3.7 Numerical Results and Comparisons to Experiments

The results from the numerical model compared to the experiments are shown in Figs. 3.22-3.24, in terms of hysteretic response, cumulative hysteretic energy, and moment-rotation relationships.

3.7.1 Hysteretic Response

Hysteresis results from numerical analysis were compared to experimental results for the repaired specimens, as shown in Figure 3.22. Model Fiber predicted the backbone curve very well, capturing important characteristics. For repaired cast-in-place specimens CB-CIP-R and F-CIP-R, Model Fiber captured the pinching behavior of the hysteresis, as shown in Figure 3.22. For repaired CIP specimens with pinching and severe bond-slip due to debonding between the column and repair system, Model Fiber is appropriate for simulating the structural behavior.

3.7.2 Cumulative Hysteretic Energy

Cumulative hysteretic energy versus drift ratio from the numerical model was superimposed with the experimental results for the repaired specimens, as shown in Figure 3.23. The results from Model Fiber are in very good agreement with the corresponding experiments. The error in cumulative hysteretic energy between numerical models and experiments at each drift ratio was less than 5%.

3.7.3 Moment-Rotation Response

In this analysis, moment-rotation results from Model Fiber were obtained as output. The moment-rotation relationships from Model Fiber were compared to the experimental results measured using linear variable differential transformers (LVDTs) for the repaired specimens, as shown in Figure 3.24. The LVDTs were removed at the 6% drift ratio in the tests, which explains missing data shortly after the peak moment in

the experiments. The moment-rotation results obtained from Model Fiber not only matched the experimental results, but also predicted the behavior after the peak moment was reached.

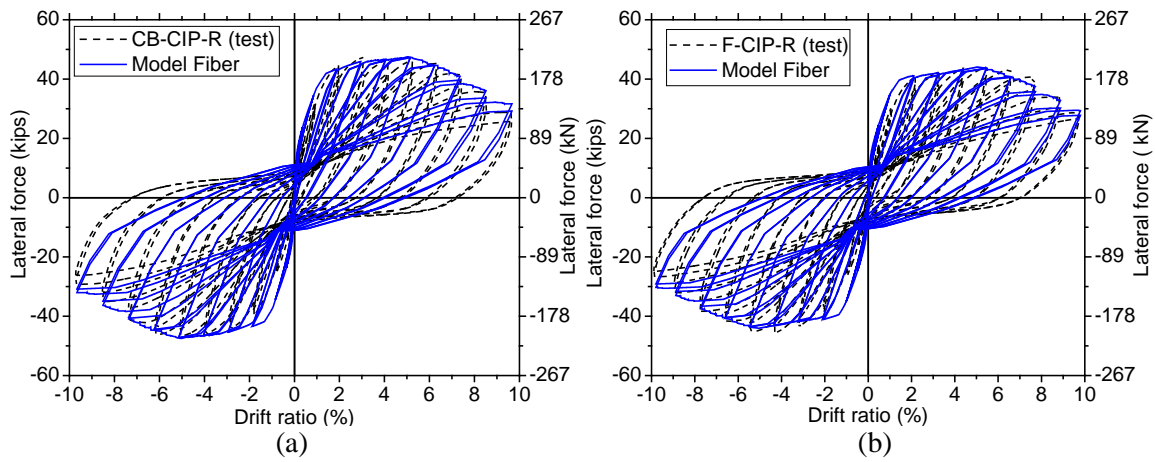


Figure 3.22 Hysteretic response of repaired CIP specimens: (a) Model Fiber and test for CB-CIP-R; (b) Model Fiber and test for F-CIP-R.

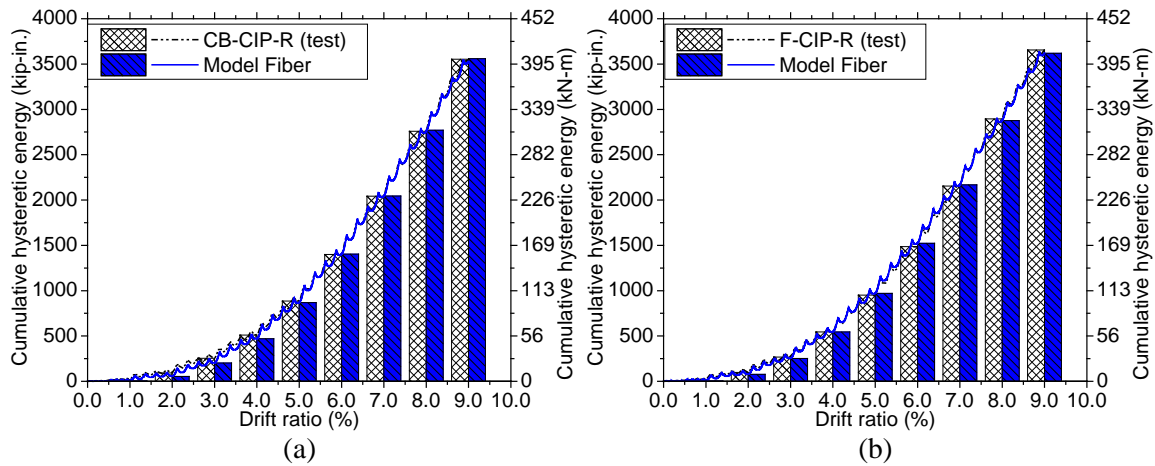


Figure 3.23 Cumulative hysteretic energy comparisons: (a) CB-CIP-R; (b) F-CIP-R.

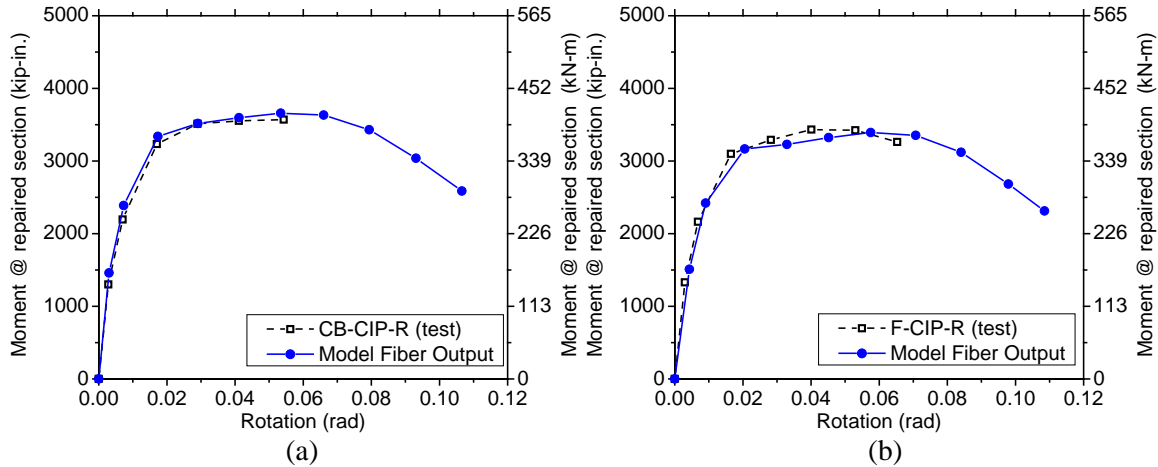


Figure 3.24 Moment-rotation response comparisons: (a) CB-CIP-R; (b) F-CIP-R.

3.7.4 Accumulated Low-Cycle Fatigue Damage

Low-cycle fatigue of column longitudinal steel bars was incorporated in Model Fiber. The fatigue damage of the two extreme longitudinal steel bars in the loading direction was obtained for the repaired specimens, as shown in Figure 3.25. According to the definition of accumulated fatigue damage in the *fatigue* material, a steel bar fractures when the fatigue damage reaches a value equal to 1.0. For specimens CB-CIP-R and F-CIP-R, the maximum fatigue damage of two extreme steel bars was 0.6 and 0.7, respectively, which is less than 1.0; this is consistent with the experiments during which there was no fracture of longitudinal steel bars.

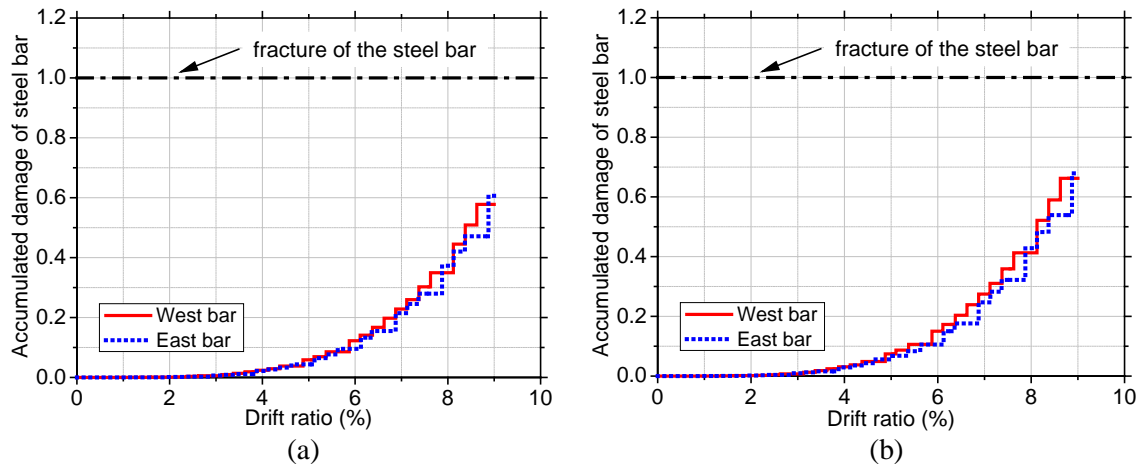


Figure 3.25 Low-cycle fatigue of two extreme column longitudinal steel bars from Model Fiber: (a) CB-CIP-R; (b) F-CIP-R.

4. SEISMIC RETROFIT OF A MULTI SPAN SIMPLY SUPPORTED CURVED BRIDGE WITH THREE-COLUMN BENTS

4.1 Description of Bridge

A four span simply-supported curved bridge was designed based on the reinforcing details and dimensions of the three-column bridge bent tested in-situ by Pantelides et al. (1999). The original bridge was constructed in Salt Lake City in 1963 and was designed for gravity and wind loads but not for seismic loads. Several bents of this bridge were retrofitted with CFRP jackets and tested under quasi-static cyclic loads. The measured in-situ concrete compressive strength was $f'_c = 34$ MPa and the yield strength of the mild steel reinforcement $f_y = 336$ MPa.

4.1.1 Superstructure and Substructure

Figure 4.1 shows the plan and elevation of the proposed bridge structure with curvature radius of 137 m and total length of 88 m. The superstructure is a concrete slab supported on eight steel girders through steel studs. Each span has a length of 22 m; steel girders are simply supported at the cap beams on both ends with bearings, as shown in Figure 4.2. Intermediate steel diaphragms are provided every 5.5 m along the length of the bridge and end diaphragms are provided at the supports. Figure 4.3 shows an elevation of bent 2 (identical to bent #5S of the bridge tested by Pantelides et al. 1999, and compared in Pantelides and Fitzsimmons 2012). A typical bent consists of three columns with a 7.310 m clear height and a cross-section of 914 x 0.914 mm. The columns are 7.260 m apart at their center and the cap beam has a 0.914 x 1.219 m cross-section. All columns were reinforced with 16 – 32 mm longitudinal bars and 13 mm single square hoops spaced at 305 mm; these reinforcement details, as shown in Figure 4.4, do not meet current AASHTO (2014) seismic design criteria.

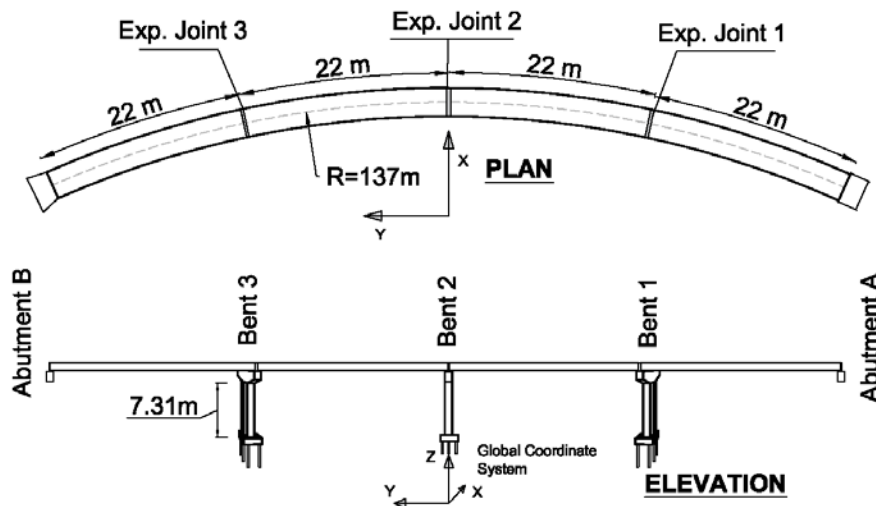


Figure 4.1 Plan and elevation of the bridge.

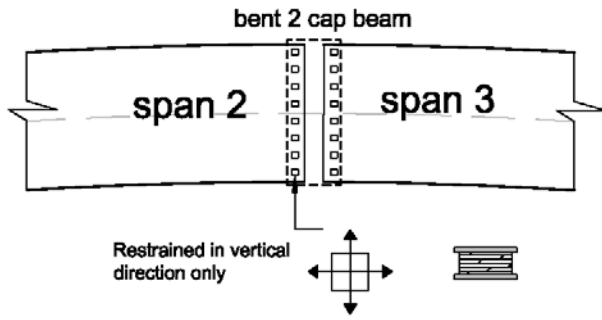


Figure 4.2 Bearings of the original bridge.

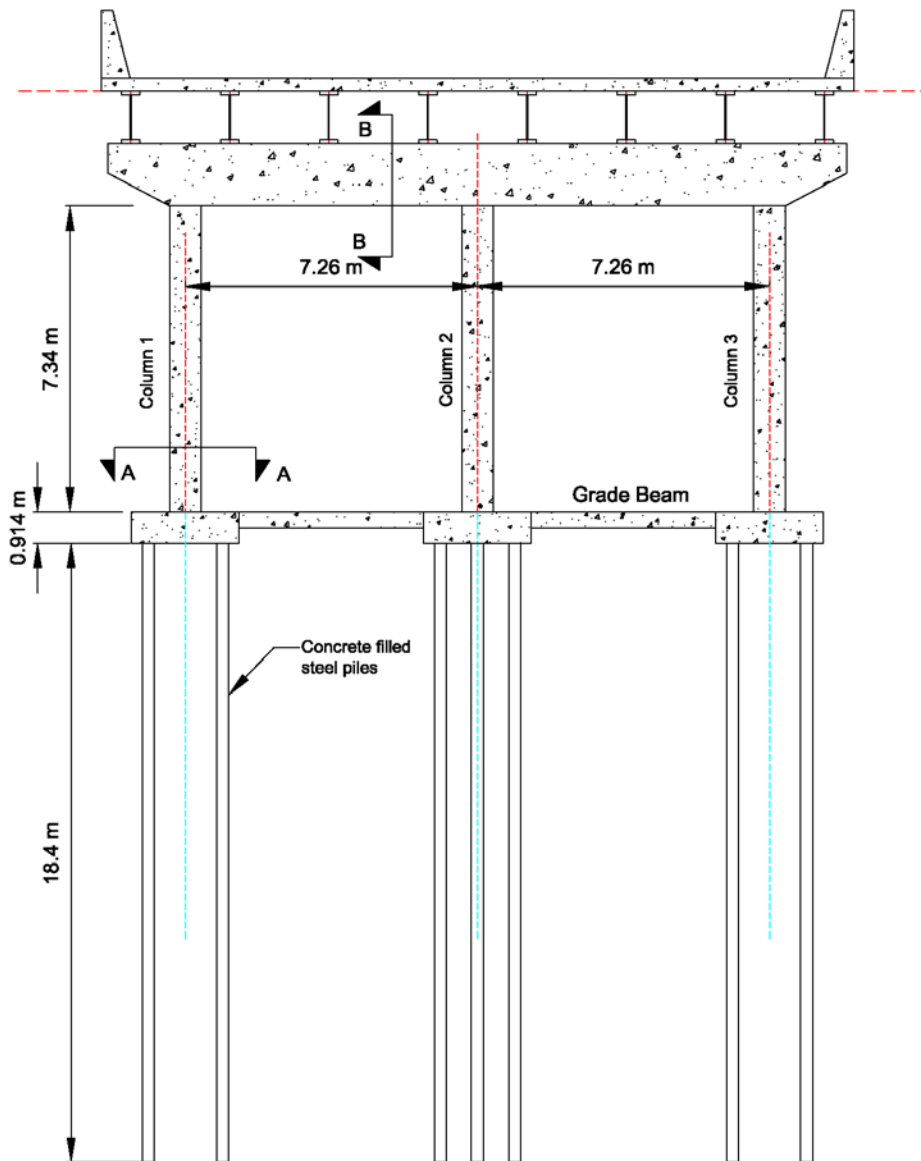


Figure 4.3 Elevation of Bent 2.

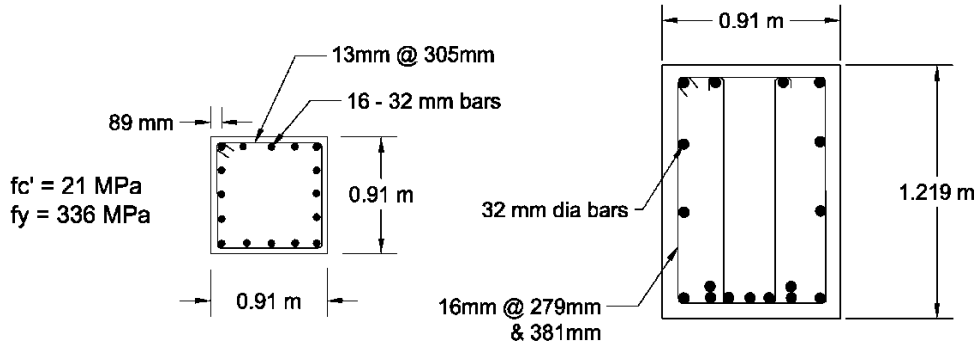


Figure 4.4 Sectional details: (a) Column (Sec. A-A); (b) Cap beam (Sec. B-B).

The cross-sectional area of the transverse reinforcement is only 43% of the area required. The lap-splices of the column longitudinal reinforcement consist of a length of 24 bar diameters and are located in the plastic hinge region at the column base. The requirements for column hoops of a closed tie with 135° angle are not met. In addition, no transverse shear reinforcement is provided in the T-joints. It is clear that the columns lacked confinement in the plastic hinge region. The cap beam has sufficient shear reinforcement in the middle, but the longitudinal reinforcement in the cap beam-to-column joints does not have adequate anchorage length.

4.1.2 Foundations and Soil Description

The columns were supported on 914 mm thick pile caps. The two exterior pile caps were supported on four 0.30 m diameter concrete filled steel piles, 18.30 m deep. The interior pile cap was supported on five piles. The pile caps were connected by a concrete strut (460 x 460 mm) reinforced with 4x25 mm steel bars and 13 mm stirrups spaced at 457 mm. No shear reinforcement existed in the pile caps. Pile flexural reinforcement was present only at the bottom of the pile cap, which did not have sufficient development length thus making it vulnerable to pullout failure.

4.2 Numerical Model

A non-linear numerical analysis model of the bridge was developed using *OpenSEEs* (Mckenna 2014) as shown in Figure 4.5. The columns and cap beam were modeled using nonlinear force-based beam-column elements with fiber sections discretized at four integration points to capture nonlinear response. It was assumed that the cap beam-column and column-pile cap joints were strong enough to withstand the shear forces. No material degradation at the joints was considered. The total deck weight was 3038 kN, which was distributed and applied vertically downwards on the top nodes of the columns. Column and cap beam fiber sections are shown in Figure 4.5. Columns were assumed to attract more damage due to the strong beam-weak column design philosophy; column sections in the numerical model had a larger number of fibers than the beam sections. Column cores and the cap beam were assigned material properties of confined concrete using the “Concrete04” material model. The Concrete04 material model is capable of simulating crushing of concrete leading to loss of strength in further cycles. Reinforcing bars were modeled using the ‘ReinforcingSteel’ material model in *OpenSEEs* due to its ability to simulate buckling of steel bars, cyclic degradation of stiffness, and fatigue failure.

The ends of the cap beam and columns were modeled with rigid elastic elements to represent connection lengths. Pile-caps were modeled as lumped mass at one node for each pile-cap. Slave nodes were modeled at the joints of the piles and the pile-cap. These slave nodes were connected to the main pile-cap node using rigid elements to simulate the behavior of the rigid pile-cap. Piles were modeled using elastic beam-column elements since no significant damage to piles was expected. Soil-pile interaction was modeled

using non-linear P-y springs with dashpots at each 0.30 m of the pile depth. The “PySimple1” material available in OpenSEEs with zero-length elements was used to model the lateral springs for soil-pile interaction. Vertical springs were modeled using the “TzSimple1” material model to represent friction resistance of piles against vertical loads. Pile tip resistance was modeled with a vertical spring using a “QzSimple1” material. The numerical analysis model is shown in three-dimensions in Figure 4.6.

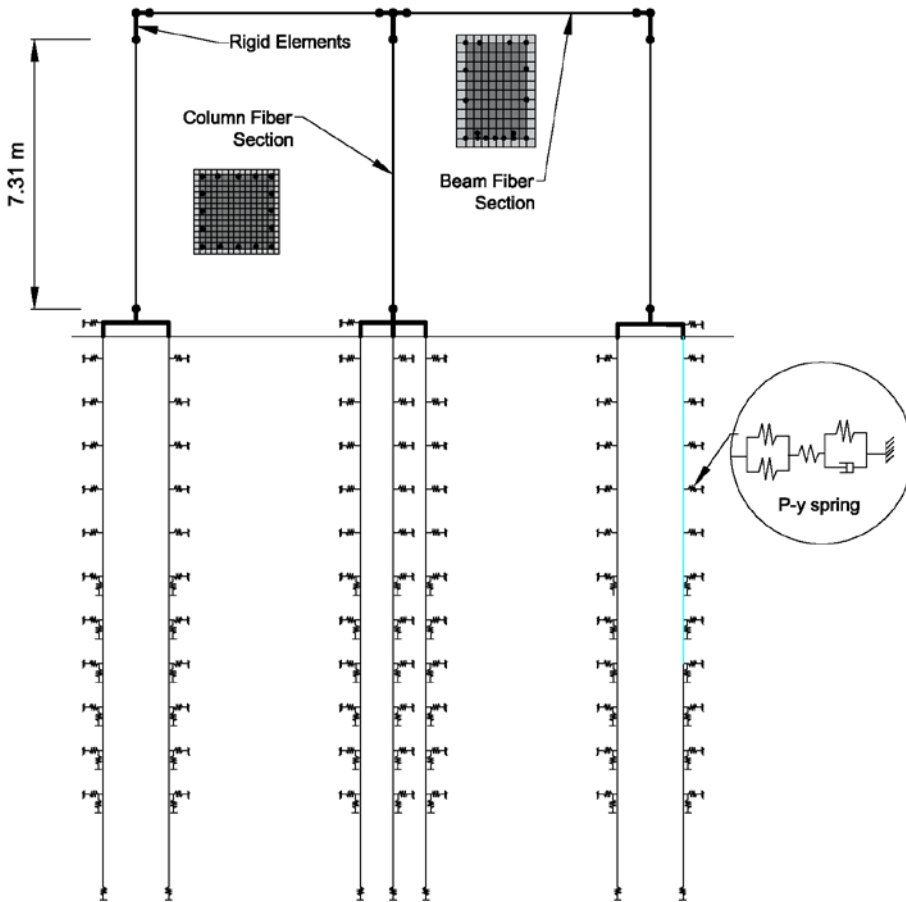


Figure 4.5 Numerical model of one of the bents.

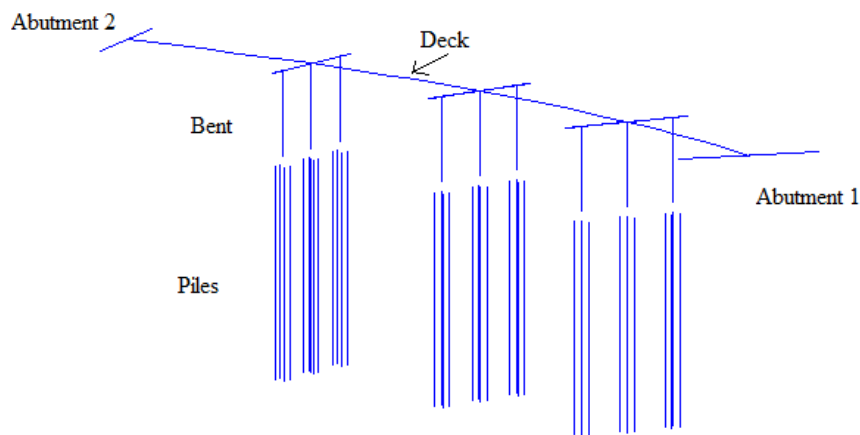
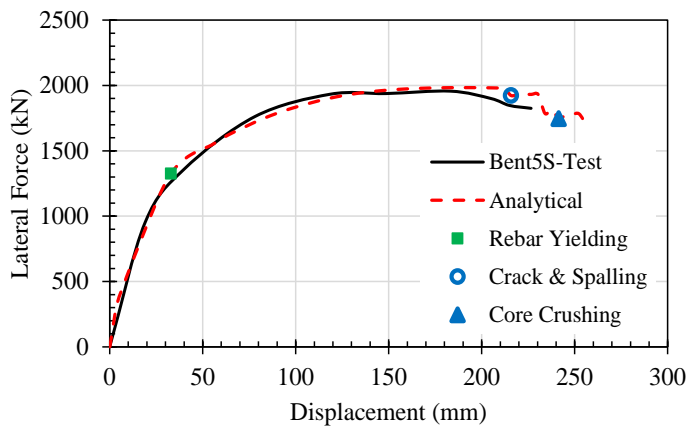


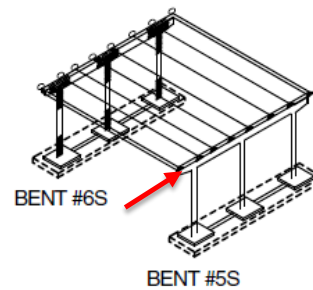
Figure 4.6 Numerical model of curved bridge rendered in MATLAB.

4.3 Model Validation

Pushover analysis was performed by statically loading the cap beam of bent 2. The results were compared to the test output for bent 5S test (Pantelides et al. 1999; and Pantelides and Fitzsimmons 2012). Only half the deck load was used in the pushover analysis to simulate test conditions in Figure 4.7(b). The numerical model captures the behavior of Bent 5S accurately, as shown in Figure 4.7(a). Cover cracking and spalling occurred at a cap beam displacement of 215 mm (2.90% drift ratio) and the extreme fiber of the column core concrete crushed at 240 mm (3.28% drift ratio). In the field test, the observed peak load was 1956 kN at a displacement of 182 mm, while the numerical model estimate was a peak load of 1985 kN at a displacement of 212 mm; the load dropped due to core concrete crushing instead of gradual reduction in load after 182 mm, as observed in the test. Lateral movement of the pile cap during the pushover in the numerical model was compared with the monitored pile cap displacement in the field test. Figure 4.8 shows that the numerical model captured the soil behavior closely.



(a)



(b)

Figure 4.7 Model validation: (a) comparison of numerical pushover analysis curve with experimental data; (b) test setup for bent 5S with half deck load.

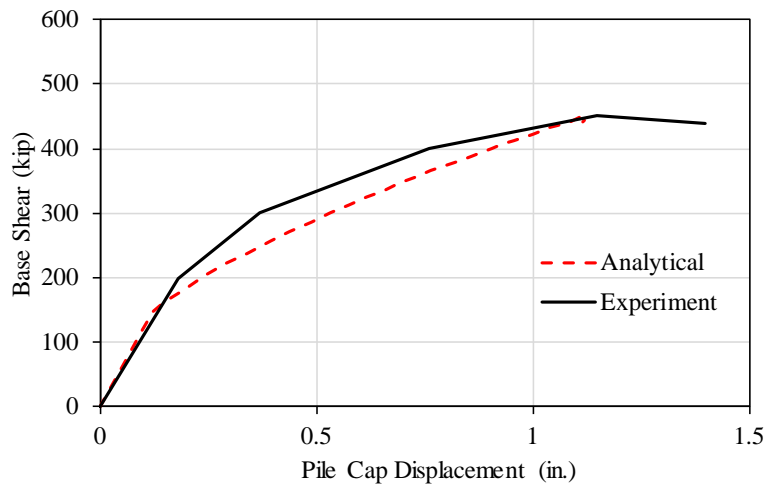


Figure 4.8 Comparison of pile cap displacement of numerical pushover analysis with experimental data.

Another static pushover analysis was performed using the numerical model with the full deck load to simulate the real conditions of the bridge. Figure 4.9 shows the effect of adding a full deck load on the bridge bent performance and lateral load capacity. The additional dead load enhanced P-delta effects and reduced the concrete crushing drift ratio from 3.2% to 2.5%, while increasing the peak lateral load capacity from 1985 kN to 2093 kN. This full load condition will be used in subsequent numerical analysis.

4.3.1 BRB and SCED Model Validation

The Buckling Restrained Brace (BRB) member was modeled using a two-node link element with “Steel02” (Giuffré-Menegotto-Pinto with isotropic strain hardening material model) available in *OpenSEEs*. The BRB analysis model was validated against a BRB test conducted by Xu (2017) at the University of Utah. Figure 4.10(a) shows a comparison of the *OpenSEEs* model and the BRB test. The Self-Centering Energy Dissipation (SCED) member was modeled using a two-node link element with “self-centering material.” The numerical analysis model requires the initial stiffness, secondary stiffness, and activation force as inputs. The model was validated against the test performed by Christopoulos (2008). Figure 4.10(b) shows that the numerical model captured the SCED behavior accurately.

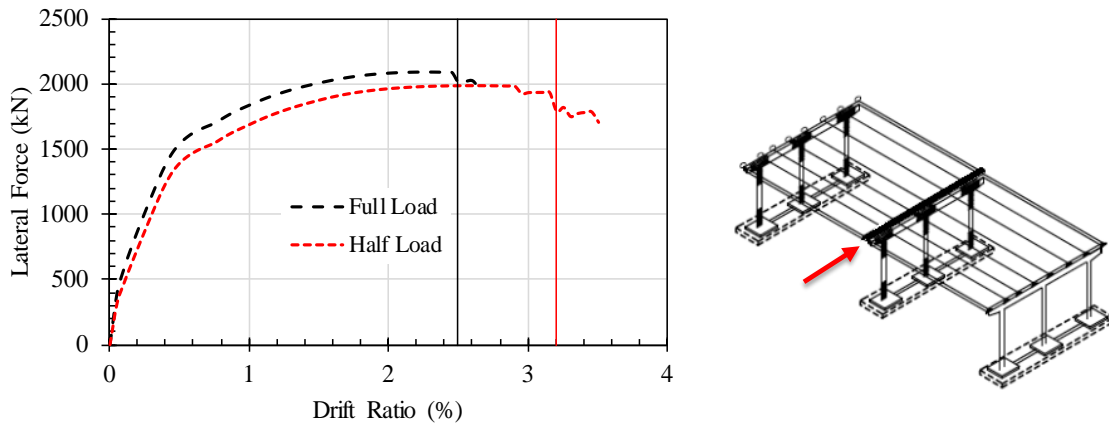


Figure 4.9 Comparison of lateral load capacity of numerical model of the bridge bent with half deck load (Pantelides et al. 1999) and full deck load.

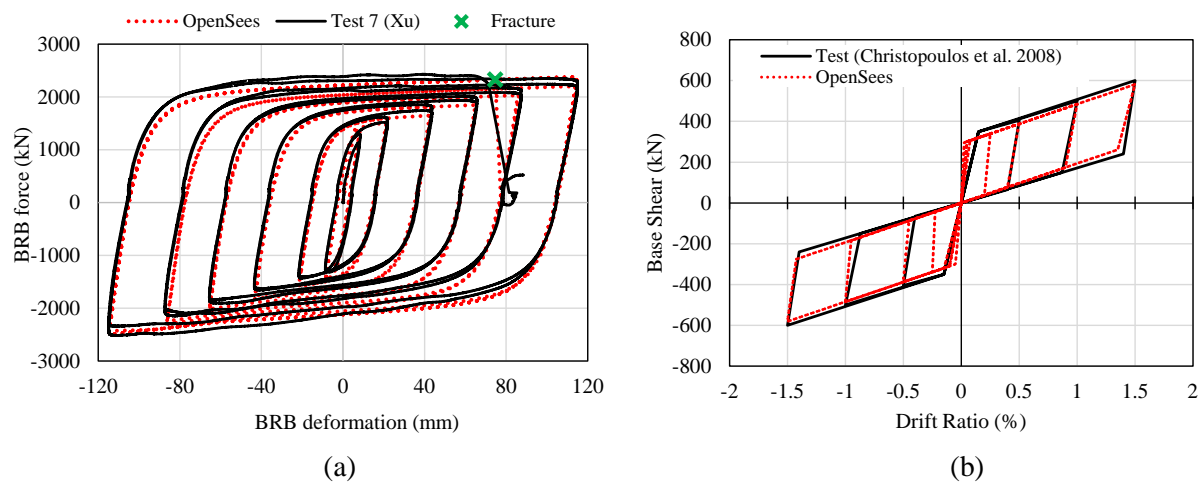


Figure 4.10 Validation of numerical model for: (a) BRB; (b) SCED.

4.3.2 Performance Criteria

Non-linear time-history analyses using far-field and near-field ground motions were performed to assess the seismic demand on the three-dimensional model of the curved bridge. The curved bridge performance obtained from the numerical analyses was compared to limit states. For this study, drift limit states from Vision 2000 (OES 1995) were used to assess bridge performance. Vision 2000 defines four performance levels based on drift ratio: (1) fully operational up to 0.2% drift, (2) operational up to 0.5% drift, (3) life safety up to 1.5% drift, and (4) near collapse up to 2.5% drift. Table 4-1 describes the performance states in detail. In this study, operational and fully operational limit states were consolidated and only three drift limit states were used as shown in Table 4-2.

Table 4.1 Performance states of Vision 2000.

Performance	Description
Fully Operational	Continuous service. Negligible structural and nonstructural damage.
Operational	Most operations and functions can resume immediately. Structure safe for occupancy. Essential operations protected, non-essential operations disrupted. Repair required to restore some non-essential services. Damage is light.
Life Safety	Damage is moderate, but structure remains stable. Selected building systems, features, or contents may be protected from damage. Life safety is generally protected. Structure may be evacuated following earthquake. Repair possible, but may be economically impractical.
Near Collapse	Damage severe, but structural collapse prevented. Nonstructural elements may fall. Repair generally not possible.

Table 4.2 Drift limits for performance criteria.

Performance State	Permissible Max. Limit	Permissible Residual Drift	Concrete Strain	Rebar Strain
Operational	0.5%	Negligible	0.004	0.015
Life Safety	1.5%	0.5%	0.018	0.06
Near Collapse	2.5%	2.5%	-	-

4.4 Mode Shapes

The fundamental mode of vibration for the curved bridge was longitudinal translation with $T_1 = 0.39s$ as shown in Figure 4.11. The second mode of vibration was translation in the transverse direction with $T_2 = 0.36s$. The third mode ($T_3 = 0.31s$) was rotation about the middle bent (bent 2) pushing bent 1 and bent 3 on either side. This mode is expected due to the bridge's curvature. The fourth and sixth modes show translation in the longitudinal direction but are dominated by gap opening at the expansion joints. This shows that the bridge deck is expected to have pounding damage at the expansion joints. The fifth mode is translation in the lateral direction with all bents vibrating out-of-phase.

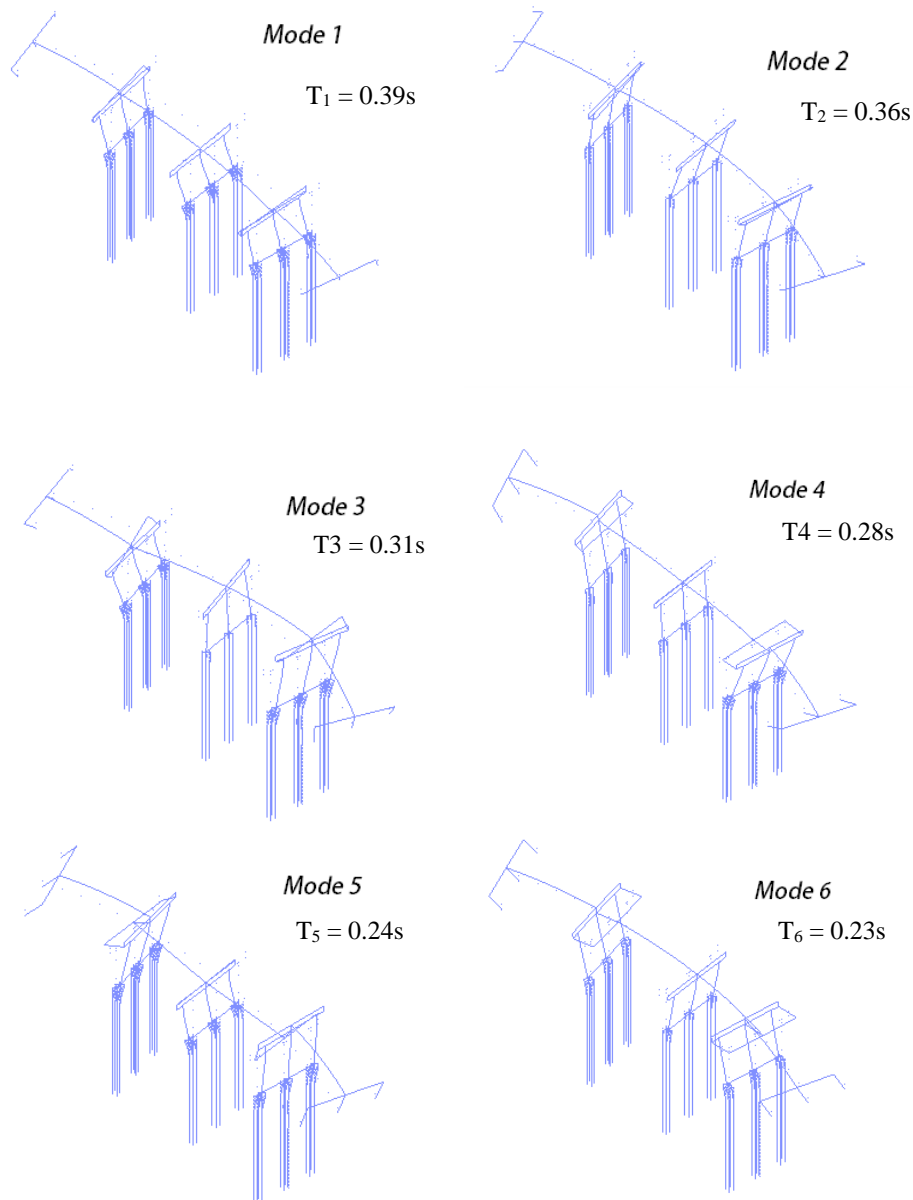
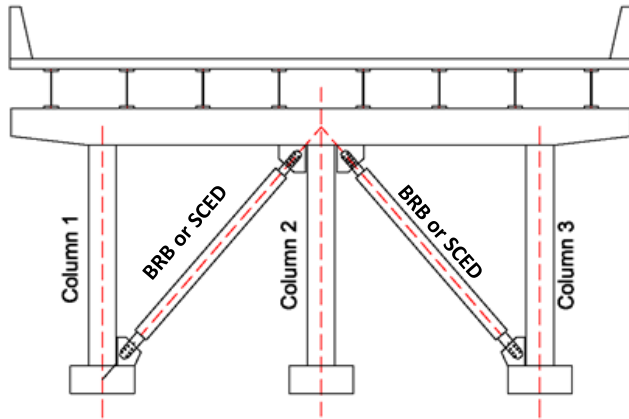


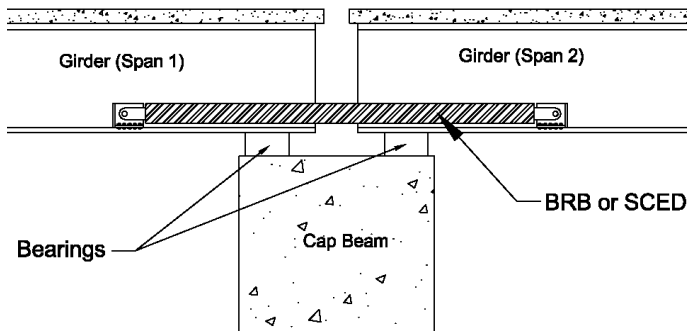
Figure 4.11 First six mode shapes of as-built curved bridge.

4.5 Seismic Retrofit Scheme

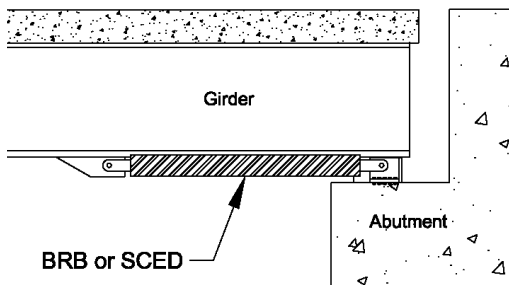
The proposed seismic retrofit scheme for the curved bridge included adding BRBs or SCEDs between columns of the bridge bents for lateral strengthening as shown in Fig 4.12(a). To prevent structural pounding between the girders at the expansion joints of the bridge and at the abutment, longitudinal BRBs/SCEDs were implemented. Figures 4.12(b) and (c) show the seismic retrofit scheme at the expansion joints and abutments, respectively.



(a)



(b)



(c)

Figure 4.12 Seismic retrofit scheme for bridge with BRBs or SCEDs: (a) for individual bent; (b) at expansion joints; (c) at abutments.

4.6 Non-linear Time-history Analysis

4.6.1 Deck Bearing Modification

The girders in the original bridge were simply supported on a steel plate embedded on top of the cap beam with a square piece of thick steel plate acting as the bearing. This support was sufficient for the bridge under dead and live loads, but could lead to unseating of the deck for lateral loads during an

earthquake. The Kobe (1995) ground motion scaled to the design earthquake (DBE) level at the site ($S_a = 0.991g$) was applied in the transverse direction of the simply supported bridge. Figure 4.13 shows the lateral displacement of the bent 2 cap beam, and deck span 2 and span 3, which were supported on bent 2. As expected, the decks slid on the cap beam since the bearings were not restrained. Figures 4.14(a) and (b) confirm the large deformations at the bearings. This leads to large residual lateral displacements of the deck segments relative to the bent. For the MCE level ground motion, the bridge would be vulnerable to unseating of the deck.

The first step towards seismic retrofit is to relocate damage to the column ends. To achieve that, the deck bearings should be replaced with pin/rocker and slider type (roller/slider pot) bearings as shown in Figure 4.15. The numerical analysis model was modified to represent the new bearing conditions for further analysis. Figure 4.16 shows the lateral displacement time history for the Kobe (1995) ground motion scaled to the site DBE level of the bent-2 cap beam at span 2, and span 3 after the bearing was replaced. The relative displacement between the bent cap beam and deck span is reduced significantly and the lateral seismic load on the deck is being transferred to the bent effectively.

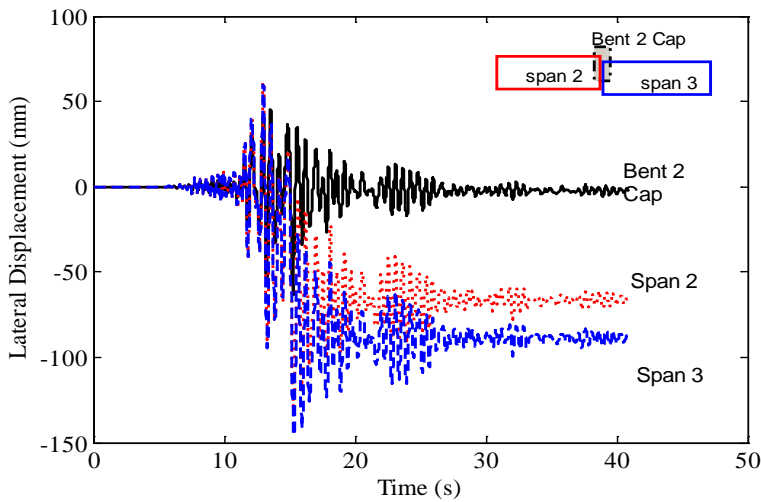


Figure 4.13 Comparison of lateral displacement of cap beam of Bent 2; span 2 and span 3 supported on Bent 2 of as-built bridge.

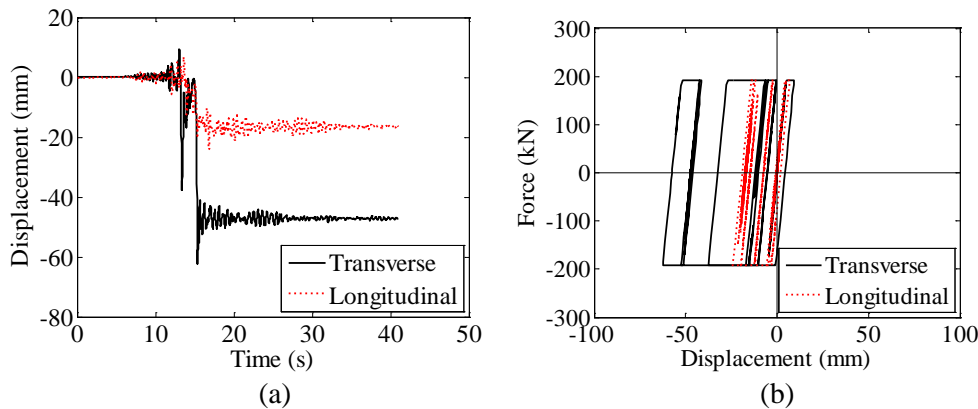


Figure 4.14 Bearing at bent 2: (a) deformation time history; (b) hysteresis.

Non-linear dynamic analyses were performed to assess the performance of the existing and retrofitted bridge bent under historic ground motions. The objective was to investigate the nonlinear dynamic response of the bridge bent and compare the displacement demand levels with the predicted capacity. The model for dynamic analysis was the same as the model used in the validation study except that the deck weight was doubled (3849 kN) to account for the tributary weight of two spans supported on each bent. A stiffness-proportional 5% constant structural damping was used in the analysis for all ground motions. The fundamental period of vibration of the as-built bridge bent was 0.39 s whereas the period of the retrofitted bridge was 0.33 s. The additional stiffness provided by the BRBs and SCEDs was identical since they were designed following the same procedure.

4.7 Effect of Ground Motion Incidence Angle on Bridge Performance

Seismic demands applied to bridge structures depend on ground motion type and direction. Penzien and Watabe (1975) determined that the major principal axis of a ground motion points to the epicenter in general, which is normal to the fault. Principal directions are often used because they have zero covariance with respect to each other. Bisadi and Head (2011) performed a parametric study with 100 paired ground motions, 100 different bridge configurations, and ground motion incidence angles varying from 0° to 180° with increments of 10° . The results showed that the critical angle of incidence causing

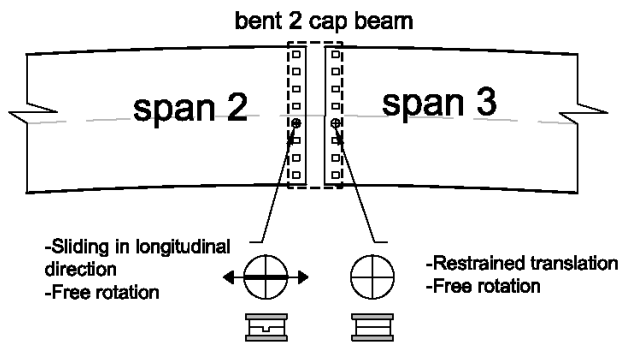


Figure 4.15 Bearing replacement plan for the bridge.

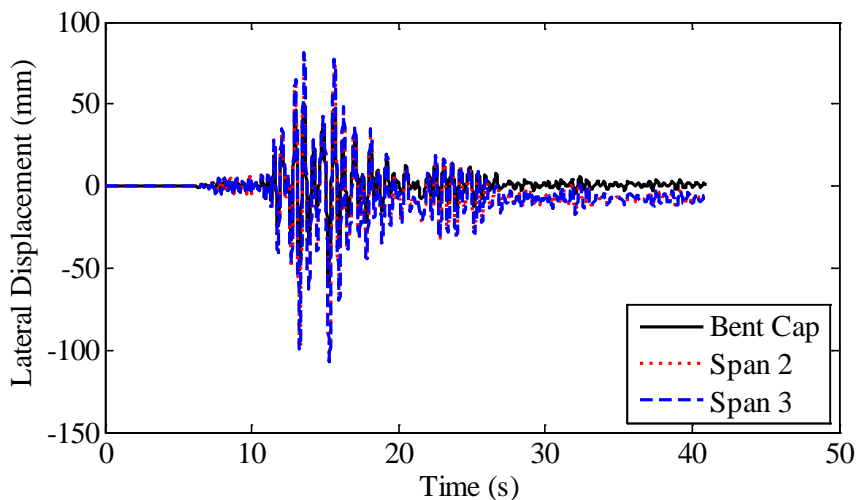


Figure 4.16 Comparison of lateral displacement of cap beam of bent 2; span 2 and span 3 supported on bent 2 for bridge after bearing replacement.

maximum response depends on the ground motion characteristics in addition to the bridge properties. Basu and Shinozuka (2011) analyzed the effect of seismic ground motion incidence angle on the seismic performance of straight bridges, concluding that straight bridges were most sensitive to ground motions with incident angles was between 30° and 60° with respect to the longitudinal axis of the bridge.

The effect of ground motion incidence angle on the three-span curved bridge was investigated. To reduce the influence of epicenter uncertainty and record-to-record (RTR) variability, the ground motions are first rotated to minimize the correlation in the orthogonal directions. Similar to the method described in ASCE 41-06 (2006), each set of rotated response spectra was scaled in such a way that the average of the square root of the sum of the squares (SRSS) spectrum in the interval $0.2T_{1,T} \approx 0.07s$ to $1.5T_{1,L} \approx 0.55s$ was equal to 1.3 times the average spectral acceleration (Sa) of the MCE spectrum in this interval ($1.3S_{avg} = 1.933 g$). After the ground motions were scaled, each set was used as input to the curved bridge with different incidence angles. The component with the smaller Peak Ground Acceleration (PGA) is applied first in the longitudinal direction of the bridge; the component with the larger PGA is applied in the orthogonal direction. The orthogonal Ground Motion (GM) sets are rotated counterclockwise from 0° to 180° as shown in Figure 4.17. Eleven far-field bidirectional scaled ground motions were rotated from 0° to 180° at an interval of 15° and seismic demands on the bridge were compared. A high number of ground motions are required to lower the dispersion in the response estimation using median values.

Figure 4.18 shows the peak drift demand for bent 1 in the global-X direction for 13 GM incidence angles ($0^\circ, 15^\circ, 30^\circ, 45^\circ, 60^\circ, 75^\circ, 90^\circ, 105^\circ, 120^\circ, 135^\circ, 150^\circ, 165^\circ,$ and 180°). The peak drift demand on the bent was higher when the major component was aligned with the global-X axis, i.e. when angle θ was near 0° and 180° . Figs. 4.19 and 4.20 show the peak drift demand for bent 2 in the global-X (lateral) and global-Y (longitudinal) directions respectively. The 0° angle produces the maximum demand in the lateral direction while the 90° incidence angle creates minimum demands for bent 2 in the transverse direction, because under such conditions the major GM component is in the lateral direction while the minor GM component is in the longitudinal axis. Bent 2 had the maximum response in longitudinal direction for an earthquake incidence angle of 90° , which is along the bridge longitudinal axis, as shown in Figure 4.20. A similar trend can be seen in the total base shear demand of all columns of the three bents. Figs. 4.21 and 4.22 show the total base shear demand for individual records (vertical left axis), while the standard deviation of log results (β) for each incidence angle is shown with diamond marks (vertical right axis). The peak base shear demand in the global-X direction (bridge transverse direction) was found to be higher for ground motion incidence angles close to 0° and 180° , while the base shear demand in the global-Y direction (bridge longitudinal direction) was higher for incidence angles close to 90° . Figure 4.23 shows the peak pounding force on the middle girder at abutment A. The pounding force was low for incidence angles close to 0° and 180° , while it was maximum for an incidence angle of 90° , as expected.

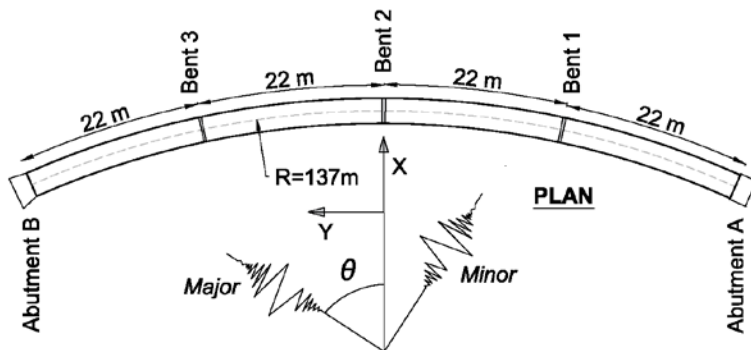


Figure 4.17 Rotation of ground motion components.

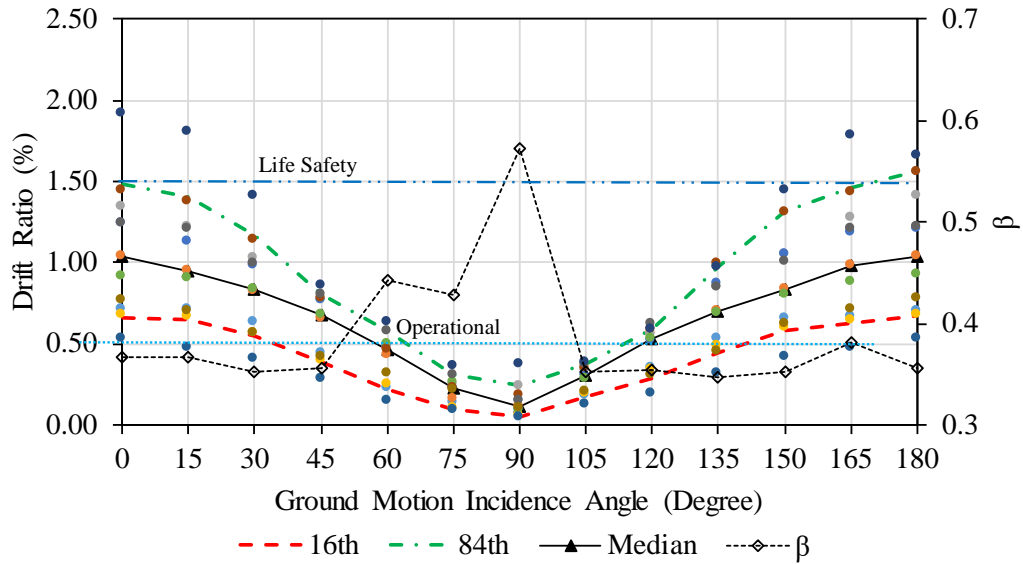


Figure 4.18 Drift ratio in global-X direction for bent 1.

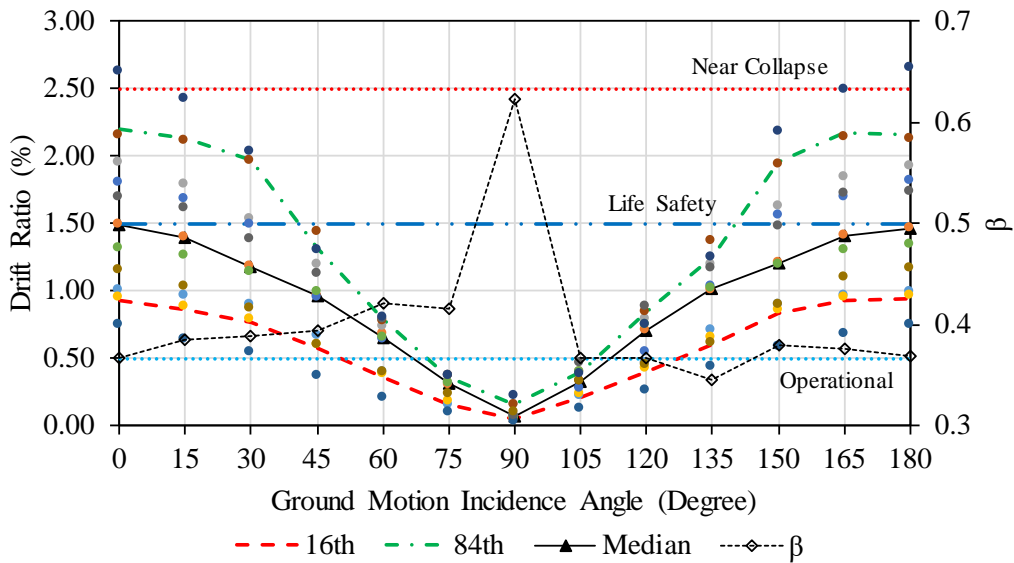


Figure 4.19 Drift ratio in global-X direction for bent 2.

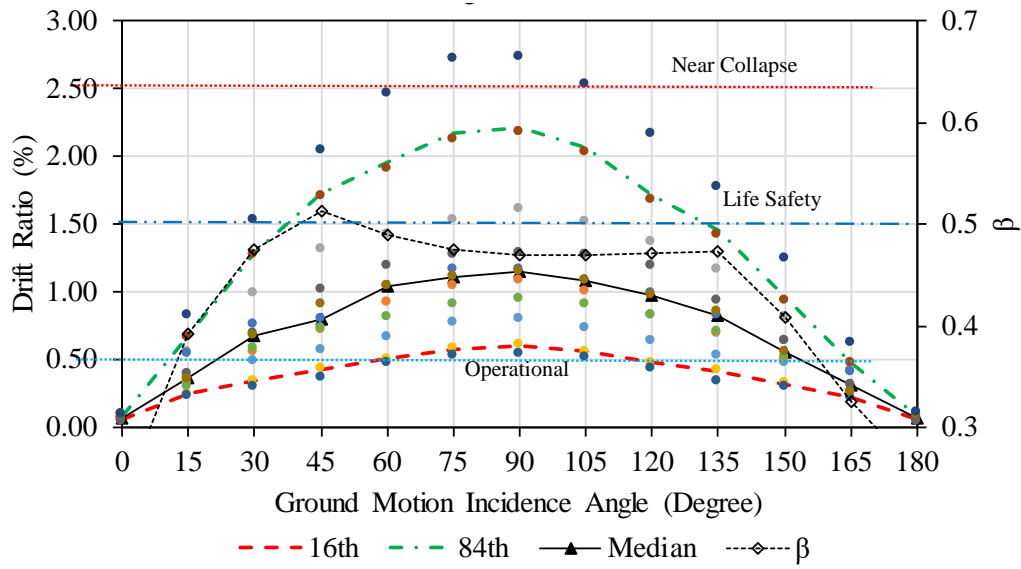


Figure 4.20 Drift ratio in global-Y direction for bent 2.

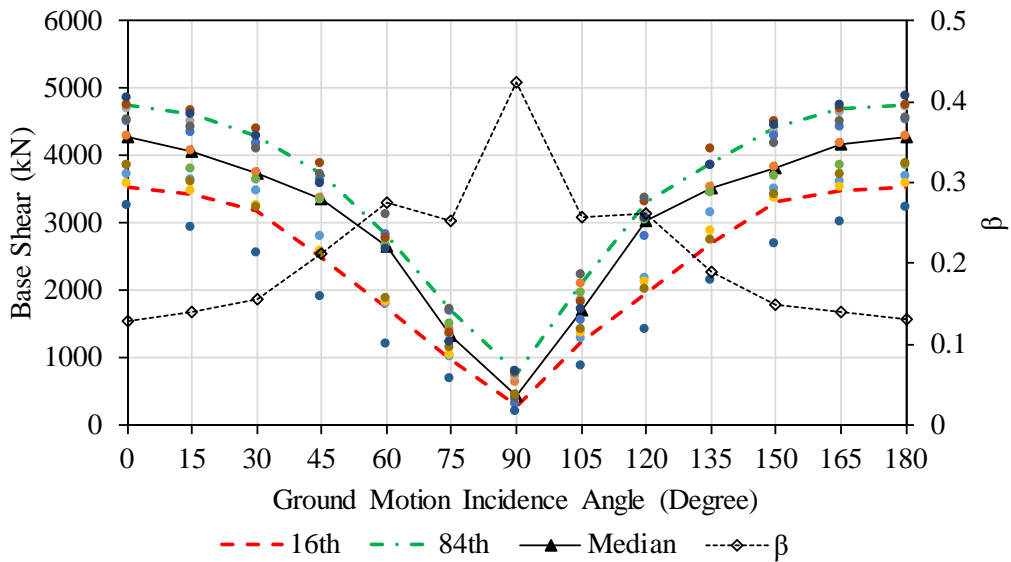


Figure 4.21 Total base shear of three bents in global-X direction.

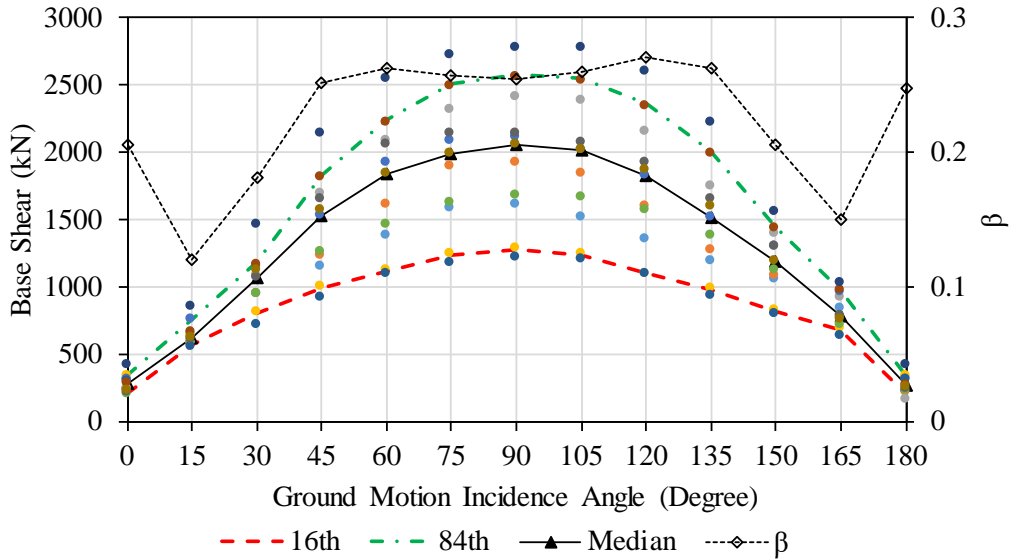


Figure 4.22 Total base shear of three bents in global-Y direction.

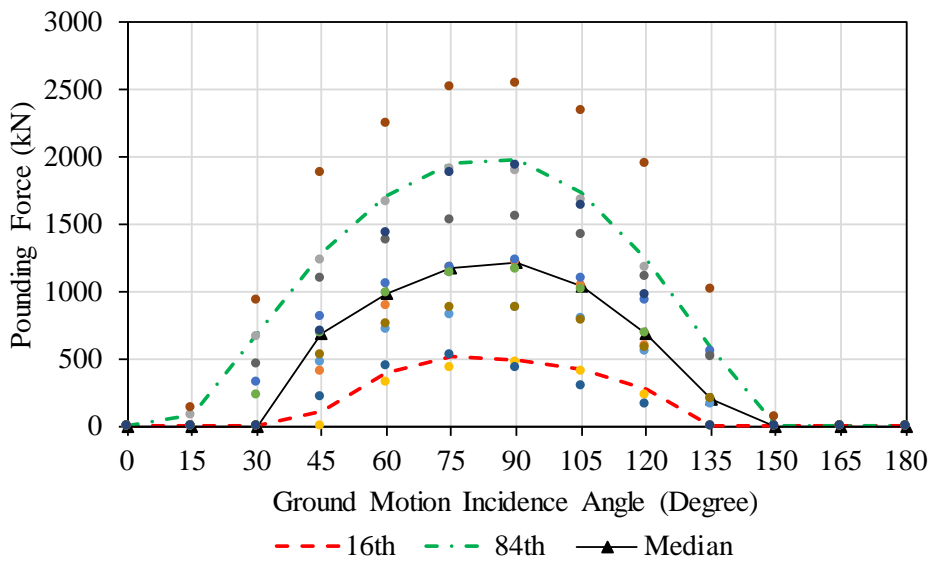


Figure 4.23 Pounding force on middle girder at abutment A.

4.8 Three-Dimensional Nonlinear Dynamic Analysis of Retrofitted Bridge with BRBs and SCEDs

The hysteretic response of the as-built bridge bent 2 under a near-field earthquake, the Chi-Chi Taiwan (1999) ground motion, scaled to the maximum credible earthquake (MCE) is shown in Figure 4.24. The peak drift demand of the as-built bridge bent was 2.1%, which is above the life-safety limit, but below the near-collapse limit. Figure 4.25 shows that the residual drift at the end of this earthquake was predicted as 0.15%. Structures may have large residual drifts when strong earthquakes cause crushing of the column core concrete. As predicted by pushover analysis, the core concrete remained undamaged until the bent reached a 2.7% drift ratio. Figure 4.26 shows the hysteretic response of the as-built bridge bent under the

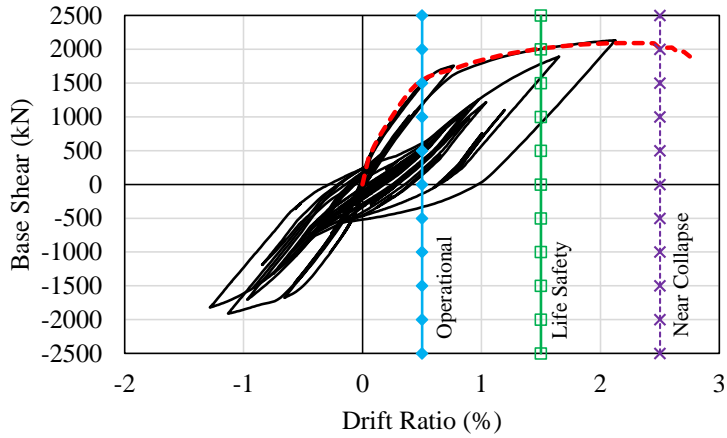


Figure 4.24 Performance of as-built bent 2 under Chi-Chi, Taiwan (1999) ground motion scaled to MCE.

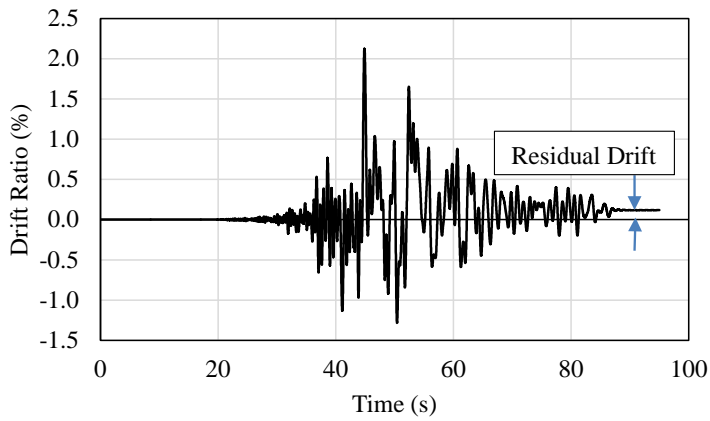


Figure 4.25 Drift ratio time history of as-built bent 2 under Chi-Chi, Taiwan (1999) ground motion scaled to MCE.

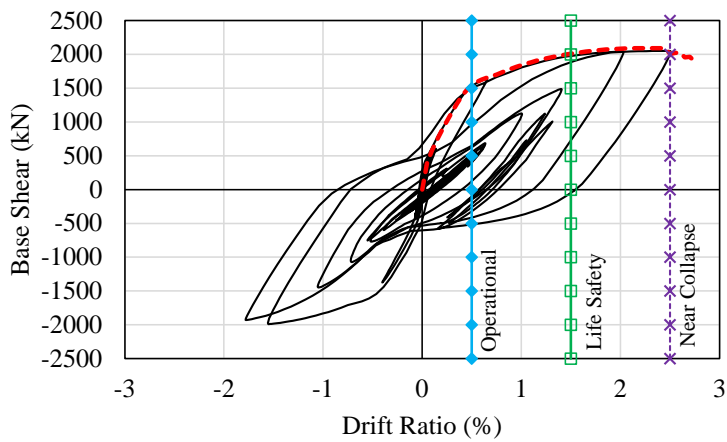


Figure 4.26 Performance of as-built bridge bent 2 under Imperial Valley (1979) Delta station far-field ground motion scaled to MCE.

far-field Imperial Valley (1979) earthquake ground motion recorded at Delta station. The as-built bent experienced a peak drift demand of 2.5% reaching the near collapse performance limit. Far-field earthquakes have several peaks in the ground acceleration time-history, with a high amount of input energy; thus, structures undergo several cycles of vibration, which might lead to low cycle fatigue and fracture of the steel reinforcement and increased spalling of core concrete.

The bridge was also analyzed after seismic retrofit with either BRB or SCED devices under the same earthquake ground motions; for the SCED devices the same retrofit scheme was used as in Figure 4.12. The performance of bent 2 after retrofit using two BRBs subjected to the Imperial Valley (1979), Delta station ground motion scaled to an MCE level is shown in Figure 4.27. The additional stiffness provided by the BRBs reduced the peak drift demand from 2.5% (as-built) to 1.65%, thus improving bent 2 performance from near collapse to life safety. The peak drift was reached at the peak of the input ground acceleration; with the exception of this strongest pulse, the BRBs reduced the drift demand significantly, as shown in Figure 4.27, which in turn would reduce low cycle fatigue damage to the steel reinforcement and concrete spalling in the columns of the bridge bent.

The bridge retrofitted with two SCEDs at each bent (Figure 4.12) was also analyzed under the Imperial Valley (1979) Delta station ground motion to compare its performance with the as-built structure. The hysteretic performance of the SCED-retrofitted bent is shown in Figure 4.28. The additional stiffness provided by the SCEDs reduced the peak drift demand of the bent from 2.5% (as-built) to 2.05% thus improving the performance from near collapse to life safety. Figure 4.29 shows a comparison of the performance of the as-built bent, the BRB retrofitted bent, and the SCED retrofitted bent under the Imperial Valley (1979) Delta station ground motion scaled to the MCE hazard level. The peak drift was reduced significantly and the structure shows a significant increase in stiffness after both retrofit schemes. The drift time history for the three cases is shown in Figure 4.30. The overall drift was reduced significantly by using BRBs or SCEDs.

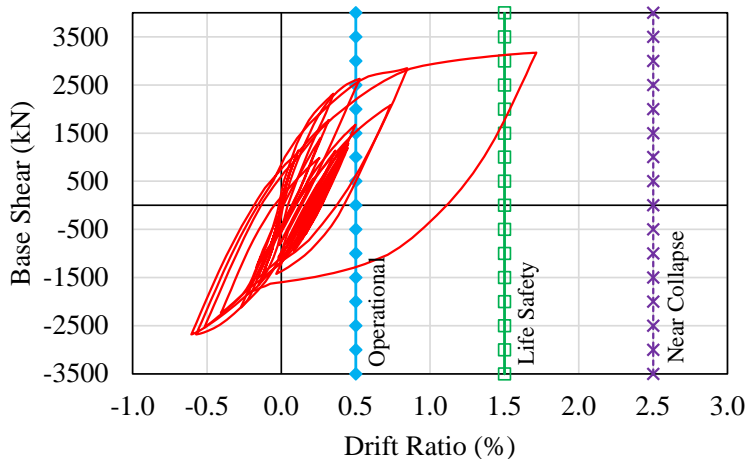


Figure 4.27 Performance of bridge bent 2 retrofitted with BRBs under Imperial Valley (1979) Delta station far-field ground motion scaled to MCE.

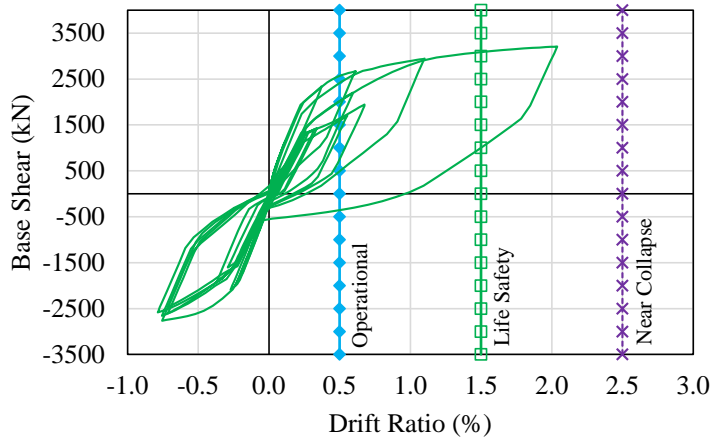


Figure 4.28 Performance of bridge bent 2 retrofitted with SCEDs under Imperial Valley (1979) Delta station far-field ground motion scaled to MCE.

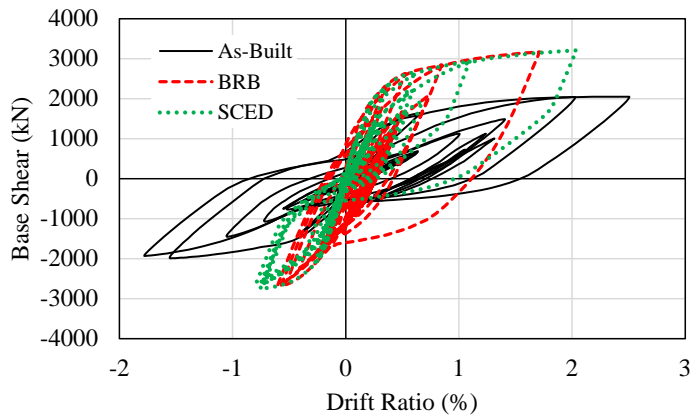


Figure 4.29 Comparison of performance of as-built and retrofitted bridge bent 2 under Imperial Valley (1979) Delta station far-field ground motion scaled to MCE.

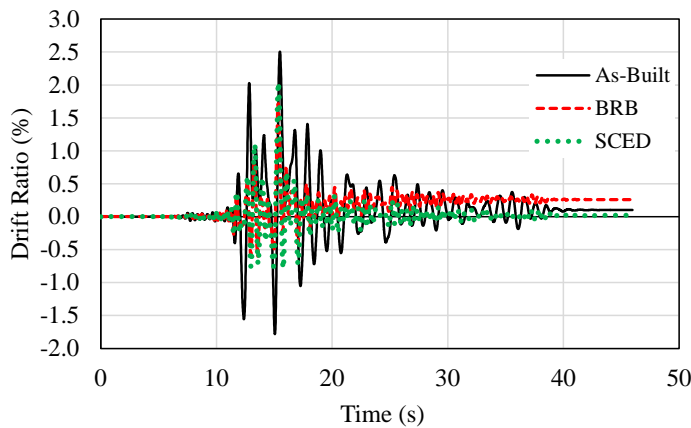


Figure 4.30 Drift ratio time history of as-built and retrofitted bridge bent 2 under Imperial Valley (1979) Delta station far-field ground motion scaled to MCE.

The SCED-retrofitted structure showed practically no residual drift at the end of the earthquake. Residual drift in the case of the BRB retrofit was larger than that of the as-built structure, but was still within the “operational” performance limit. This occurred because of yielding and permanent deformation of the BRB steel core after a number of load cycles during the earthquake. Once the core achieves a significant amount of plastic deformation, it cannot restore the deformed steel to the original position; this leads to a large residual drift in the structure. If the BRBs are designed to keep the plastic deformation to low levels, then they will act more as external stiffeners rather than energy dissipating devices. For a BRB to act as an energy dissipating device it is expected that it will undergo large plastic deformations beyond the yield point. The component hysteresis curves for a BRB and a SCED are shown in Figure 4.31 and 4.32, respectively. The SCED has a self-centering hysteresis behavior as opposed to the BRB, which shows significant residual deformation. The BRBs and SCEDs induced additional shear demand at the column-brace connection as shown in Figure 4.33, making the columns vulnerable to shear failure. Using an FRP donut at the column-gusset plate connection is recommended in order to enhance the column shear capacity. The FRP donut retrofit for a bridge bent with BRB/SCED is shown in Figure 4.34.

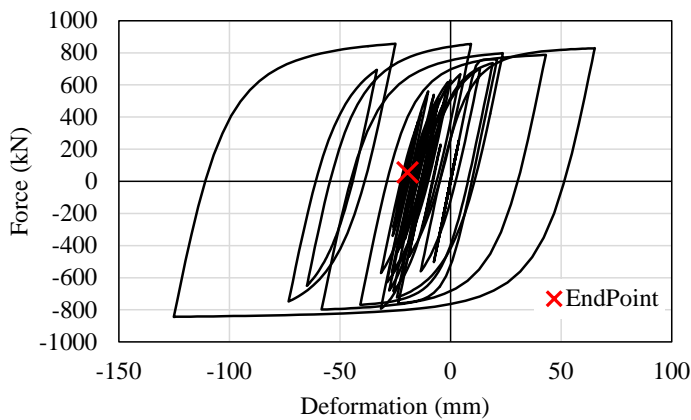


Figure 4.31 Hysteresis of one of the BRBs under the Imperial Valley (1979) Delta station far-field ground motion scaled to MCE.

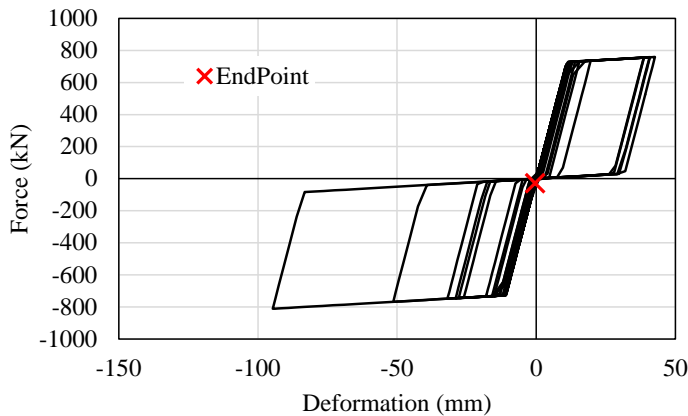


Figure 4.32 Hysteresis of one of the SCEDs under the Imperial Valley (1979) Delta station far-field ground motion scaled to MCE.

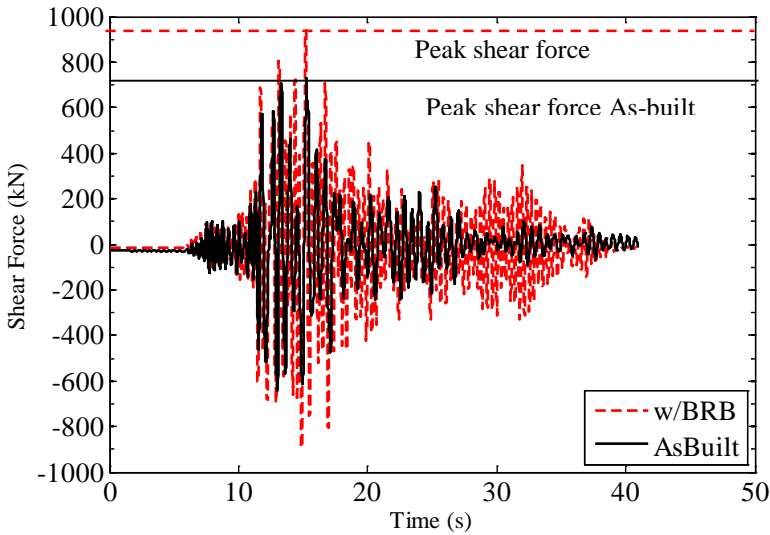


Figure 4.33 Shear force demand in the column at the column-brace connection for Imperial Valley (1979) Delta station far-field ground motion scaled to MCE.

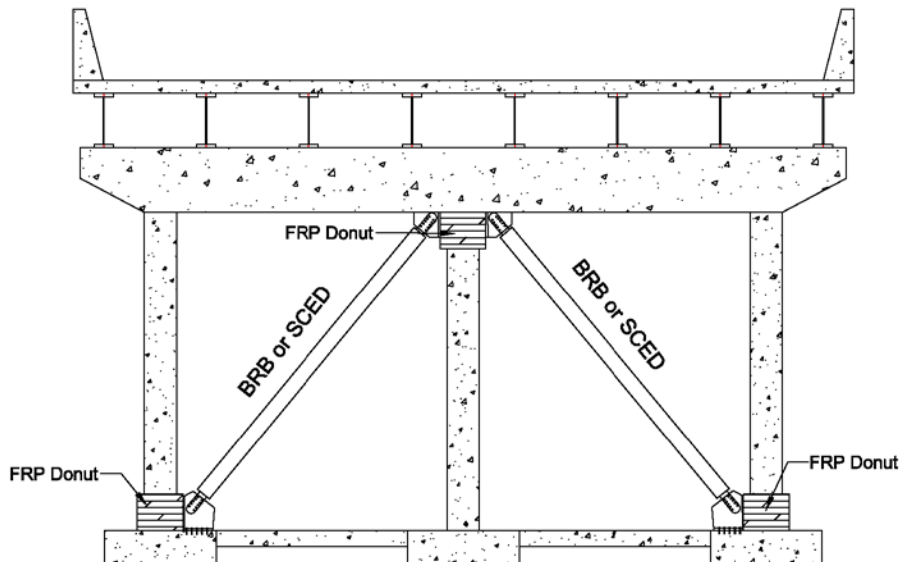


Figure 4.34 Column shear capacity enhancement with FRP donut.

Probabilistic seismic demand analysis was conducted for the as-built and retrofitted bridge bents using 22 far-field earthquake ground motions scaled to the MCE hazard level. The peak drift for each ground motion was used to evaluate probability of the bent achieving a certain performance limit based on the recommended values in Table 4.2. Figure 4.35 shows the Cumulative Distribution Functions (CDF) for the three cases. The as-built bent had a 50% cumulative probability of exceeding the “life safety” limit and a 9% cumulative probability of exceeding the “near collapse” limit state. The BRB retrofit reduced the probability of exceeding the “life safety” limit state to 9% while the SCED retrofit reduced it to 13%. The peak drift ratio demand for the SCED retrofit was found to be higher than that with the BRB retrofit,

as discussed previously. Both retrofit methods improved the seismic performance of the bridge bents significantly and the peak drift demand never reached the collapse limit state.

The CDFs for concrete compressive strain and steel bar tensile strain for the as-built and retrofitted bridge are shown in Figs. 4.36 and 4.37. With respect to concrete strain, the cumulative probability of exceeding the “operational” performance limit state reduced from 36% to 13% for the BRB retrofit and 18% for the SCED retrofit. According to Table 4.2, the “life safety” limit state occurs when the concrete compressive strain reaches 0.018. However, the peak strain in the column core concrete, or “crushing limit,” was 0.007 because of lack of confinement. The seismic retrofit reduced the cumulative probability of exceedance of the crushing limit from 9% to 0%. As shown in Figure 4.37, the effect of the retrofit was higher in controlling rebar tensile strain at the column bottom as compared to concrete strain. For the as-built bridge the cumulative probability for rebar strain exceeding the “operational” limit state of 0.015 was 65% which was reduced to 10% for the BRB retrofit and 18% for the SCED retrofit. It is clear that the seismic retrofit scheme improved bridge performance significantly.

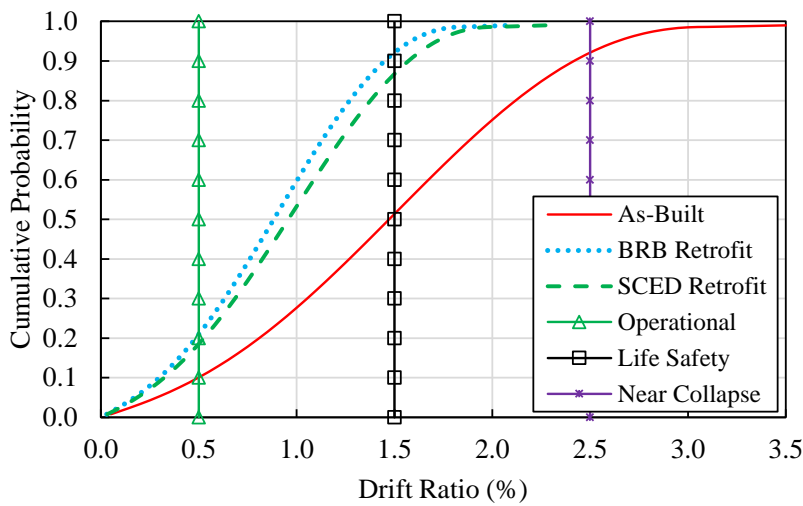


Figure 4.35 Drift performance evaluation of as-built and retrofitted bridge under 22 far-field ground motions scaled to MCE level.

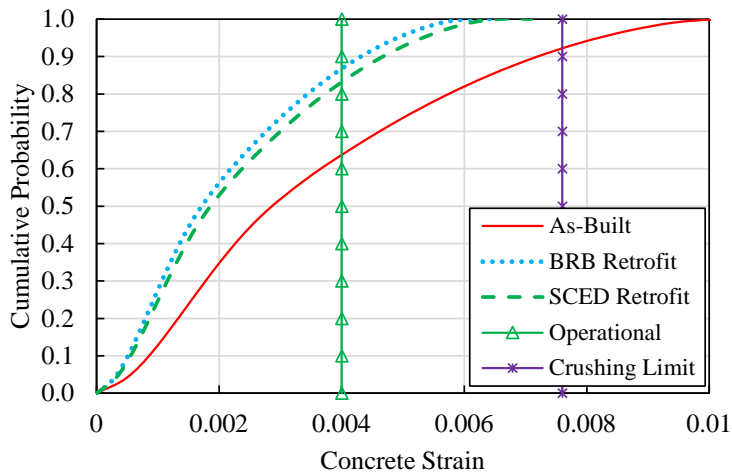


Figure 4.36 Concrete compressive strain performance evaluation of as-built and retrofitted bridge bent under 22 far-field ground motions scaled to MCE level.

Longitudinal BRBs/SCEDs reduced or eliminated pounding between the deck and abutment. Figure 4.38 shows the peak total pounding force at the abutment for 22 ground motions for the as-built and retrofitted bridges. The total pounding force was calculated as the sum of pounding forces at girders 1, 2 and 3. The pounding force varied from zero to 15000 kN for the as-built bridge. The as-built bridge experienced pounding at the abutment for 12 ground motions out of 22 input ground motions. The retrofitted bridge experienced pounding only for two input ground motions. The BRBs or SCEDs installed in the longitudinal direction provided additional stiffness and damping at the expansion joint restraining relative movement of the deck spans; the retrofit reduced the number of pounding incidences significantly in a given earthquake when pounding did occur, further reducing damage to the abutment or the deck, as shown in Figure 4.39.

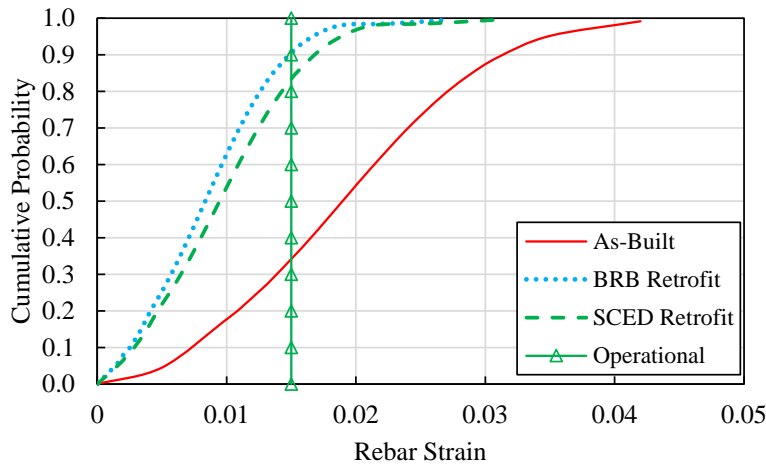


Figure 4.37 Rebar tensile strain performance evaluation of as-built and retrofitted bridge bent under 22 far-field ground motions scaled to MCE level.

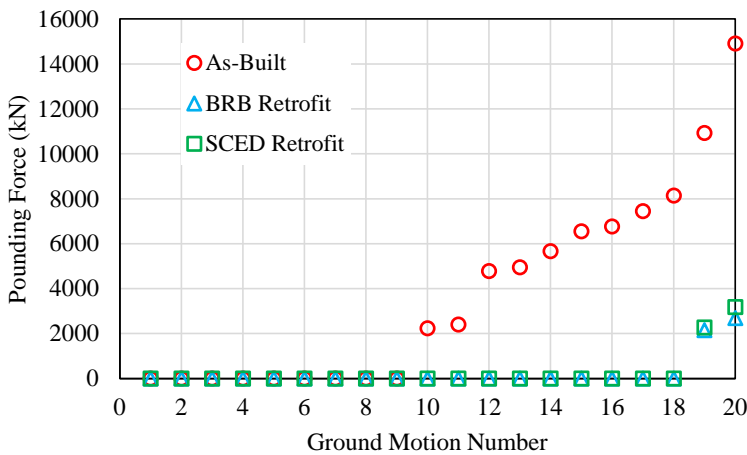


Figure 4.38 Pounding force between deck and abutment A for the as-built and retrofitted bridge under 22 far-field ground motions scaled to MCE level.

Figure 4.40 shows contribution of the columns of the three bents to the total lateral base shear demand of the bridge. For the retrofitted bridge, the BRBs and SCEDs absorbed 50% of the seismic shear demand (as per the design of BRBs/SCEDs for lateral seismic retrofit described in Section 5), reducing the shear demand in the columns; this reduced demand is at a section above the gusset plate joint. However, at the gusset plate-column connection, the BRBs and SCEDs induced additional shear demand making the columns vulnerable to shear failure. Using an FRP donut at the column-gusset plate connection, as was shown in Figure 4.34, is recommended to enhance column shear capacity at the gusset plate connection.

The benefit of using SCEDs over BRBs for seismic retrofit is returning the structure close to its original position after a seismic event. Residual drift ratio, a permanent drift ratio of the bridge bent due to concrete damage and permanent elongation of steel rebar, is a measure of the operational limit state. Figure 4.41 shows the residual drift CDF for bent 2 of the as-built bridge, the bridge retrofitted with BRBs and

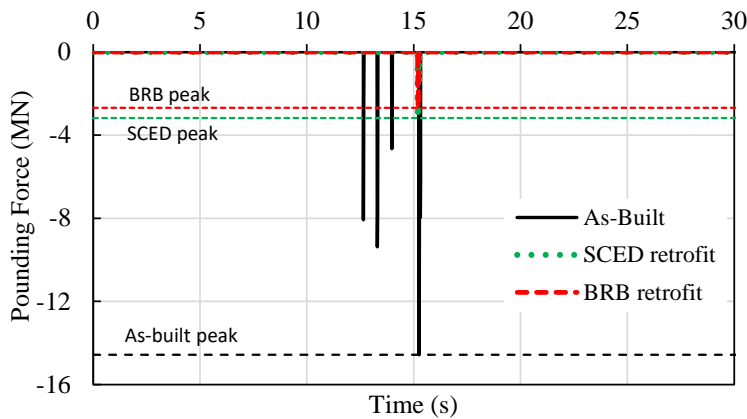


Figure 4.39 Pounding force time-history at abutment A for the as-built and retrofitted bridge under Kobe (1995) ground motion scaled to MCE level.

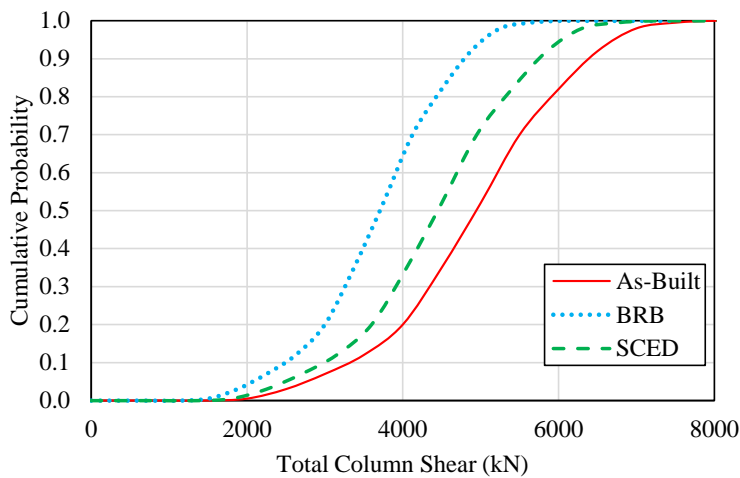


Figure 4.40 Total base shear resisted by columns of three bents in global-X direction under 22 far-field ground motions scaled to MCE level.

the bridge retrofitted with SCEDs. For as-built bridge bent 2, the cumulative probability was 60%, which means that the residual drift ratio exceeded 0.5%—the limit for “operational state” defined in Vision 2000. The cumulative probability of residual drift ratio exceeding 0.5% reduced to 18% for the bridge retrofitted with BRBs, while it was 0% for the bridge retrofitted with SCEDs. Self-centering energy dissipation devices successfully brought bent 2 close to the original center position, which kept the bridge within the operational performance level for all 22 ground far-field motions.

4.9 Performance of Bridge Retrofitted with BRBs/SCEDs and CFRP Donut

Since BRBs and SCEDs induce additional shear force in the columns at the column-brace connection, the bridge was analyzed with a seismic retrofit scheme with BRBs/SCEDs and CFRP donuts, as shown in Figure 4.34. The numerical model presented in Section 3 was implemented in the columns of the retrofitted bridge. The design of the CFRP donut for the columns of the bridge is presented in Section 5. The stiffness of the CFRP donut section was much higher than that of the column, thus making the effective length of the column shorter and increasing the stiffness of the structure. The brace is connected through the gusset plate which transfers the axial force to the CFRP donut. The base shear capacity of the bridge when retrofitted with BRBs/SCEDs and CFRP donut is higher than the bridge retrofitted with BRBs/SCEDs only. The peak drift demand for the bridge retrofitted with BRBs/SCEDs and donuts was lower than the bridge retrofitted with BRBs/SCEDs only as shown in Figure 4.42. The strain demand in the columns of bent 2 was recorded at the column section right above the CFRP donut. The peak concrete strain demand in the column of the bridge retrofitted with BRBs/SCEDs and CFRP donuts was lower than that of the bridge retrofitted with BRBs/SCEDs only. The additional strength provided by the CFRP donut reduced the peak concrete strain demand to 0.0006 from 0.0008 as shown in Figure 4.43(a). The peak rebar strain demand (Figure 4.43(a)) was also reduced in the bridge retrofitted with BRBs and CFRP donuts to 0.0050 from 0.0078 in the case of the BRB only retrofit. Since the columns retrofitted with CFRP donut provided additional stiffness, the energy dissipation demand in the BRBs was reduced. Cumulative energy dissipated by one of the BRBs at bent 2 for the two retrofit cases is shown in Figure 4.44(a) and (b). The BRB peak deformation was 26 mm for the bent retrofitted with CFRP donut as compared to 39 mm for bent with BRBs only. The cumulative energy dissipated by the BRBs reduced by 30% when the bent was retrofitted with additional CFRP donuts.

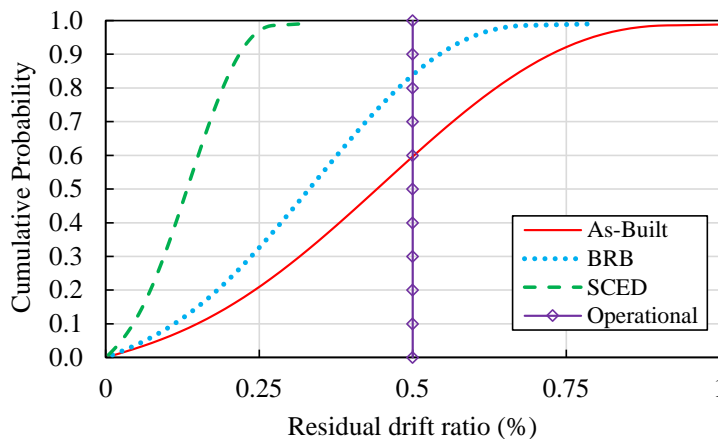


Figure 4.41 Residual drift CDF of as-built and retrofitted bridge bent 2 under 22 far-field ground motions scaled to MCE level.

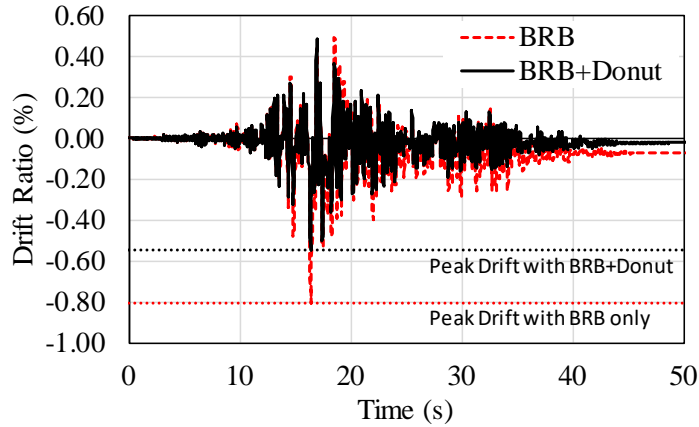


Figure 4.42 Comparison of drift for bent 2 of bridge retrofitted with BRBs and BRBs+Donut for Landers, Yermo fire station ground motion scaled to MCE level.

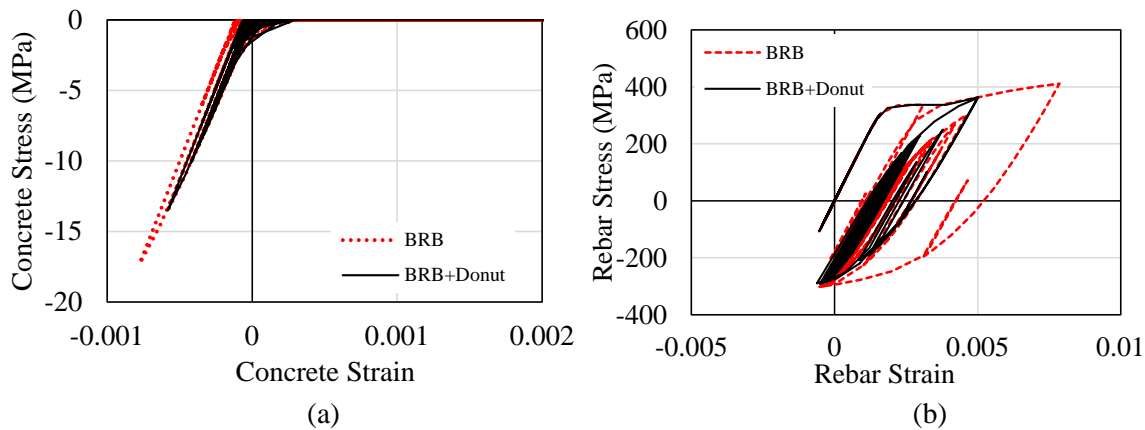


Figure 4.43 Stress-strain performance of: (a) column core concrete; (b) rebar of bent 2 of the bridge retrofitted with BRBs and BRBs+Donut for Landers, Yermo fire station ground motion scaled to MCE level.

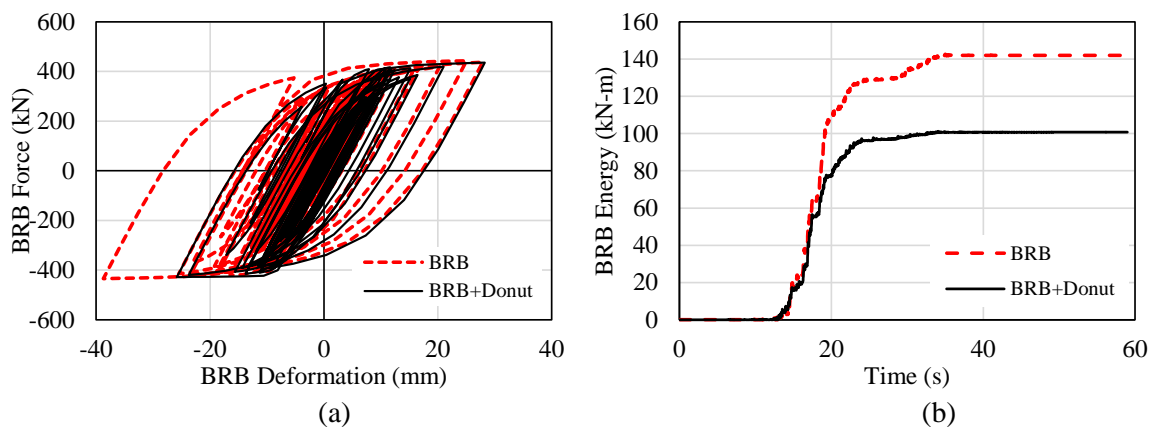


Figure 4.44 Performance comparison of BRB at bent 2 of the bridge retrofitted with BRBs and BRBs+Donut for Landers, Yermo fire station ground motion scaled to MCE level: (a) hysteretic curves; (b) cumulative energy dissipated by the BRB.

5. RECOMMENDED SEISMIC RETROFIT PROCEDURE USING BUCKLING RESTRAINED BRACES, SELF-CENTERING ENERGY DISSIPATION DEVICES AND CFRP DONUTS

5.1 Design of BRBs for Bridge Bents

The procedure in the American Institute of Steel Construction (AISC, 2014) manual provides a design for BRBs for new buildings. However, there is no such design guide for implementing BRBs in multi-column bridge bents. El-Bahey and Bruneau (2011) provided a detailed procedure of designing BRBs with a structural fuse concept; this design methodology aims to reduce the yield displacement of the system to achieve higher energy dissipation and ductility. Damage is relocated to the replaceable BRBs, while the main bridge bent remains elastic for the design level earthquake. The design procedure was further verified by Bazaez and Dusicka (2016) with cyclic tests on a scaled two-column bridge bent. Wang et al. (2016) performed a parametric study on the BRB strength contribution to the total base shear demand in a three-column bridge bent using an numerical model to optimize the BRB core area; the study showed that BRBs with “yield length ratio” (ratio of BRB core length to total workpoint length of the brace) equal to 0.55 perform best when designed for a 50% base shear contribution for the design level earthquake. The design procedure provided in this report follows the recommendations made by Wang et al. (2016). The steps for design of the BRBs for seismic retrofit are as follows:

1. Based on the seismic zone, soil site class, and site location, the design spectral acceleration ($S_{a,DBE}$) is obtained from the USGS design map tool, available at the website. (<https://earthquake.usgs.gov/designmaps/us/application.php>).
2. Response modification factor (R) and overstrength factor (\emptyset) are determined for design, based on AASHTO (2012) guidelines. The example bridge is located in Seismic Zone 3, and it is classified as a multiple-column bent bridge for Operational Category (AASHTO, 2012). This classification is associated with a response modification factor $R=5.0$, and an overstrength factor $\emptyset=1.3$.
3. Total seismic weight (W) and transverse stiffness of bent (K_{bentT}) are found using equations. Using the seismic weight and stiffness, the fundamental period of transverse vibration, T_{1_bent} , of the bent is calculated. This could also be performed using elastic structural analysis.
4. The elastic seismic coefficient (C_{sm}) corresponding to T_1 is found using 5% damped AASHTO design response spectra maps. The equivalent static seismic load (P_e) can be calculated using the deck seismic weight, fundamental mode of vibration, and design spectral acceleration using:

$$P_e = \frac{\emptyset C_{sm} W}{R} \quad (5.1)$$

where \emptyset = overstrength bridge factor for the seismic zone (AASHTO 3.10.9.4.3C); R = Response Modification Factor for bridge substructure (AASHTO Table 3.10.7.1-1).

5. It is design recommended that the BRB contribution to shear should be 50% of the total design seismic shear (Wang et al. 2016). Hence, the force resisted by each of the two BRBs (Figure 5.1) can be calculated as:

$$P_{BRB} = \frac{P_e}{N_{BRB} \cos\theta} \quad (5.2)$$

where N_{BRB} = Number of BRBs in the bent.

6. Strength adjustment factors (β and ω) and yield stress (F_y) for the BRBs are provided by the manufacturer; β is the compression overstrength factor and ω is the strain-hardening factor for the buckling restrained braces. The BRB core area A_c is calculated as:

$$A_{core} = \frac{P_{BRB}}{F_y \beta \omega} \quad (5.3)$$

The ratio of yielding core to work point length of the brace ($L_{core}/L_{workpoint}$) is recommended as 0.55.

- Installing BRBs in the bridge bent will increase stiffness. The new stiffness of the retrofitted bent can be calculated as:

$$K_{bentR} = K_{bent} + N_{BRB} * K_{BRB} * \cos^2 \theta \quad (5.4)$$

- Using the new period (T_1) for the retrofitted bridge bent, the new seismic design force is estimated and steps from 4 to 8 are repeated until the BRB core area stops changing.

5.2 Design of SCED for Bridge

Self-centering energy dissipation devices are a new development and there have not been any prescribed guidelines for design. From Section 4.2, it is known that SCEDs have an activation point. This design procedure uses the self-centering energy dissipation device tested by Christopoulos (2008). The steps to design the SCEDs for retrofit are as follows:

- Based on the seismic zone, soil site class, and site location, the design spectral acceleration ($S_{a,DBE}$) is obtained from the USGS design map tool, available at the website. (<https://earthquake.usgs.gov/designmaps/us/application.php>).
- The response modification factor (R) and overstrength factor (ϕ) is found for the design, based on AASHTO (2012) guidelines. The example bridge is located in Seismic Zone 3, and it is classified as a multiple-column bent bridge for Operational Category (AASHTO, 2012). This classification is associated with a response modification factor $R=5.0$, and an overstrength factor $\phi=1.3$.
- The total seismic weight (W) and transverse stiffness of the bent (K_{bentT}) are found using equations. Using the seismic weight and stiffness, the fundamental period of transverse vibration, T_{1_bent} , of the bent is calculated. This can also be performed using elastic structural analysis.
- The elastic seismic coefficient (C_{SM}) corresponding to T_1 using 5% damped AASHTO design response spectrum maps is calculated. The equivalent static seismic load (P_e) can be obtained using the seismic weight of the deck, the fundamental mode of vibration, and the design spectral acceleration using Eq. (5.1).
- This design procedure recommends that SCEDs contribute 50% of the total design seismic shear. Hence, the force resisted by each of the two SCEDs (Figure 5.1) can be calculated as:

$$P_{act} = \frac{P_e}{N_{SCED} \cos \theta} \quad (5.5)$$

where N_{SCED} = Number of SCEDs in the bent.

- The ratio of forward activation force to reverse activation force (β) is taken as 1.0, as shown in Figure 5.2. The area of PT bars and friction force can be calculated as follows:

$$F_a = P_{pt} + F = P_{act} \quad (5.6)$$

$$P_{pt} + F = 2F \Rightarrow P_{pt} = F = 0.5 * P_{act} \quad (5.7)$$

where, P_{pt} is the pretension in the high strength PT rods and F is the friction damper force. Using these two quantities, the PT area and the properties of the friction damper can be designed. The level of prestress in the PT bars is recommended to stay below 70% of the yield stress. The initial stiffness (K_1) is

provided by a combination of PT bars, inner and outer tubes and the friction damper. Secondary stiffness is provided by PT bars only.

5.3 Design of CFRP Donut for Column Shear

A seismic repair method using a CFRP donut consisting of a CFRP cylindrical shell, non-shrink repair concrete, and headed steel bars has been developed; the method had been implemented for severely damaged precast and cast-in-place concrete column-to-footing/cap beam connections under quasi-static cyclic loads (Parks et al. 2016; Wu and Pantelides 2017a; b). The load and displacement capacity of the severely damaged specimens was successfully restored. Based on the good performance of the repaired columns, the repair method was implemented in the analysis of the multi-column bridge bents in this study.

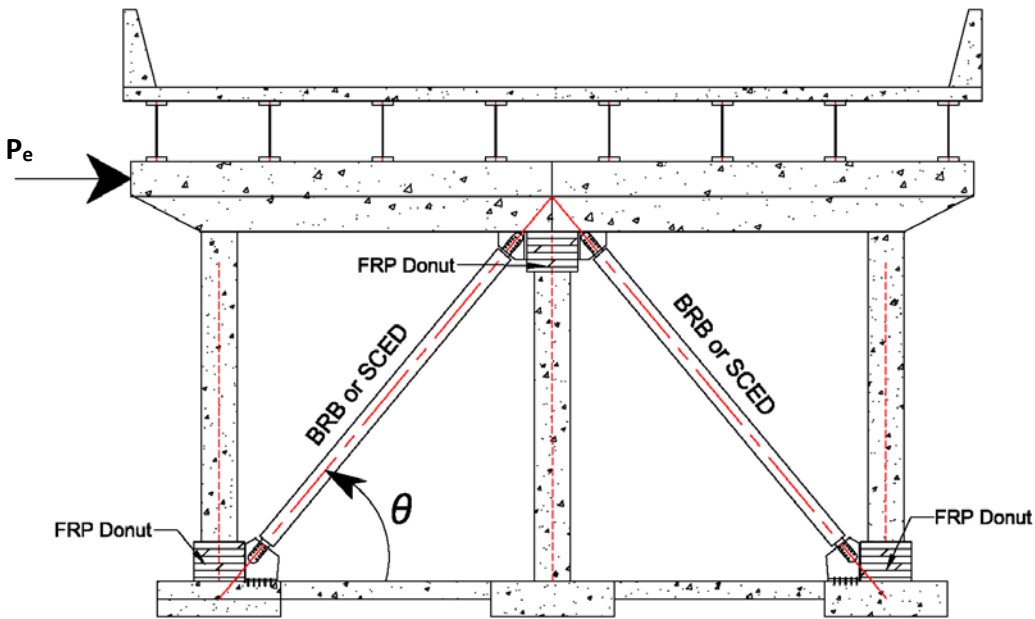


Figure 5.1 Retrofit scheme for old bridges.

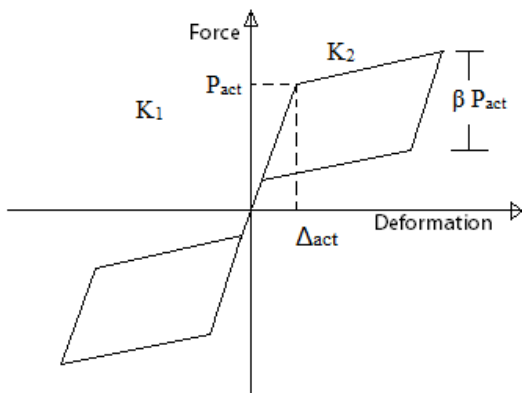


Figure 5.2 Design of self-centering material.

5.3.1 Strut-and-Tie Model for Retrofit Design

To predict the performance of the repaired precast concrete specimens, a Strut-and-Tie model (STM) was developed for the original and repaired specimens (American Concrete Institute Committee 318 2014; Brown et al. 2016). Generic modeling parameters were established and special attention was focused on the struts within the CFRP cylindrical shell. The response obtained from the STM showed satisfactory agreement with the experiments of the repaired bridge assemblies in terms of initial stiffness, lateral load and displacement capacity.

For the retrofit design using a CFRP donut, a simplified STM was developed in this research project, which is focused on the CFRP donut design, as shown in Figure 5.3. General parameters were developed in the simplified STM to determine the tension force for tie AD .

5.3.2 Design of Headed Steel Bars

The tension and compression force centroids at first yield, x_t and x_c respectively in Figure 5.3(a), were found from sectional analysis of the original column. The first yield state is defined by the onset of extreme tension steel yielding. The corresponding tension force, F_t , from the column longitudinal steel and the compression force, F_c , from the column concrete were determined by considering the applied axial load at the column top, as shown in Figure 5.3(a). Node C was located at the top fiber of the CFRP donut.

For the retrofitted column cross-section, design of the headed steel bars was based on achieving the same column flexural capacity as the original column. To be conservative, the contribution of the original longitudinal steel bars was ignored. In this retrofit, four 32 mm (#10) headed steel bars were used for each side of the column. In an actual seismic retrofit, a similar number of headed steel bars would have been used in the north and south sides of the column but since the present model is two-dimensional this was not implemented.

5.3.3 Determination of CFRP Donut Geometry

The retrofit height of the CFRP donut, H_R , was assumed to be at least equal to the calculated plastic hinge length of the column, obtained as (Panagiotakos and Fardis 2001):

$$L_{pl,cy} = 0.12L_s + 0.014a_s d_b f_y \quad (5.8)$$

$$L_{pl,mon} = 1.5 L_{pl,cy} \quad (5.9)$$

where L_s is the shear span, a_s equals 1.0 by considering steel bar bond-slip in the plastic hinge, d_b is the diameter of the longitudinal column steel bars, and f_y is the yield strength, in SI units. The plastic hinge region from Eq. (5.9) was calculated as 889 mm. A retrofit height of 1067 mm was selected based on experience from past experiments (Wu and Pantelides 2017a; b).

Shape modification of the original column cross-section by post-tensioning an FRP shell using expansive cement concrete was considered (Yan and Pantelides 2011). In this study, a circular shape was selected for the CFRP donut. Once the location, number and size of headed steel bars were determined, the diameter of the CFRP cylindrical shell, D_R , was determined by considering the necessary gap between CFRP shell and headed steel bars; hence a diameter D_R equal to 1372 mm was selected.

5.3.4 Design of CFRP Cylindrical Shell

Based on the CFRP donut dimensions, the layout of the simplified STM was finalized. The lateral load, F_L , was determined as the lateral shear capacity of the column and applied at node C in Figure 5.3(a). Based on equilibrium of the nodes in the statically determinate STM truss, the forces in all struts and ties were obtained using statics. The horizontal location of node E , x_E in Figure 5.3(a), was determined based on static equilibrium of nodes D and E . The diameter of the CFRP donut, D_R , could be increased due to the large lateral load, F_L , to accommodate the location of node E . The final iteration required a lateral load, F_L , equal to 1000 kN, which was the calculated column shear capacity, and a final CFRP shell diameter of 1372 mm was selected.

The material details of the CFRP composite and retrofitted concrete can be found in Table 3.1. The measured thickness of a single CFRP composite layer was 1.20 mm in laboratory experiments (Wu and Pantelides 2017a; b). The tension force of tie AD , T_{AD} in Figure 5.3(a), was used to determine the number of CFRP hoop layers based on ring theory, as shown in Figure 5.3(b). Based on previous experimental and simulation results, the top one-third of the CFRP shell forms an effective tension ring, which acts as a tension tie that provides continuous confinement to the repair concrete (Wu and Pantelides 2017a; b). The total thickness of the CFRP shell is calculated as:

$$t = \frac{0.5 T_{AD}}{E_f K_\varepsilon \varepsilon_{fu} h_e} \quad (5.10)$$

where t is the total thickness of the CFRP hoop layers, T_{AD} is the tension force in tie AD , E_f is the elastic modulus of the CFRP composite, K_ε is the FRP strain efficiency factor considering premature failure of the FRP composite due to three-dimensional stresses, assumed as 0.58 (American Concrete Institute Committee 440, 2017), ε_{fu} is the ultimate tensile strain of the CFRP composite, and h_e is the effective height of the CFRP shell, assumed equal to $H_R/3$. A minimum CFRP shell thickness was required to suppress strain-softening behavior in the FRP-confined concrete cross-section as (Moran and Pantelides 2012):

$$t_{min} = \frac{\lambda_{SH} f'_{CR}}{4 C_{SH} E_f} D_R \quad (5.11)$$

where t_{min} is the minimum thickness of CFRP hoop layers, f'_{CR} is the compressive strength of the repair concrete, and D_R is the diameter of the CFRP donut. The parameters of λ_{SH} and C_{SH} for the square column in this study are 12 and 1, respectively, (Moran and Pantelides 2012). Based on the calculated results from Eqs. (5.10) and (5.11), and the CFRP composite material properties from Table 3.1, five layers of CFRP composite were obtained for the hoop direction of the CFRP shell. Two layers of vertical CFRP composite were provided for the CFRP shell to avoid circumferential failure of the CFRP shell based on previous experimental results (Parks et al. 2016; Wu and Pantelides 2017a; b).

5.3.5 Design of Steel Collar

Considering the insufficient transverse confinement of the original cast-in-place column, bond-slip of longitudinal steel bars was expected (Harajli and Mabsout 2002); moreover the bond of the original column concrete and repair concrete is crucial for satisfactory performance (Wu and Pantelides 2017a; b). A steel collar with shear studs around the original column within the CFRP donut was provided to increase the bond between original cast-in-place column and retrofit concrete (Wu and Pantelides 2017b). The nominal shear strength of a single steel headed stud, Q_n , can be determined as (AISC Committee on Specifications 2010):

$$Q_n = 0.5 A_{sa} \sqrt{f'_{cR} E_c} \quad (5.12)$$

where A_{sa} is the cross-sectional area of a steel headed stud, equal to 507 mm² in the present case; f'_{cR} is the retrofit concrete compressive strength assumed as 50 MPa; and E_c is the modulus of elasticity of the non-shrink concrete, assumed as equal to 35 GPa; the design shear strength of a single steel stud was obtained as 337 kN. The shear force demand for steel studs is determined from bending moment equilibrium at the repair section as follows:

$$Q_D = M_D / b_c \quad (5.13)$$

where M_D is moment demand at the base of the column obtained from push-over analysis, equal to 2500 kN-m; and b_c is the width of the column section, equal to 914 mm. The calculated shear force for the shear studs was obtained as 2734 kN from Eq. (5.13); thus, the required minimum number of shear studs was slightly larger than eight. In this study, it was assumed that nine studs would be provided on each side. The final repair design with the steel collar is shown in Figure 5.4.

5.3.6 Design of CFRP Jackets Above the CFRP Donut

Considering the insufficient number and details of the steel transverse reinforcement provided in the joint regions, two layers of CFRP composite were provided at $\pm 45^\circ$ with respect to the horizontal at column-to-cap beam joints in previous seismic retrofit designs for joints (Gergely et al. 1998). In this study, the same design procedure was adopted to strengthen the column-cap beam joints.

To increase the shear capacity of column cross-sections immediately above the retrofitted region, CFRP jackets were designed outside the CFRP donut. The design CFRP jacket thickness is defined as (American Concrete Institute Committee 318, 2014; Seible et al. 1997):

$$V_f = V_0 / \phi_v - (V_c + V_s) \quad (5.14)$$

$$t_j = \frac{V_f}{0.5 \pi \varepsilon_{fj} E_f b_c} \quad (5.15)$$

where V_0 is the column shear demand obtained from push-over analysis, equal to 1200 kN; ϕ_v is the shear reduction factor equal to 0.85, V_c is the shear capacity of the concrete, V_s is the shear capacity of the transverse steel reinforcement, V_f is the column shear capacity of the CFRP composite, ε_{fj} is the effective strain of the CFRP jacket, assumed as 0.004 (Seible et al. 1997), and t_j is the thickness of the CFRP jacket. The calculated thickness of the CFRP jacket was 2.0 mm, and two layers of CFRP composite were designed for the column outside the CFRP donut. The detailed design of the retrofitted multi-column bridge bent is shown in Figure 5.5.

5.3.7 Foundation Seismic Rehabilitation

To achieve the seismic retrofit goal, it is necessary to develop a higher capacity than the existing foundation and pile cap system could provide. In this respect the seismic rehabilitation measures implemented in full scale in-situ tests carried out by Pantelides et al. (2007) were used. These included: (a) four 32-mm Dywidag bass epoxied into the piles of each of the three pile caps for a distance of 2.44 m; (b) a RC grade beam consisting of two 0.84 m x 0.46 m RC beams on the sides of the existing 0.46m square RC strut, along with a RC overlay 0.30 m x 2.13 m with two end beams at the edges of the exterior pile caps, as shown in Figure 5.5.

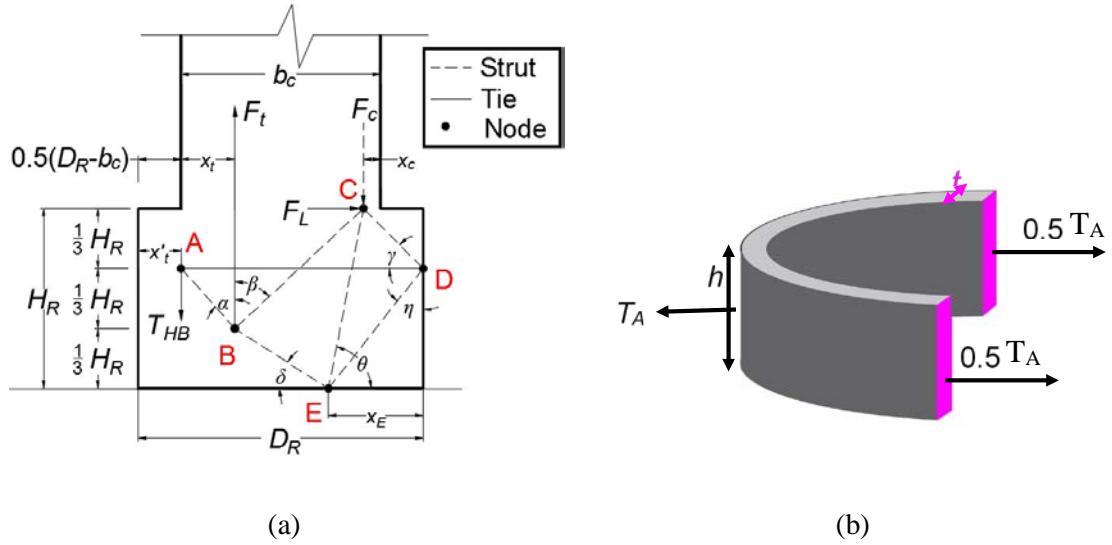


Figure 5.3 Design of CFRP donut: (a) Simplified Strut-and-Tie model; (b) design of hoop layers.

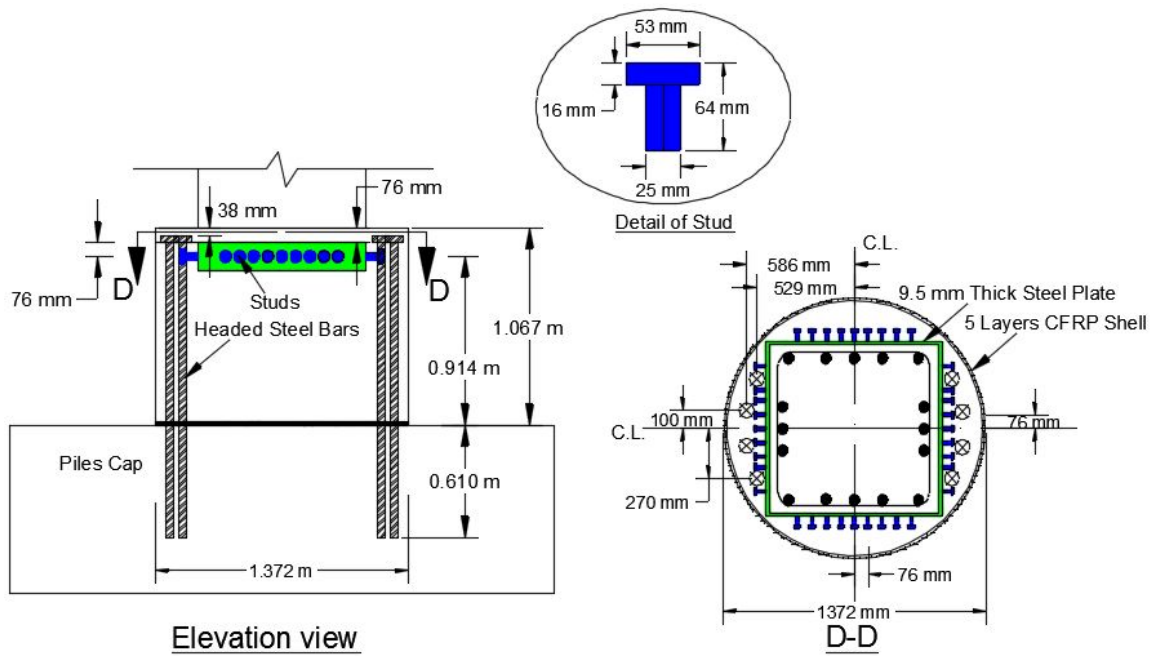


Figure 5.4 Retrofit details of CFRP donut for column.

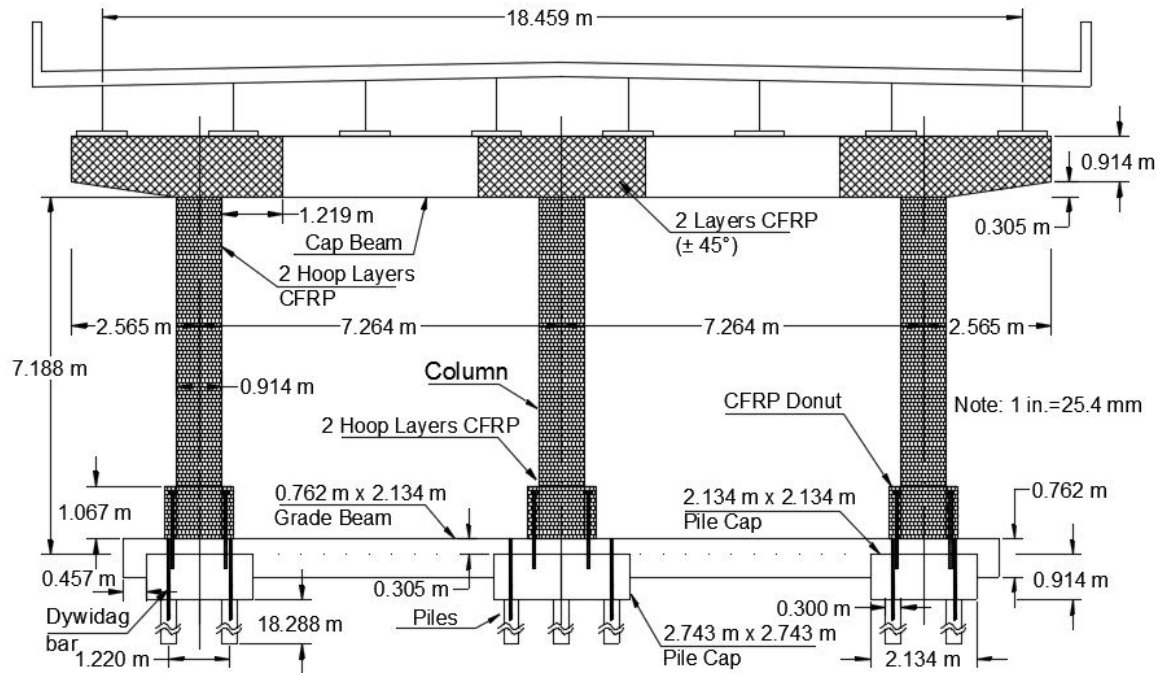


Figure 5.5 Retrofitted bridge bent with CFRP composite jackets and CFRP donut.

6. CONCLUSIONS

6.1 CFRP Donut for Bridge Column Repair

A method was developed for the seismic retrofit or repair of deficient cast-in-place monolithic bridge columns connected to a cap beam or footing. In half-scale experiments, the original specimens had experienced severe damage including concrete crushing and spalling in the concrete core, longitudinal steel bar buckling across multiple spiral hoops and longitudinal bar fracture. Experiments showed that the repair method restored strength and displacement capacity successfully despite the severe damage. The ultimate drift ratio of the repaired specimens was 8.1 and 8.4%; the strength of the repaired specimens was 20% higher than the original specimens. The displacement ductility obtained for the repaired specimens was 6.0 and 6.8, which exceeds the displacement ductility demand of 5.0 specified in the AASHTO Guide Specifications for single column bridge bents.

The CFRP cylindrical shell did not experience cracking or failure; it provided continuous confinement, resisted hoop tension, and improved the shear strength of the system. CFRP hoop layers formed an effective tension ring concentrated at the top 152 mm of the CFRP donut which was approximately the top one-third of the donut height. Vertical CFRP layers prevented formation of circumferential cracks in the CFRP cylindrical shell. Headed steel bars transferred axial forces from the column through the CFRP donut to the footing/cap beam and improved the stiffness of the repaired columns. Pinching was caused by concrete damage, which reduced available development length of the buckled and fractured bars suffered by the original specimens and the resulting slip between cracked surfaces. Bond between column concrete and CFRP donut concrete is crucial for satisfactory performance of the repair system; a steel collar with steel studs is recommended for enhancing the bond between column and repair concrete. Based on the results from the numerical simulations using the model developed in this research the following conclusions can be made:

1. Based on the overall performance of the repaired specimens, the repair technique was successful. It restored the strength and displacement capacity of severely damaged reinforced concrete columns with crushed concrete in the column core containing buckled and fractured steel bars. The repair technique requires minimal intervention and is relatively fast to construct and implement.
2. The numerical Model Fiber developed, considering distributed plasticity spread over a defined plastic hinge length reproduced hysteresis curves and energy dissipation curves that matched the experimental results in a satisfactory manner.
3. Model Fiber considered bond-slip effects, the effects of previous loading history, and cyclic degradation of column longitudinal steel bars.
4. The modified steel stress-strain curve, which was derived from a one-dimensional bond-slip model, was successful in Model Fiber for simulating the experimental response. The defined plastic hinge length was about 67% of the column cross-sectional dimension for the cast-in-place specimens.
5. Model Fiber considered low-cycle fatigue effects and demonstrated that the accumulated fatigue damage of the longitudinal steel bars was consistent with the experimental results. The model was able to obtain the accumulated fatigue of the steel bars and to predict steel bar fracture for the same drift ratio cycle as the experiment.
6. Model Fiber produced local responses such as moment-rotation relationships and could be used for prediction purposes.

6.2 Retrofit of Curved Bridge Using BRBs/SCEDs

The research presents a comprehensive evaluation on the use of BRBs and SCEDs to seismically retrofit existing curved RC bridges under 12 different incidence angles. BRBs or SCEDs were added to the bridge bents as structural fuses, creating a dual lateral force resisting system with larger strength and stiffness than that of the original bridge system in the transverse direction. The curved bridge was also retrofitted at the abutments with BRBs/SCEDs to prevent structural pounding between girders and abutments. The results show that BRBs/SCEDs can prevent damage to the main components of the original bridge by seismic energy dissipation through hysteretic behavior and by shear demand redistribution in the transverse direction. The main findings are as follows:

1. The curved bridge experienced maximum demand in the transverse direction when the earthquake major component was in a direction perpendicular to the bridge longitudinal axis. Structural pounding between decks and abutments was maximum when the major component of the ground motion aligned with the bridge longitudinal axis.
2. BRBs/SCEDs installed in the bridge bents reduced the drift ratio demand significantly. Peak drift ratio demand with the SCED retrofit was higher than that with the BRB retrofit. Since BRBs show isotropic hardening while SCEDs do not, BRBs resist larger forces as compared to SCEDs.
3. Dynamic analysis of the bridge for 22 far-field ground motions shows that the as-built bent had a 50% probability of exceeding the “life safety” performance limit and 9% probability of exceeding the “near collapse” performance limit for MCE level ground motions.
4. Both BRB and SCED seismic retrofits reduced the probability of exceeding the “near collapse” performance limit to 0%. Retrofit with BRBs reduced the probability of exceeding the “life safety” performance limit to 9%, while this probability was 13% for the SCED retrofit.
5. The probability of exceeding the crushing limit of column core concrete was 9% for the as-built bridge, which was reduced to 0% for both the BRB and SCED retrofit. Based on the concrete strain demand, the cumulative probability of exceeding the “operational” performance limit state reduced from 36% for the bents of the as-built bridge to 13% in the case of BRB retrofit and 18% for the SCED retrofit.
6. For the as-built bridge the cumulative probability for rebar strain exceeding the “operational” limit state was 65%, which was reduced to 10% for the BRB retrofit and 18% for the SCED retrofit.
7. Significant reduction of the residual drift ratio was observed for the bent retrofitted with SCEDs as compared to BRBs. For the as-built bridge, the probability of exceeding the “operational” limit state was 40%. This probability was reduced to 18% for the bridge retrofitted with BRBs and 0% for the bridge retrofitted with SCEDs. The self-centering energy dissipation devices successfully returned the bridge bent close to the original position which kept the bridge in the “operational” limit state for all 22 ground motions.
8. Longitudinal BRBs/SCEDs reduced pounding between the deck and abutment. The peak pounding force was reduced from 15,000 kN for the as-built bridge to 3,000 kN for the SCED retrofitted bridge and 2,800 kN for the BRB retrofitted bridge. For 20 of the 22 ground motions, BRB/SCED devices completely eliminated pounding.
9. Foundation seismic retrofit is important for the seismic performance of the bridge bent. Previous rehabilitation measures were adopted in this research including Dywidag bars connecting the piles to the pile caps and widening of the RC struts connecting the pile caps with a RC grade beam. BRBs and SCEDs improved the ductility performance of the bridge bent, but induced additional shear force in the column-brace connection. The column base shear capacity is enhanced by using the CFRP donut investigated in this research.
10. Addition of a CFRP donut at column-brace connections further enhanced the seismic shear capacity of the bridge and reduced drift demand. The concrete and rebar strain in the column at a section right above the CFRP donut were reduced.

REFERENCES

- AASHTO. (2011). *AASHTO Guide Specifications for LRFD Seismic Bridge Design*. American Association of State Highway and Transportation Officials, Washington, D.C.
- AASHTO (2014). *AASHTO LRFD Bridge Design Specifications, 7th Edition*. American Association of State Highway and Transportation, Atlanta, GA.
- ACI 440. (2015). *Guide for the Design and Construction of Concrete Reinforced with FRP Bars (ACI 440.1R-15)*. Farmington Hills, MI.
- Ameli, M. J., Parks, J. E., Brown, D. N., and Pantelides, C. P. (2015). "Seismic evaluation of grouted splice sleeve connections for reinforced precast concrete column-to-cap beam joints in accelerated bridge construction." *PCI J.*, 60(2), 80–103.
- Ameli, M. J., Brown, D. N., Parks, J. E., and Pantelides, C. P. (2016). "Seismic column-to-footing connections using grouted splice sleeves." *ACI Struct. J.*, 113(1–6), 1–10.
- Ameli, M. J., and Pantelides, C. P. (2016). "Seismic analysis of precast concrete bridge columns connected with grouted splice sleeve connectors." *J. Struct. Eng.*, 143(2), 04016176:1-13.
- American Concrete Institute Committee 318. (2014). *Building Code Requirements for Structural Concrete (ACI 318-14) and Commentary (ACI 318R-14)*. American Concrete Institute, Farmington Hills, MI.
- American Concrete Institute committee 440. (2017). *ACI 440.2R-08 Guide for the Design and Construction of Externally Bonded FRP Systems for Strengthening Existing Structures*. American Concrete Institute, Farmington Hills, MI.
- American Society of Civil Engineers. (2013). *ASCE/SEI 41-13 Seismic Evaluation and Retrofit of Existing Buildings*. American Society of Civil Engineers, American Society of Civil Engineers, Reston, VA.
- AISC Committee on Specifications. (2010). *ANSI/AISC 360-10 Specification for Structural Steel Buildings*. American Institute of Steel Construction, Chicago, IL.
- AISC. (2014). *Seismic Design Manual*. American Institute of Steel Construction. Chicago, IL.
- ASCE. (2013). *Minimum Design Loads for Buildings and Other Structures*. ASCE/SEI 7-10, Reston, VA.
- ASTM International. (2014). *ASTM D3039/D3039M-14 Standard Test Method for Tensile Properties of Polymer Matrix Composite Materials*. ASTM International, West Conshohocken, PA.
- Basu, S. B., and Shinozuka, M. (2011). "Effect of Ground Motion Directionality on Fragility Characteristics of a Highway Bridge." *Advances in Civil Engineering*, Article ID 536171.
- Bazaez, R. and Dusicka, P. (2016). "Cyclic behavior of reinforced concrete bridge bent retrofitted with buckling restrained braces." *Eng. Struct.*, 119, 34-48.
- Bazaez, R. and Dusicka, P. (2017). "Performance assessment of multi-column RC bridge bents seismically retrofitted with buckling-restrained braces." *Bull. Earthq. Eng.*, DOI:10.1007/s10518-017-0279-3.
- Billah, A. H. M. M., and Alam, M. S. (2014). "Seismic Performance Evaluation of Multi-column Bridge Bents Retrofitted with Different Alternatives Using Incremental Dynamic Analysis." *Eng. Struct.*, 62–63, 105–117.
- Bisadi, V., and Head, M. (2011). "Evaluation of Combination Rules for Orthogonal Seismic Demands in Nonlinear Time History Analysis of Bridges." *J. Bridge Eng.*, 16(6), 711-717.

- Brown, D. N., Parks, J. E., Ameli, M. J., and Pantelides, C. P. (2016). "Strut-and-tie models of repaired precast concrete bridge substructures with CFRP shell." *Composite Structures*, 138, 161–171.
- Chou, C., C., Chen, Y., Pham, D., Truong, V. (2014). "Steel braced frames with dual-core SCBs and sandwiched BRBs: Mechanics, modeling and seismic demands." *Eng. Struct.*, 72(1), 26-40.
- Christopoulos, C., Tremblay, R., Kim, H., and Lacerte, M. (2008). "Self-Centering Energy Dissipative Bracing System for the Seismic Resistance of Structures: Development and Validation." *J. Struct. Eng.*, 10.1061/(ASCE)0733-9445(2008)134:1(96), 96-107.
- California Department of Transportation. (2013). *Caltrans seismic design criteria version 1.7*. Division of Engineering Services, Sacramento, CA.
- CEB-FIP. (1993). *CEB-FIP Model Code 1990*. Thomas Telford Ltd., London.
- CEB-FIP. (2012). *CEB-FIP Model Code 2010*. Thomas Telford Ltd., London.
- Chai, Y. H., Priestley, M., and Seible, F. (1991). "Seismic retrofit of circular bridge columns for enhanced flexural performance." *ACI Struct. J.*, 88(5), 572–584.
- D'Amato, M., Braga, F., Gigliotti, R., Kunnath, S., and Laterza, M. (2012). "Validation of a modified steel bar model incorporating bond-slip for seismic assessment of concrete structures." *J. Struct. Eng.*, 138(November), 1351–1360.
- Dassault Systèmes Simulia. (2014). "ABAQUS version 6.14-1." *Dassault Systèmes Simulia*, Dassault Systèmes Simulia Corp, Providence, RI.
- Dhakal, R. P., and Maekawa, K. (2002). "Modeling for Postyield Buckling of Reinforcement." *J. Struct. Eng.*, 128(9), 1139–1147.
- El-Bahey, S., Bruneau, M., (2011). "Buckling restrained braces as structural fuses for the seismic retrofit of reinforced concrete bridge bents." *Eng. Struct.*, 33(3), 1052-1061.
- Fakharifar, M., Chen, G., Wu, C., Shamsabadi, A., Elgawady, M. A., and Dalvand, A. (2016). "Rapid repair of earthquake-damaged RC columns with prestressed steel jackets." *J. Bridge Eng.*, 21(4), 4015075.
- FEMA. (2009). *NEHRP Recommended Seismic Provisions*. FEMA P-695, Federal Emergency Management Agency, Washington, D.C.
- Gao, N., Jeon, J., Hodgson, D.E., and Desroches, R. (2016). "An innovative seismic bracing system based on a superelastic shape memory alloy ring." *Smart Mater. Struct.*, 25(2016)055030(16pp).
- Gergely, I., Pantelides, C. P., Nuismer, R. J., and Reaveley, L. D. (1998). "Bridge Pier Retrofit Using Fiber-reinforced Plastic Composites." *J. Compos. Constr.*, 2(4), 165–174.
- Guerrini, G., Restrepo, J.I., Massari, M., and Vervelidis, A. (2014). "Seismic Behavior of Posttensioned Self-Centering Precast Concrete Dual-Shell Steel Columns." *J. Struct. Eng.*, 141(4):04014115.
- Harajli, M. H., and Mabsout, M. E. (2002). "Evaluation of bond strength of steel reinforcing bars in plain and fiber-reinforced concrete." *ACI Struct. J.*, 99(4), 509–517
- Harajli, M. H. (2009). "Bond Stress-Slip Model for Steel Bars in Unconfined or Steel, FRC, or FRP Confined Concrete under Cyclic Loading." *J. Struct. Eng.*, 135(5), 509–518.
- He, R., Sneed, L. H., and Belarbi, A. (2013). "Rapid Repair of Severely Damaged RC Columns with Different Damage Conditions : An Experimental Study." *Int. J. Concrete Structures and Materials*, 7(1), 35–50.

- He, R., Yang, Y., and Sneed, L. H. (2015). "Seismic repair of reinforced concrete bridge columns: review of research findings." *J. Bridge Eng.*, 20(12), 4015015.
- Jiang, S., Zeng, X., Shen, S., and Xu, X. (2016). "Experimental studies on the seismic behavior of earthquake-damaged circular bridge columns repaired by using combination of near-surface-mounted BFRP bars with external BFRP sheets jacketing." *Eng. Struct.*, 106, 317–331.
- Kamulla, V., Erochko, J., Kwon, O. and Christopoulos, C. (2014). "Application of hybrid-simulation to fragility assessment of the telescoping self-centering energy dissipative bracing system." *Earthq. Eng. Struct. Dyn.* 2014; 43:811–830.
- Kitada, T. (1998). "Ultimate strength and ductility of state-of-the-art concrete-filled steel bridge piers in Japan." *Eng. Struct.*, 20(4–6), 347–354.
- Kumar, P., and Mosalam, K. M. (2015). "Shaking table evaluation of reinforced concrete bridge columns repaired using fiber-reinforced polymer Jackets." *J. Bridge Eng.*, 20(12), 4015025.
- Kunnath, S. K., and Brown, J. (2004). "Low-Cycle Fatigue Failure of Reinforcing Steel Bars." *ACI Mat. J.*, 101(6), 457–466.
- Kunnath, S. K., Heo, Y., and Mohle, J. F. (2009). "Nonlinear Uniaxial Material Model for Reinforcing Steel Bars." *J. Struct. Eng.*, 135(4), 335–343.
- Lehman, D. E., Gookin, S. E., Nacamuli, A. M., and Moehle, J. P. (2001). "Repair of earthquake-damaged bridge columns." *ACI Struct. J.*, 98(2), 233–242.
- Mander, J. B., Priestley, M., and Park, R. (1988). "Theoretical Stress-Strain Model for Confined Concrete." *J. Struct. Eng.*, 114(8), 1804–1826.
- McKenna, F. (2014), "Open system for earthquake engineering simulation (OpenSEEs)". Berkeley, CA.
- Marriot, D., Pampanin, S. and Palermo, A. (2011). "Biaxial testing of unbonded post-tensioned rocking bridge piers with external replicable dissipaters." *Earthq. Eng. Struct. Dyn.*, 40:1723-1741.
- Miller, D. J., Fahnestock, L. A., and Eatherton, M. R. (2012). "Development and experimental validation of a nickel–titanium shape memory alloy self-centering buckling-restrained brace." *Eng. Struct.*, 40, 288-298.
- Monzon, E. V., Buckle, I.G., and Itani, A.M. (2016). "Seismic Performance and Response of Seismically Isolated Curved Steel I-Girder Bridge." *J. Bridge Eng.*, 10.1061/(ASCE)ST.1943-541X.0001594.
- Moran, D. A., and Pantelides, C. P. (2012). "Elliptical and circular FRP-confined concrete sections: A Mohr-Coulomb analytical model." *Int. J. Solids and Structures*, 49(6), 881–898.
- NIST (2015). *Seismic Design of Steel Buckling-Restrained Braced Frames*. NIST CGR 15-917-34, National Institute of Standards and Technology, Gaithersburg, MD.
- OES (1995). *Vision 2000: Performance Based Seismic Engineering of Buildings*. Prepared by Structural Engineers Association of California. California Office of Emergency Services, Mather, CA.
- Panagiotakos, T. B., and Fardis, M. N. (2001). "Deformation of reinforced concrete members at yielding and Ultimate." *ACI Struct. J.*, 98(2), 135–148.
- Pantelides, C. P., Gergely, I., Reaveley, L.D., and Volnyy, V.A. (1999). "Retrofit of R/C bridge pier with CFRP advanced composites." *J. Struct. Eng.*, 125 (10), 1094-1099.

- Pantelides, C. P., and Fitzsimmons, G., (2012). "Case Studies of Seismic Rehabilitation of Reinforced Concrete Multicolumn Bridge Bents." *J. Bridge Eng.*, 10.1061/(ASCE)BE.1943-5592.0000203.
- Pantelides, C. P., and Gergely, J. (2002). "Carbon-fiber-reinforced polymer seismic retrofit of RC bridge bent: design and in situ validation." *J. Compos. Constr.*, 6(1), 52–60.
- Parks, J. E., Brown, D. N., Ameli, M. J., and Pantelides, C. P. (2016). "Seismic repair of severely damaged precast reinforced concrete bridge columns connected with grouted splice sleeves." *ACI Struct. J.*, 113(3), 615–626.
- Penzien, J. and Watabe, M. (1975). "Characteristics of 3-D earthquake ground motions." *Earthq. Eng. Struct. Dyn.* 3, 365–373.
- Priestley, M.J.N., Seible, F. and Calvi, G-M (1996) "Seismic Design and Retrofit of Bridges", *John Wiley and Sons*, NY, 686 p.
- Rodriguez, M., and Park, R. (1994). "Seismic load tests of reinforced concrete columns strengthened by jacketing." *ACI Struct. J.*, 91(2), 150–159.
- Saadatmanesh, H., Ehsani, M. R., and Jin, L. (1997). "Repair of earthquake-damaged RC columns with FRP wraps." *ACI Struct. J.*, 94(2), 206–214.
- Saiidi, M. S., and Cheng, Z. (2004). "Effectiveness of Composites in Earthquake Damage Repair of Reinforced Concrete Flared Columns." *J. Compos. Constr.*, 8(4), 306–314.
- Scott, M. H., and Fenves, G. L. (2006). "Plastic Hinge Integration Methods for Force-Based Beam–Column Elements." *J. Struct. Eng.*, 132(2), 244–252.
- Seible, B. F., Priestley, M. J. N., Hegemier, G. A., and Innamorato, D. (1997). "Seismic Retrofit of RC Columns with Continuous Carbon Fiber Jackets." *J. Compos. Constr.*, 1(2), 52–62.
- Shin, M., and Andrawes, B. (2011). "Emergency repair of severely damaged reinforced concrete columns using active confinement with shape memory alloys." *Smart Mat. and Struct.*, 20(6), 65018.
- Uriz, P., and Mahin, S. A. (2008). *Toward Earthquake-Resistant Design of Concentrically Braced Steel-Frame Structures*. Berkeley, CA.
- Upadhyay, A., Pantelides, C.P., and Ibarra, L. (2016). "Seismic Performance of Curved Bridges on Soft Soils Retrofitted with Buckling Restrained Braces." *Proc. of Geotech. and Struct. Eng. Congress 2016*. ASCE, Phoenix, AZ, 118-137.
- Upadhyay, A. and Pantelides, C.P. (2017). "Comparison of the Seismic Retrofit of a Three-Column Bridge Bent with Buckling Restrained Braces and Self Centering Braces." *Proc. of Struct. Congress 2017*. ASCE, Denver, CO, 414-423.
- Varela, S. and Saiidi, M. (2016), "A bridge column with superelastic NiTi SMA and replacable rubber hinge for earthquake damage mitigation." *Smart Mater. Struct.*, 25(2016)075012(18pp).
- Vosooghi, A., and Saiidi, M. S. (2010). Post-earthquake evaluation and emergency repair of damaged RC bridge columns using CFRP materials (Report No. CCEER-10-05). Reno, NV.
- Vosooghi, A., and Saiidi, M. S. (2013). "Design guidelines for rapid repair of earthquake-damaged circular RC bridge columns using CFRP." *J. Bridge Eng.*, 18(9), 827–836.
- Wang, Y., Ibarra, L., and Pantelides, C. (2016). "Seismic Retrofit of a Three-Span RC Bridge with Buckling-Restrained Braces." *J. Bridge Eng.*, 10.1061/(ASCE)BE.1943-5592.0000937, 04016073.

- Wei, X. and Bruneau, M. (2016). “Case Study on Applications of Structural Fuses in Bridge Bents.” *J. Bridge Eng.*, 21(7):05016004.
- Wu, R.-Y., and Pantelides, C. P. (2017a). “Rapid Seismic Repair of Reinforced Concrete Bridge Columns.” *ACI Struct. J.*, 114(5), 1339–1350.
- Wu, R.-Y., and Pantelides, C. P. (2017b). “Rapid Repair and Replacement of Earthquake-damaged Concrete Columns Using Plastic Hinge Relocation.” *Composite Structures*, 180, 467–483.
- Wu, R.-Y., and Pantelides, C. P. (2017c). “Rapid seismic repair of severely damaged cast-in-place reinforced concrete bridge piers (No. 17-06278).” *Transportation Research Board 96th Annual Meeting of Transp. Res. Board*, Washington D.C.
- Wu, R.-Y., and Pantelides, C. P. (2017d). “Rapid Seismic Repair of Severely Damaged Reinforced Concrete Bridge Piers.” *Proc. Struct. Congress 2017*, Denver, CO, 370–381.
- Wu, R.-Y., and Pantelides, C. P. (2018). “Analytical Models for Seismic Repair of Bridge Columns Using Plastic Hinge Relocation.” *Proc. Struct. Congress 2018*, Fort Worth, TX, 296–307.
- Xiao, Y., Wu, H., and Martin, G. R. (1999). “Prefabricated composite jacketing of RC columns for enhanced shear strength.” *J. Struct. Eng.*, 125(3), 255–264.
- Xu, W., and Pantelides, C. P. (2017). “Strong-axis and weak-axis buckling and local bulging of buckling-restrained braces with prismatic core plates.” *Eng. Struct.*, 153(2017), 279-289.
- Yan, Z., and Pantelides, C. P. (2011). “Concrete column shape modification with FRP shells and expansive cement concrete.” *Constr. and Building Materials*, 25(1), 396–405.
- Yang, Y., Sneed, L. H., Morgan, A., Saiidi, M. S., and Belarbi, A. (2015). “Repair of RC bridge columns with interlocking spirals and fractured longitudinal bars – An experimental study.” *Constr. and Building Materials*, 78, 405–420.
- Zhao, J., and Sritharan, S. (2007). “Modeling of Strain Penetration Effects in Fiber-Based Analysis of Reinforced Concrete Structures.” *ACI Struct. J.*, 104(2), 133–141.
- Zhou, Z., He, X.T., Wu, J., Wang, C.L., and Meng, S.P. (2014) “Development of a novel self-centering buckling-restrained brace with BFRP composite tendons.” *Steel and Composite Structures*, 16(5), 491-506.